ABSTRACT

Title of dissertation: ASTEROID CONTROL VIA NEUTRAL BEAM EMITTING SPACECRAFT

Anthony Joseph DeCicco
Doctor of Philosophy, 2018

Dissertation directed by: Professor Christine Hartzell
Department of Aerospace Engineering

Automated surveys along with population models have determined that tens of thousands Near Earth Objects (NEOs) exist and regularly cross over the Earth's orbit. While none of the currently discovered NEOs are predicted to impact Earth, many have yet to be discovered. We propose using neutral beam equipped spacecraft to deflect an asteroid from an Earth impact trajectory. Neutral beams are created through global neutralization of ion beams via recombination reactions and contain no charged particles.

This thesis focuses on the design and testing of a unique neutral beam thruster and its application to planetary defense. The first contribution of this thesis focuses on the efficacy of using low-thrust propulsion to de-spin and deflect sub-kilometer sized asteroids. The second contribution of this thesis demonstrates that neutral beams, a technology typically used to heat tokamak plasmas, can be scaled for keV electric propulsion for spacecraft. The third contribution of this thesis is that a method has been developed to conduct thrust measurements for sub-Newton propul-

sion on a hanging pendulum thrust stand during thermal drift. For the fourth contribution of this thesis analytical expressions for a low power neutral beam are derived and simulations are conducted to design a unique gas diffusion neutralizer. The experimental performance is validated against both the analytical expressions and simulation data.

Using neutral beams for mitigating the hazard of sub-kilometer asteroids is possible within current and near-term technology. The gas diffusion neutralizer designed is applicable to other gridded ion thrusters with only minor modifications needed. This thesis presents the experimental methods for neutral beam characterization including assembly of the diagnostics. The improvements in testing on a hanging pendulum thrust stand allow for more rapid characterization of the thrust performance of sub-Newton thrusters. The analytical expressions and simulations developed by this work have been confirmed by experimental data and demonstrate the viability of neutral beam propulsion. Future work in this field could investigate deflection mission design, alternate ion sources, gas diffusion neutralizer material choices, ion deflection subsystems, and higher energy ion beams.

Asteroid Control via Neutral Beam Emitting Spacecraft

by

Anthony Joseph DeCicco

Dissertation submitted to the Faculty of the Graduate School of the
University of Maryland, College Park in partial fulfillment
of the requirements for the degree of
Doctor of Philosophy
2018

Advisory Committee:
Professor Christine M. Hartzell, Chair/Advisor
Professor David Akin
Professor Adil Hassam
Professor Ray Sedwick
Professor Elaine Oran
Dr. Robert Adams

Preface

On JD 2456897.25, in the Milky Way on the Orion Arm orbiting a star known as Sol on the third planet, Earth, my Ph.D. career started at the University of Maryland under the advisement of Dr. Christine Hartzell. My passion for spaceflight started long before then on a family vacation to Disney World when we also visited Kennedy Spaceflight Center. At KSC, I learned about something that would define the modern era of spaceflight: a space station built by a partnership of countries from around the world, some allies and others with tepid geopolitical ties, working despite their differences to conduct long-term human spaceflight and research to benefit all of humanity. This was my calling to engineering: to advance knowledge and help build a world where exploration and discovery drive humanity.

My Great Uncle Unc gave me a telescope one year and with it I was able to see our Moon, Luna, not as a white orb in the sky but as a physical solar system body with craters, ridges, and mountains. An alien world that told a story, which I had no idea at the time was about the creation of Earth and the history of the solar system. Where do asteroids come into this story? Every impact crater on Luna tells a story of a near miss of an asteroid collision on Earth, but it also tells us about the asteroid population in our neighborhood. Planetary scientists started by looking at those craters to determine what the relative size population of Near Earth Asteroids might be. From that and further observations using ground telescopes, we have learned a great deal about the busy asteroid traffic in our neighborhood. Certain types of asteroids are rich in metals, hydrated minerals, and carbon or silica deposits. These

are the basic building blocks of spacecraft flying around at our doorstep waiting for us to dare to grab them and begin a new revolution in spaceflight by building our vehicles in orbit. Occasionally one of these might also cause damage on Earth and so my calling for my Ph.D. was to develop a technology that could both handle deflection of an asteroid yet be able to move it into precisely the orbit we want to visit later to build spacecraft. My research is a start in the direction of Earth independence, a contribution in how to safely move asteroids for protecting Earth and future resource utilization. It helps realize my dream where humanity explores every planetary system in our solar system, refilling and rebuilding in-situ, and always learning a bit more about ourselves, life, and Earth along the way.

Dedication

To my parents who instilled in me from an early age the importance of education.

Acknowledgments

Thank you to my advisor Dr. Christine Hartzell for taking me on and giving me a chance to pursue my graduate studies. Your dedication to being a wonderful advisor was exemplified by your commitment to weekly one-on-one meetings which helped me immensely in bouncing ideas off of you and getting direction at critical junctions. Thank you also for the lab dinners, semester charades competitions, and lab socials where we were able to get away from work and just have fun together as a lab.

Thank you to the NASA Space Technology Research fellowship for sponsoring my education and this research. Your continued support has afforded me the opportunity to present my research around the world and conduct my experiments at state of the art facilities at NASA. I am very thankful for this program and its drive to bring concepts to reality for the future of space exploration.

Thank you to my mother and father for always supporting my educational pursuits and for the many years of nights helping me with a science fair project, book report, or dreaded art project. Thank you also for understanding my working holidays when I was home during my PhD and for coming down to visit me every year. Mom, thank you for always being my greatest advocate and pushing me to work hard. I am so proud of you finishing your Masters and teaching collegiate-level mathematics. Sorry the weather decided to freeze away the cherry blossoms last year Mom. Dad, thank you for teaching me the fundamental tool skills and how to go from a sketch on paper to a physical build. You have shown me how to

balance being an active member of your field and have a family. I wish I had half the woodworking knowledge that you do, but I know you'll teach me along the way.

Thank you to my Nonno and Nonna who have always provided our family with a grounded, loving environment. The many Sunday dinners, family trips to the beach and Disney World, and sleepovers were an essential part of growing up. I have enjoyed our weekly Skype calls while I've been in graduate school and it made me feel that much closer to home telling you about my weekly progress and learning about what was happening in our hometown. Nonna, thank you for the incalculable number of veal piccatas, hamburgers, steak and cheeses, gnocchis, and raviolis and for teaching me how to make all of my favorite pastas (the secret sauce recipe will always be in my lab notebook). Thank you for the care packages you would insist that I take back with me every time I came up to visit. Nonno, thank you for having me tinker in the barn and open up electric motors when I could barely reach the bench. Thank you also for the watermelon you would bring out for me when I was doing yardwork on a hot summer day, the nights of Poirot on PBS, and making sure Nonna put the pepperoni in the sauce.

Thank you to my sister Maria and brother-in-law James. Maria you made my transition into college eight years ago so much easier being right in the area. I'm so proud of you pursuing and finishing your PhD in immunology even when you faced uphill battles in your experiments. Your perseverance showed me that whole experiments may not go right the first or 20^{th} time, but finding ways to fix each issue eventually demonstrates how rewarding the process can be. James, I am very happy to have you in the family and to have another sci-fi nerd to talk with. You've

worked very hard for each opportunity in your life and it has rewarded you with a great career.

Thank you to my Uncle Steven and Aunt Ann Marie for hosting the numerous Sunday dinners and welcoming me over. Every weekend, while a bit chaotic between the dogs and kids, provided me with a welcome break from my studies. I'll miss making desserts for the family each week and spending time talking about spaceflight, economics, or Game of Thrones.

Thank you to Rob and Glen for being wonderful mentors and for getting me involved on projects that pushed me intellectually. Having the experience to work at NASA on advanced propulsion and learn what it takes to conduct research in technology development has made me a better engineer, troubleshooter, & researcher and allowed me to work in fields that are once-in-a-lifetime opportunities. I'm also going to miss going out for BBQ with you guys.

Finally, thank you to my friends Eric, Christina, Thomas, Julie, Zach, Dylan, Katy, Matt, Ryan, Mel, Lem, Brent, Lauren, Teddy, and Elaine for making these past few years in graduate school memorable. From hiking trips, trivia nights, beer & wine tastings, college football & basketball, water-skiing, potlucks, board games and speculating the future of spaceflight, and Thomas' famous craft brews, you have all helped me get out of the lab and out doing the things I love.

Table of Contents

Preface ii

Dedication iv

Acknowledgements v

List of Tables x

List of Figures xi

List of Abbreviations xiii

1 Introduction and Motivation 1
- 1.1 Near Earth Asteroid (NEOs) and Planetary Defense . . . 1
- 1.2 Electric Propulsion as a Deflection Method . . . 2
- 1.3 Plasma Properties and Terminology . . . 3
- 1.4 Asteroid Environment Hazards . . . 5
- 1.5 Neutral Beams . . . 6
  - 1.5.1 Ion source . . . 8
  - 1.5.2 Neutralization through Charge Exchange Reactions . . . 8
- 1.6 Thesis Overview . . . 10
- 1.7 Thesis Contributions . . . 11
- 1.8 Publications . . . 12
  - 1.8.1 Journal . . . 12
  - 1.8.2 Conferences . . . 12
  - 1.8.3 Additional Presentations . . . 13

2 Literature Review 14
- 2.1 Asteroid Deflection Methods . . . 14
- 2.2 Asteroid De-spin . . . 18
- 2.3 Prior Development of Neutral Beams . . . 19
- 2.4 Requirements for an Alternative Asteroid Deflection Method . . . 20

3 De-spin and Deflection of Hypothetical Asteroid 2017 PDC 24
3.1 Deflection of Hypothetical Asteroid 2017 PDC . . . 24
3.2 Arresting the Rotation of 2017 PDC . . . 34
3.3 Discussion . . . 42

4 Design of a Gas Diffusion Neutralizer for an Argon Ion Source 44
4.1 One Dimensional Model for Neutralization and Neutral Beam Performance . . . 44
4.2 Effect of Gas Injection Rate and Neutralizer Geometry . . . 54
4.3 Discussion . . . 63
4.4 Final Design of the Gas Diffusion Neutralizer . . . 63

5 Testing Methodology for a Neutral Beam Technology Demonstration 68
5.1 Procedure for the preparation of the VAHPER thrust stand and vacuum chamber for thrust testing . . . 68
5.2 Procedure for the calibration of the VAHPER thrust stand and thrust measurements of the neutral beam technology demonstrator . . . 73
5.3 Construction of a Copper Faraday Cup . . . 75
5.4 Procedure for the preparation of neutralization measurements via a Faraday cup . . . 77
5.5 Procedure for neutralization measurements via a Faraday cup . . . 79
5.6 Construction of a Direct-Contact Graphite Calorimeter . . . 82
5.7 Procedure for thermal output measurements via a direct contact graphite calorimeter . . . 86

6 Performance and Characterization 90
6.1 Technology Demonstration Description . . . 90
6.2 Low Thrust Measurement Techniques . . . 92
6.3 NBAC Thrust Measurement Data . . . 95
6.4 Neutralization Measurements via Faraday Cup . . . 103
6.5 Discussion . . . 110

7 Calorimetry of a Neutral Beam 112
7.1 Graphite Calorimeter Experiment Set-up . . . 113
7.2 Kinetic Losses from Neutralization . . . 115
7.3 Discussion . . . 118

8 Conclusion and Future Work 119
8.1 Conclusions . . . 119
8.2 Future Work . . . 123

Bibliography 126

List of Tables

3.1 Densities of asteroid classes 27
3.2 Propellant usage per spacecraft in a four thruster NBAC system for asteroid deflection 34

4.1 Required Power for a Neutral Beam 50

5.1 Wiring Channels on NI 9205 for Calorimeter 89

List of Figures

1.1 Ion Beam Shepherd . . . 3
1.2 Debye Length . . . 4
1.3 Particle Lofting Free Body Diagram . . . 6
1.4 Neutral Beam schematic . . . 7
1.5 Schematic of Ion Source . . . 9

3.1 Closest approach of 2017 PDC of various spectral types for 420 day campaign . . . 29
3.2 Maximum radius of 2017 PDC able to be deflected via a neutral beam 30
3.3 Effect of spacecraft failure on C-type asteroid deflection . . . 31
3.4 Effect of spacecraft failure for a variety of spectral types . . . 33
3.5 Schematic of asteroid deflection with reference frames . . . 36
3.6 Known rotation rates of asteroids . . . 37
3.7 Partial and full despin for asteroids of various spectral types . . . 38
3.8 Propellant mass required to fully de-spin an asteroid of various spectral types . . . 41
3.9 Partially de-spinning fast rotating asteroids . . . 42

4.1 Neutralization ratio for Argon ion energy range . . . 46
4.2 Predicted thrust for a neutral beam . . . 51
4.3 Surface sputtering thrust enhancement . . . 52
4.4 Neutral beam utilization prediction . . . 53
4.5 Neutral beam specific impulse prediction . . . 53
4.6 Terminology for gas flow study . . . 56
4.7 Gas flow design study geometry cases . . . 57
4.8 Neutralization predictions for COMSOL and Analytical models . . . 58
4.9 Effects of geometry on background density . . . 59
4.10 Gas density profiles for various gas study geometries . . . 60
4.11 Neutralization predictions for various gas study geometries . . . 60
4.12 Partially open geometry for gas flow study . . . 61
4.13 Comparing gas density profile for open and partially open geometries 61
4.14 Comparing neutralization for open and partially open geometries . . . 62
4.15 Gas Diffusion Neutralizer Screen . . . 64

4.16 Gas Diffusion Neutralizer Structure . . . 65
4.17 Gas Diffusion Neutralizer Caps . . . 66
4.18 Exploded view of gas diffusion neutralizer . . . 67

5.1 Neutral Beam on the VAHPER thrust stand . . . 71
5.2 Power feedthrough at NASA Marshall Spaceflight Center . . . 72
5.3 Vacuum door at NASA Marshall Spaceflight Center . . . 72
5.4 Copper Faraday cup . . . 76
5.5 Neutral Beam in the UMD vacuum chamber . . . 79
5.6 Sealed vacuum chamber at UMD . . . 80
5.7 Calorimeter blocks initially placed . . . 84
5.8 Finished direct contact graphite calorimeter . . . 85
5.9 Soldered 50 pin connector . . . 85
5.10 Thermocouple set-up at UMD . . . 88

6.1 Cross section of test set-up . . . 92
6.2 Gas diffusion neutralizer exploded view . . . 92
6.3 Torsion Thrust Stand Schematic . . . 94
6.4 Linear variable differential transducer . . . 95
6.5 Hanging pendulum thrust stand . . . 96
6.6 Repeatability of thermal drift . . . 98
6.7 Thrust test data example . . . 100
6.8 Standard deviation method . . . 101
6.9 Thrust measured used VAHPER thrust stand . . . 103
6.10 Faraday cup schematic . . . 105
6.11 Neutralization results . . . 108

7.1 Graphite calorimeter experiment schematic . . . 114
7.2 Calorimeter temperature example . . . 115
7.3 Comparing measured power with thrust . . . 117

List of Abbreviations

eV	Electron-Volts
GMAT	General Mission Analysis Tool
LD	Lunar Distance
NBAC	Neutral Beam for Asteroid Control
NEA	Near Earth Asteroid
NEO	Near Earth Object
PHA	Potentially Hazardous Asteroid
SOI	Sphere of Influence
TRIM	Transport of Ions in Matter
VNB	Velocity - Normal - Binormal
CNEOS	Center for NEO Studies
JPL	Jet Propulsion Lab
NAC	NASA Advisory Council
NASA	National Aeronautics and Space Administration
NI	National Instruments

Chapter 1: Introduction and Motivation

1.1 Near Earth Asteroid (NEOs) and Planetary Defense

Automated surveys have become a staple of Near Earth Object (NEO) discovery and observation. The Center for NEO Studies (CNEOS) at JPL [1] is responsible for high-precision orbit determination and ephemerides as well as hazard assessment for NEOs. As of 06/03/18 there are 18321 NEOs with 1904 of those qualifying as Potentially Hazardous Asteroids (PHAs) [1]. From 2000-2017, there were 1749 close approaches at 5 LD (Lunar Distances) or less and 594 fireball events [1]. In response to the NASA Advisory Council (NAC) report [2], NASA created the Planetary Defense Coordination Office (PDCO) to coordinate the United States' discovery and response efforts for NEOs.

Planetary defense encompasses four distinct fields: observation, characterization, mitigation, and coordination. The current NEO observation programs [1] are Catalina Sky Survey [3], Pan-STARRS [4], NEOWISE [5], Space Surveillance Telescope (SST) [6], and ATLAS [7]. With the exception of ATLAS, these automated surveys are focused upon surveying the sky to determine the total NEO population. ATLAS is focused upon discovering asteroids that are on a terminal trajectory for Earth days or weeks before impact. Characterization is carried out using data from

these surveys and subsequent observations by smaller telescopes owned by universities, space agencies, and organizations. Characterization also includes assessing the historical impact risk of the population using models derived from such sources as Chelsey *et al.* [8]. Mitigation encompasses all technologies and methods by which an asteroid or comet can be deflected to avoid casualties and damage on Earth. Of the proposed asteroid deflection methods, there are two fundamental categories: high impulse and slow push. The applicability of either depends upon the asteroid size and the time until impact. Finally, coordination between observation, characterization, mitigation, and other government agencies is carried out by the PDCO.

1.2 Electric Propulsion as a Deflection Method

The foundations of electric propulsion have been credited to Robert Goddard, Herman Oberth, and Ernst Stuhlinger [9]. The first successful in-space test was that of the SERT I in 1964 on a ballistic flight from Wallops [10]. Since then, electric propulsion has enabled unique long-duration spaceflight missions, most notably the Dawn mission to Vesta and Ceres [11]. Using ion propulsion, Dawn was the first spacecraft to rendezvous with two different bodies in the solar system. It is because of the high efficiency afforded through using electric propulsion that such mission profiles are possible. Bombardelli *et al.* [12] have proposed using electric propulsion for asteroid deflection. In this slow push method, called the ion beam shepherd, the thrust plume acts upon the asteroid as some distance, d. Over the course of months or years, the ion beam shepherd deflects the asteroid from an Earth impact

trajectory. This has several advantages as it allows for the fine control of an asteroid through a contactless, efficient, and proven spaceflight technology.

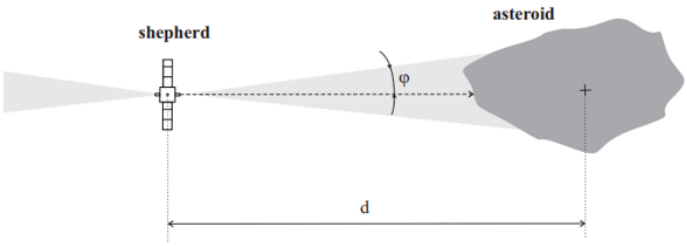

Figure 1.1: The ion beam shepherd (reproduced from [12]) uses its thrust plume to act upon the asteroid at a distance, d. This pushes the asteroid from an impact trajectory.

1.3 Plasma Properties and Terminology

Plasma is a state of matter where the electrons in an atom have been excited to a point that they disassociate from the atom; these electrons are now considered to be "free electrons." In a plasma there is a collection of ions and free electrons and the number density of each is typically equal to one another; this is also known as a quasi-neutral plasma (See Fig. 1.2). In this quasi-neutral plasma, the free electrons move around at a much higher speed than the heavier ions. The ions can be considered stationary relative to the electrons. Quasi-neutrality inherently makes an assumption that for the scale length of concern (distance R in Fig. 1.2) the mean distance (λ_D in Fig. 1.2) between an ion and a free electron is much smaller so that the total charge of the system is zero.

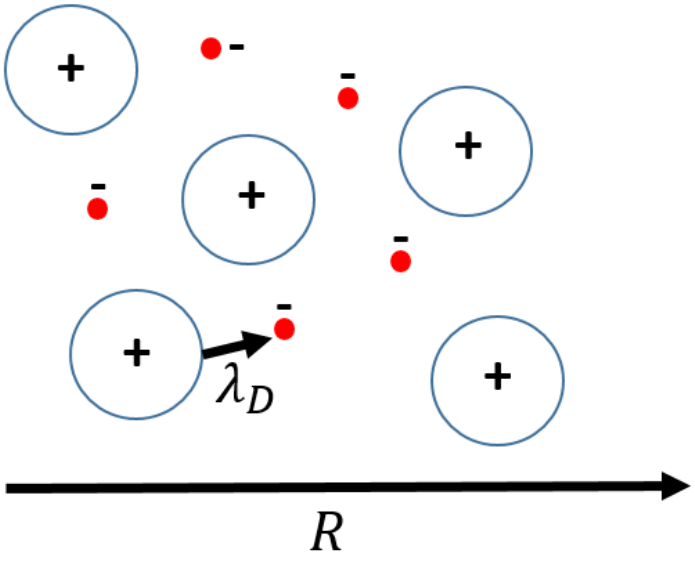

Figure 1.2: The ions (blue outline circles) and free electrons (red dots) are in equal number density making this a quasi-neutral plasma. The mean distance between ions and free electrons λ_D is much smaller than the scale length of concern R.

The mean distance between an ion and free electron is known as the Debye length as is calculated by Eq. 1.1:

$$\lambda_D = \sqrt{\frac{\epsilon_0 k_B T_e}{n e^2}} \tag{1.1}$$

where ϵ_0 is the permitivitty of free space, k_B is the Boltzmann constant, T_e is the electron temperature, n is the number density, and e is the elementary charge. The plasma temperature is measured in a electron-Volts (eV); 1 eV is the energy equivalent of taking a single charge and accelerating it through an electric potential of 1 V. The conversion from eV to K is approximately 1 eV = 11604 K [13]. This is a convenient measurement for plasmas, and in our case for ion acceleration, as

the ion temperature is the total electric potential through which the ions have been accelerated.

1.4 Asteroid Environment Hazards

There is a potential environmental hazard that Bombardelli and Paleaz [18] have not considered. Asteroids are likely a collection of boulders and dust held together by gravity and cohesion. Cohesion is likely the dominant force holding small asteroids together [19, 20]. Additionally, it has been hypothesized that dust grains may be detached from the surface of small asteroids due to electrostatic forces (a.k.a. electrostatic dust lofting) [21,22]. Hartzell and Scheeres [21] proposed a model of dust lofting considering self-gravity, cohesion between grains, and seismic shaking. They show that grains can loft from the surface of Itokawa for electric fields of order 10^2 - 10^3 V/cm, depending on the cohesion. Lofted dust grains could create a dusty, charged exosphere that would be dangerous for spacecraft. Typical ion propulsion such as [12] assumes a quasi-neutral plasma, meaning that the ions and electrons in the flow have the same number density. At the scale of the Debye length (the mean separation of ions from electrons in the flow) and larger, the plasma can be considered electrically neutral. However at length scales smaller than the Debye length, this is no longer true. The Debye length depends upon the temperature and density of the plasma. While the Debye length at the exit of the thruster may be microns or smaller, the Debye length will increase with decreasing plasma density as the plume expands. For a spacecraft positioned 200m from an asteroid

with a thrust plume expansion half angle of 10°, the Debye length would increase to 35m. At scales smaller than 35m on the surface of the asteroid, the flux of ions and electrons could create a potential difference. If the resulting electrostatic force exceeds the cohesion and gravitational acceleration on a grain ($F_E > F_G + F_C$), then the particle would loft from the surface, possibly creating a hazardous environment for nearby spacecraft.

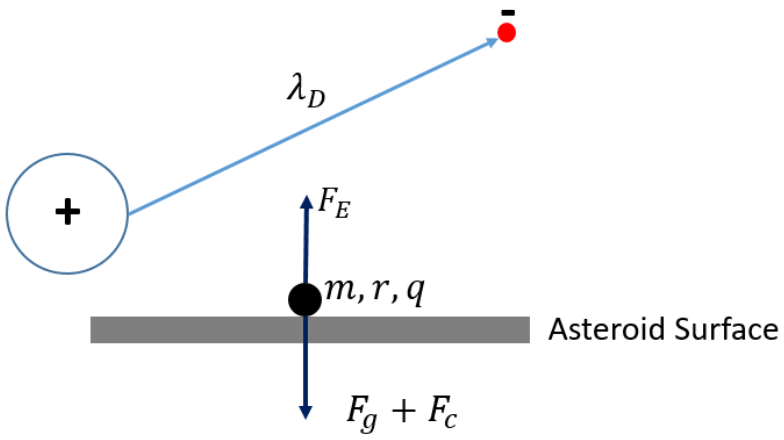

Figure 1.3: A dust grain is attached to the asteroid surface by gravity (F_G) and cohesion (F_C). If an ion beam impinges on the surface of an asteroid and its Debye length (λ_D) is greater that the size of the dust grain, then the grain can experience an upwards electric force (F_E). If $F_E > F_G + F_C$ then the particle will loft from the surface.

1.5 Neutral Beams

To avoid the possible hazard of electrostatically lofted dust, we will design a neutral beam capable of deflecting an asteroid from an earth impact. Neutral beams are comprised of three modules: an ion source, a neutralization chamber, and an ion dump [15]. A typical neutral beam is a globally neutralized particle beam used as

a non-magnetic and non-electrostatic heating element for fusion tokamaks. Fig. 1.4 presents a basic schematic for a neutral beam. Ions are created and accelerated in the ion source and directed to the gas cell where they undergo ionization and electron recombination reactions with the background cold neutral gas [16]. Upon exiting the gas cell, the particles are mainly fast neutral atoms with some ions left in the particle beam, due to the reactions being predominantly electron recombination reactions in the 1-10 keV range [17]. These ions are deflected via an electric field into an ion dump allowing for a pure neutral beam with no electric or magnetic field.

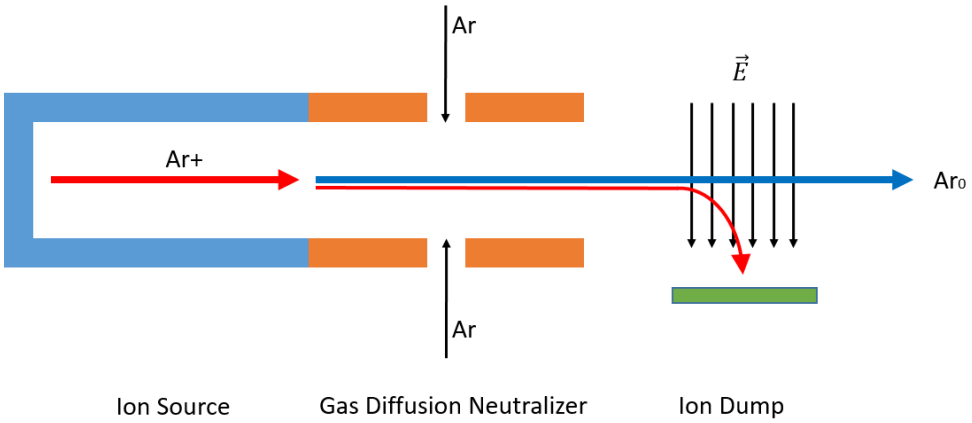

Figure 1.4: The ions (Ar^+) are created and accelerated in the ion source. The gas (Ar) is injected into the neutralizer. The ions react with the gas and most are neutralized. The remaining ions are deflected via an electric field ($\vec{E}$) into the ion dump, leaving the neutral fast particles flowing downstream (Ar°)

1.5.1 Ion source

An ion source creates a plasma and preferentially discharges only the ions from the plasma. One type of ion source is a DC two-grid source (KDC 10 schematic [14] shown in Fig. 1.5). In this source, a tungsten wire cathode is heated to a point that hot, free electrons disassociate from the wire. A gas is injected into the system and the free electrons impact the gas, exciting an electron in the gas and causing it to disassociate. The ions are accelerated to the screen grid due to the anode being positively charged and repelling the ions, whereas the electrons are attracted to the anode. The accelerator grid is charged to a small negative potential preventing the electrons from escaping but attracting the ions to the grid. The ions exit the ion source and continue downstream.

1.5.2 Neutralization through Charge Exchange Reactions

We consider the case of a 1 keV argon ion output from the KDC 10 [14]. There are two important charge exchange reactions to consider for keV argon ions. During operation, an ion beam of given energy and density is sent through a neutralization chamber filled with neutral gas (also referred to as the 'neutral target') where electron capture and ionization reactions occur. For an argon target:

$$Ar^{+}_{eV} + Ar \rightarrow Ar_{eV} + Ar^{+} \quad Electron\,Capture$$

$$Ar_{eV} + Ar \rightarrow Ar^{+}_{eV} + Ar + e^{-} \quad Ionization$$

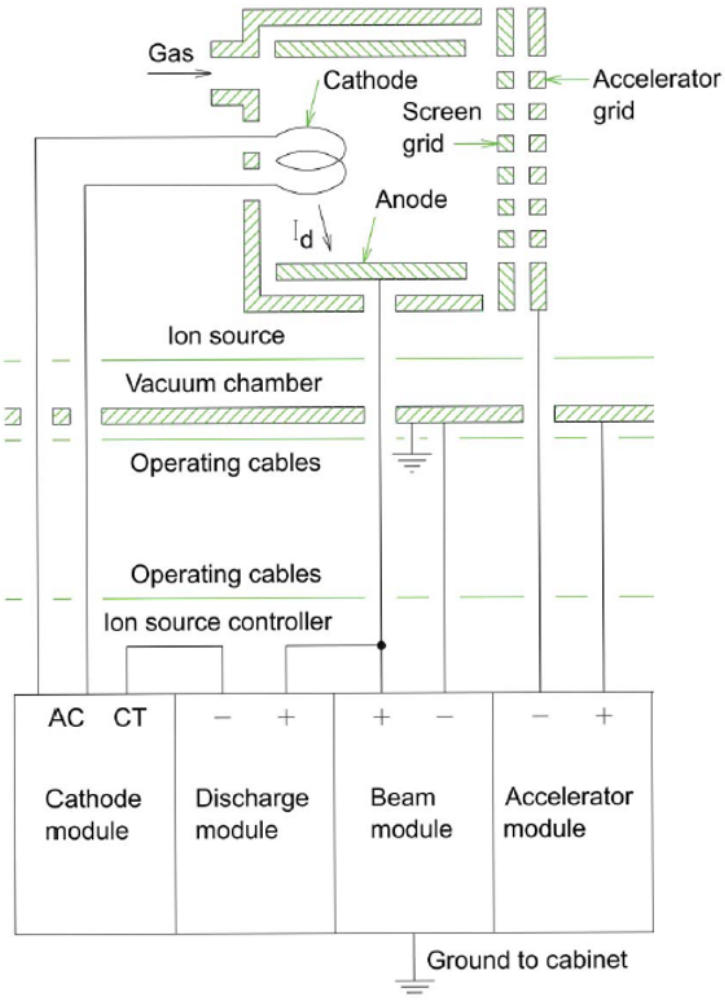

Figure 1.5: The ion source consists of a graphite wire cathode that is heated to release electrons. These electrons impact the gas creating ions. The screen grid and accelerator grid separate and accelerate the ions from the electrons, leading to only ions exiting the system. Reproduced from [14].

Electron capture reactions dominate due to a larger reaction cross section and a majority of the beam flux becomes neutrally charged without a significant reduction in the beam's momentum. The remaining ions in the beam are deflected into ion dumps using applied magnetic or electric fields resulting in a beam of high energy neutral particles.

1.6 Thesis Overview

This thesis will present the development, testing, and application of a Neutral Beam for Asteroid Control (NBAC). The concept is designed for 100 - 400m asteroids and NBAC's goal is to achieve sufficient deflection in less than 5 years of operations. Our chosen asteroid size range stems from Johnson's [23] recent data that these are likely to be the largest population of undiscovered NEAs that were mandated by Congress in the 2005 Fiscal Year NASA Authorization Act for discovery by 2020 [24]. A 5 year deflection time limitation is between that of a high impulse nuclear device [25] and slow-push gravity tractor [26].

In Chapter 2 we will cover past research on asteroid deflection and de-spin techniques and the requirements for an alternate means of asteroid control. Chapter 2 will also cover the development of neutral beams and low thrust measurement techniques. In Chapter 3 we use the hypothetical asteroid 2017 PDC as a reference PHA to determine the performance of a neutral beam spacecraft architecture on deflection and de-spin. Studies in Chapter 4 investigate the effect of gas diffusion neutralizer geometry and gas flow rate on gas background density and neutralization of a 1 keV argon ion beam using an analytical approach and COMSOL. We outline the methodology in Chapter 5 for building the diagnostics and the experimental procedures. In Chapter 6 we present the thrust and neutralization data of the neutral beam technology demonstrator. We present calorimetric data in Chapter 7 to investigate whether momentum losses occur during neutralization of the ion beam. Finally, in Chapter 8 we discuss the conclusions and future work for this research.

1.7 Thesis Contributions

This thesis is focused upon the theory, design, and application of a neutral beam for asteroid control. We first investigate low thrust asteroid de-spin and deflection. We then present the design and testing of a low-power neutral beam technology demonstration. This research was accomplished using GMAT, COMSOL, and Matlab routines coupled with analytical expressions and through experimental work. Through this research, further work can be accomplished to develop an efficient low power neutral beam. There are four major contributions:

1) The efficacy of low-thrust asteroid de-spin and deflection via neutral beam spacecraft is quantified for sub-kilometer sized asteroids

2) It is demonstrated that neutral beams are scalable for keV electric propulsion for spacecraft.

3) A method to conduct thrust measurements for sub-Newton propulsion on a hanging pendulum thrust stand during thermal drift is developed.

4) Analytical expressions for a low power neutral beam are derived and simulations are conducted to design a unique gas diffusion neutralizer. The experimental performance is validated against both the analytical expressions and simulation data.

1.8 Publications

The publications listed here cover the dissertation research and related fields of study:

1.8.1 Journal

- DeCicco, A.J., Hartzell, C.M., Adams, R.B, and Polzin, K.A., "The feasibility of deflecting asteroid 2017 PDC using neutral beam propulsion. Acta Astronautica, In Press, 2018.

- DeCicco, A.J. and Hartzell, C.M., "Design of a Gas Diffusion Neutralizer in Support of Neutral Beam Propulsion." In Preparation.

- DeCicco, A.J., Hartzell, C.M., Adams, R.B, and Polzin, K.A., "Performance and characterization of a neutral beam propulsion technology demonstration." In Preparation.

1.8.2 Conferences

- DeCicco, A.J., Hartzell, C.M., Adams, R.B, and Polzin, K.A., "Preliminary Asteroid Deflection Mission Design for 2017 PDC Using Neutral Beam Propulsion. In Aerospace Conference, 2018 IEEE, pp. 1-10. 2018.

- Cortez, R.J, Cassibry, J.T., Adams, R.B., Doughty, G.E., Taylor, B.D., DeCicco, A.J., "Progress on Fusion Modeling and the Charger-1 Power Facility

at UAH. In Nuclear & Emerging Technologies for Space (NETS) Proceedings, pp.37-44, 2017.

- DeCicco, A.J., and Hartzell, C.M. "Asteroid Deflection via Neutral Beam Emitting Spacecraft." In IAA Planetary Defense Conference, IAA, 2017.

- DeCicco, A.J., and Hartzell, C.M. "System-Level Design Considerations for Asteroid Despin via Neutral Beam Emitting Spacecraft." In Aerospace Conference, 2016 IEEE, pp. 1-8. IEEE, 2016.

- DeCicco, A. J., and Hartzell, C.M. "Cohesion and Electrostatic Lofting of Ellipsoidal Dust Grains." In Lunar and Planetary Science Conference, vol. 46, p. 2002, 2015.

1.8.3 Additional Presentations

- "Neutral Beam Deflection," Keynote Speech at the 2017 New England Association of Technology Teachers

- "Astrodynamics: The Fundamentals of Rocket Science," Seminar at the 2017 New England Association of Technology Teachers

- "System-Level Design Considerations for Asteroid Despin via Neutral Beam Emitting Spacecraft," Presentation at Mid Atlantic Chapter of SSPI Student Engineering Competition

Chapter 2: Literature Review

Asteroid deflection can be divided into two major categories: high impulse and slow push. High impulse refers to immediate momentum changes of the asteroid to deflect it from an Earth impact whereas slow push is accomplished over years or decades. Slow push, while not providing immediate avoidance of an impact, enables fine control of an asteroid's final orbit. We will review the variety of asteroid deflection proposals in literature along with the limited literature on altering the rotation state of an asteroid. Our goal is to use neutral beams for asteroid deflection and we will review the past work in neutral beam development. Evaluating the benefits and shortcomings of proposed asteroid deflection and de-spin concepts, we develop our own requirements for an alternative asteroid control method.

2.1 Asteroid Deflection Methods

A kinetic-nuclear impactor [27, 28] uses two high impulse deflection methods: a kinetic interceptor that creates a crater and a nuclear warhead that detonates in or above the crater to expel asteroid material and deflect it from an Earth impact. This two-stage approach creates a significant trajectory change over a short period and is preferable for large asteroids or short warning windows.

Kinetic impactors could also be used exclusively to deflect an asteroid, using the force of the impact and the ejecta to alter the orbit. Deep Impact [29] demonstrated the ability to target a small body with a hypervelocity impactor and the proposed Don Quijote mission [30] would have included an orbiter at an asteroid to observe the impact and the long-term effects. To improve upon this technology, other target asteroids have been identified as candidates for demonstration missions [31]. To demonstrate a kinetic interceptor, AIDA aims to alter the orbit of Didymos' moon [32]. This mission will directly observe the impact dust plume from the interceptor spacecraft, measuring both the size distribution and momentum enhancement. Refining estimates on momentum enhancement from AIDA is important to understand asteroid strength and the effectiveness of single or multiple kinetic impactor missions.

Propulsive deflection via attaching to and tugging on the asteroid (Scheeres and Schweickart [33]) or hovering and using the ion propulsion plume exhaust for deflection (Bombardelli *et al.'s* [12, 18]) provide finer control of the asteroid than high impulse deflection methods. Using low-thrust trajectories requires that the system arrive at the asteroid years in advance of a potential impact. It is preferable that deflection occurs during a perihelion event as this will be the most efficient ΔV maneuver. Because of the low-thrust nature of the concepts from [12, 18, 33], years of deflection time is required to provide sufficient deflection. For example, in [12], deflection of 2011 AG5 (a 4 billion kg asteroid) with a 1N thruster would require a start date of 5 years before impact and constant deflection for 2 years to achieve a deflection of 1 Earth radii. Grappling and tethering to an asteroid is difficult

as knowledge about the strength and composition of the asteroid would be needed to design the end effector. For the current population of PHAs, only 91 (5%) [34] have a Tholen [35] or SMASSI [36] spectral designation. Either several end effectors would need to be used to ensure mission success or knowledge gained through a flyby or close encounter that allowed the study of the asteroid would be required.

The gravity tractor, an example of a slow push method, uses a heavy spacecraft that closely follows an asteroid, altering its orbit through gravitational attraction. Significant deflections take years to achieve and even with the optimal duty cycle for coast and thrust phases from Olympio [37], a deflection of 100km was achieved in 5 years for a 130m diameter asteroid. Mazanek [38] improved upon the gravity tractor by recognizing the increased deflection efficiency if the spacecraft was able to lift a boulder from the surface. This would increase the total spacecraft mass and enhance the gravity tractor effect. Fine control of asteroids, such as that offered by gravity tractors or propulsive methods, expands mission objectives from not only deflection but to moving asteroids to orbits that can be visited frequently for future study or resource acquisition, as has been suggested with the Asteroid Rendezvous and Redirect Mission (ARRM) [39]. It has also been proposed to meet the objective of future observation and utilization by moving asteroids to libration points [40].

Alternatively, laser ablation described by Lubin *et al.* [41] could prove to be a long-term, sustainable solution for planetary defense. Using a kilometer-size laser-phased array orbiting Earth, [41] envisions converting solar energy to laser energy that would be capable of sublimating asteroid surfaces. Through sublimation, the asteroid plume would act as a thruster pushing it away from an Earth collision;

given enough time the phased-laser array could eliminate the asteroid. While [41] addresses asteroids rotation, they do not evaluate its effectiveness against tumbling asteroids, which may pose a problem for the illumination time to start sublimation.

Multiple mass drivers on the surface of an asteroid are an additional option for planetary defense and Old [42] determined their effectiveness for moving Apophis out of the resonant-return keyhole that would put it on an impact trajectory for 2036 during the 2029 close approach. Of the issues for using mass drivers, power and the ability to secure onto a loose, granular surface would be significant engineering obstacles. Requiring power and mass limits within current or near-term technology limits mission profiles to those that can be achieved in the near-term.

Another possible slow push method is to use mirrors to enhance the Yarkovsky effect, as described by Vasile and Maddock [43]. In this proposal, a large mirror reflects sunlight onto the surface causing sublimation which acts as a thruster. Thermal emission, also known as the Yarkovsky effect, assists in acting as a weak thruster for this concept. Vasile and Maddock's [43] method is not without its challenges. Sublimated gases will inevitably contaminate the mirror leading to a less effective reflector, which will eventually cease to have the required power to sublimate the surface. Another challenge is that the mirror required to significantly alter the asteroid trajectory would be tens of meters in size.

2.2 Asteroid De-spin

Asteroid de-spin is not a thoroughly explored part of planetary defense. Controlling the spin velocity is important as many asteroids are likely tumbling bodies [33, 44]. Deflection methods that require attachment onto the asteroid [33] or interacting with the surface [38, 41–43] are complicated by an unpredictable rotation state of the asteroid. Attaching onto a tumbling asteroid with a tether such as Scheeres [33] results in the spacecraft likewise tumbling, making control difficult. Landing on the surface of an asteroid for obtaining a boulder [38] is also complicated by a chaotic rotator as tracking with the surface during descent may not be possible. For [41, 43], each method requires energy concentration over an area in order to sublimate the asteroid. Targeting an area can not be achieved if the asteroid is chaotically rotating. Olds [42] envisions using a mass driver, which fundamentally requires that the mass be ejected along a certain trajectory. Predicting the moment to eject the mass would not be possible with a chaotic rotator. Gao and Wu [45] propose using a tethered solar sail to de-spin an asteroid: for Apophis, a 10^5 m^2 sail would require 1000 days to arrest the rotation. The tethered solar sail would attach directly to the asteroid and be positioned at an equilibrium point around the asteroid to avoid relative orbit problems in twisting the tether. Solar radiation pressure acts upon the solar sail and provides a torque to de-spin the asteroid.

Propulsion de-spin for stably rotating bodies has also been proposed using a tethered ion engine [33]. In this proposed method, a spacecraft equipped with an ion engine would mechanically attach to the surface via a tether and de-spin the asteroid

over a period of time. After de-spin, the spacecraft would be able to re-orient the asteroid to tug it to another trajectory.

2.3 Prior Development of Neutral Beams

Neutral beams for the purpose of heating a fusion toroidal plasma was proposed by [16]. Neutral beams are created by globally neutralizing an ion beam and deflecting the remaining ions from the beamline. The main premise behind a neutral beam is that it does not introduce electric or magnetic fields in order to heat a plasma. Stix [16] showed that for an ion source of sufficient current, a neutral beam could be developed that would be capable of heating a fusion toroidal plasma. He also presented an analytical expression for predicted neutralization through recombination. In [46] they investigated the components of a Deuterium neutral beam by species and energy. The ions were deflected using a magnet and their current was determined through the use of Faraday cups. The neutrals (not being affected by the magnetic field) were measured using a calorimeter which was designed to capture 90% of the neutrals. The magnetic field could also be removed to determine consistency in measurement between the Faraday cup an calorimeter in terms of total current. For multi-species, high energy hydrogen ion beams, Kim [47] calculated the change in species fractions for background gas density. This demonstrated the importance of initial species fractions at specific energies and the background density needed to transform the ion beam into a neutral beam. Menon [15] covers a detailed summary of neutral beam development in the 1970s and summarizes the

advantage it has over ohmic heating for tokamaks and stellerators. He also presents design principles and methods for high power neutral beams covering the types of plasma generators, acceleration of ions, neutralization, and ion dumps. In high power neutral beams it was recognized that the calculated gas linear density from the observed neutralization measurements did not match the predictions for gas inflow [48]. Direct elastic collisional losses from ion to background gas was ruled out for ion energies in the 10 - 100 keV range [48]. They show that sources of indirect heating are pronounced by molecular disassociations of ion beam ions and neutralizer plasma electrons. However, these issues only start at electron temperatures of 10 keV and for high gas flow rates [48]. Modern work on neutral beams has focused upon the ITER [49, 49, 50] and EAST [51] tokamak reactors. These neutral beams are designed for Mega-Watt applications to heat the fusion plasma. One exception is neutral beams for materials processing [52]. This low-energy application (10 - 200 eV) directs accelerated ions to a grounded reflector plate where they are neutralized by collision and bounce off to strike a substrate downstream.

2.4 Requirements for an Alternative Asteroid Deflection Method

After reviewing the existing asteroid deflection technologies, we have identified high level requirements for a new deflection technology that would avoid many of the weaknesses of the currently discussed methods. Specifically, to deflect 100-400m diameter asteroids, the method should:

1) Not require a spacecraft to mechanically attach to the asteroid,

2) Avoid the creation of an unsafe operating environment for the spacecraft,

3) Maintain reasonable power and mass for current or near-term technology,

4) Be throttleable to evaluate deflection effectiveness and reduce errors in deflection,

5) Compare favorably with the time other slow-push methods require to deflect an asteroid,

6) Include an assessment of the risk in losing a spacecraft or thruster during a deflection campaign.

Methods that affix to asteroids invariably require prior knowledge of the asteroid composition and structural strength. These data are not widely known for the current population of Near Earth Objects (NEOs) or in the smaller subset of Potentially Hazardous Asteroids (PHAs). Therefore, either a scouting mission or a chance close flyby of Earth would be required to assess an asteroid's structure. As previously discussed, sputtered particles are an environmental danger to spacecraft. The same is true for sublimation so any method must find a way to minimize the effects these have on a spacecraft. Additionally a limit on power and mass stems from designing a mission that could be deployed in the near term and does not use low- technology readiness level (TRL) components. From an operational standpoint, EGT has fine control over altering the asteroid trajectory, something that is difficult to achieve in high impulse methods (i.e. multiple kinetic impactors). While Thiry and Vasile [61] conclude that kinetic impactors and laser ablation are the

most effective non-nuclear deflection methods, their analysis excludes technology readiness. Propulsive deflection does offer a more near-term solution given the past and current use of ion propulsion for spacecraft. Propulsive methods can potentially offer high fidelity control as well. We further focus our method to achieve similar or reduced deflection times as compared to other slow-push methods. Finally, knowing how thruster or spacecraft loss affects deflection success informs the architecture for long duration deflection missions.

In order to achieve asteroid deflection and control and meet these objectives, we are developing a new type of thruster called a neutral beam emitter to slow the tumbling motion of asteroids and deflect them. Several spacecraft equipped with our thruster would rendezvous and act upon the asteroid until successful deflection is achieved. This requires formation flight, such as that explored by Baresi *et al.* [62] for triaxial, slow-rotating asteroids. This thruster is unique from [63] as it uses gas diffusion neutralization instead of ion compression. A neutral beam at an asteroid would mitigate the risk of electrostatic dust being attracted to the spacecraft as there would no longer be a quasi-neutral plasma interacting with the environment, as is the case with typical ion propulsion. Instead, the impinging beam would consist of only neutral particles that would not add to the charge density already on the surface. Neutral beams have been used in tokamaks to provide heating to the toroidal plasma without introducing electric and magnetic fields to the plasma, affecting its confinement [15, 51, 64, 65]. These devices typically operate at 10's of kilo-electron volts and deliver a power on the order of megawatts. This scale of energy and power is impractical for modern spaceflight. However, it is possible

to scale down this technology to the kilowatt range so that it can be used for space propulsion. Using neutral beam propulsion methods, it is possible to avoid modifying the electrical charging of the asteroid's surface while maintaining the efficiency of electric propulsion in asteroid deflection. For this study, we choose an argon as the propellant due to its good charge to mass ratio and high global availability.

Chapter 3: De-spin and Deflection of Hypothetical Asteroid 2017 PDC

This chapter will assess the efficacy of the NBAC method by applying it to the hypothetical asteroid 2017 PDC. We will use the General Mission Analysis Tool (GMAT) to determine the effectiveness of NBAC in deflecting asteroids of a variety of sizes and spectral types. We will also evaluate the effect of spacecraft failure on the ability of NBAC to deflect 2017 PDC. Finally we will demonstrate that neutral beams have the capability to de-spin and partially de-spin a variety of asteroids. Combining the work from these sections, the propellant mass needed per spacecraft to de-spin and deflect hypothetical asteroid 2017 PDC will be presented.

3.1 Deflection of Hypothetical Asteroid 2017 PDC

The primary mission of NBAC is to provide a deflection capability that bridges the design space between slow and fast impulse methods. As a propulsive deflection method, it must follow the asteroid over a period of months to years to achieve sufficient deflection. The fictitious asteroid 2017 PDC was created for the 2017 IAA Planetary Defense Conference as a baseline asteroid for the purpose of a deflection exercise [66]. Initial information for the asteroid, which is discovered on March 6,

2017, predicted a 1% chance of impact on July 21, 2027; this gives about a 10-year period to deflect the asteroid. The asteroid was estimated to be between 100m - 250m in size (due to the uncertainty in albedo) and on an elliptical 0.88 AU x 3.60 AU orbit. The greatest deflection that NBAC can supply to the hypothetical asteroid 2017 PDC is achieved by thrusting during perihelion approach all the way through perihelion. 2017 PDC has two perihelion passages (2020 and 2024) before the potential collision with Earth in 2027.

Low-thrust deflection of an asteroid using the 2017 PDC orbit with NBAC is calculated using the General Mission Analysis Tool (GMAT) [67]. For the present study, we investigated a range of asteroid masses and deflection times and considered only non-relativistic, n-body gravitational forces acting on the asteroid from the Sun and planets. When the asteroid was more than 1 million km from Earth, (approximately the radius of Earth's sphere of influence (SOI)), all planetary bodies were included as point masses for integration of the orbital dynamics equations. Point masses for Venus and Jupiter were found to be significant in determining the orbit. Inside Earth's SOI, Earth was the primary attractor using the JGM-2 gravity model and the Moon was included as a point mass. We utilize this patched conics approach as the expected perturbations for the asteroid due to other planetary bodies when inside Earth's SOI is minimal as it impacts Earth within a day. The initial state of the 2017 PDC orbit at Jan 1, 2018 00:00:00.000 was acquired through JPL's HORIZONS system and fed into GMAT to determine all future states using a RK89 integrator. With no deflection, GMAT predicts an Earth impact on July 21, 2027.

During deflection, all thrust is directed through the center of mass of the asteroid along its instantaneous velocity vector in the VNB (Velocity-Normal-Binormal) frame. It is assumed that four NBAC engines producing 70 mN each are thrusting during the deflection campaign. This corresponds to each NBAC engine producing a 10 keV beam with a plasma current of 0.94 A operating on argon propellant. Additionally, it is assumed that the spacecraft fly close to the asteroid in that the entire thrust plume impinges on the asteroid. Deflection is calculated by the GMAT simulations showed that sufficient deflection (closest approach altered to a 200 km altitude pass or greater) with NBAC was achieved for thrusting durations between 240 and 420 days (with diminishing returns at greater than 420 days of thrusting), where the duration was equally split before and after the perihelion approach in Sept. 2020. The closest approach distance is referenced to the Earth center. The deflection maneuver is assumed to take place during the first (2020) perihelion passage, as there are minimal gains achievable when the deflection is attempted at 2024 due to the short time before impact.

In Scheeres *et al.* [68] and Carry [69], densities of several asteroid types are given considering a wide range in density and macroporosity, due to the existing uncertainty in asteroid interior structure. There is significant uncertainty in the macroporosity of asteroids, as they may be either a loose collection of boulders held together by cohesion or a monolithic single-body structure. Scheeres *et al.* [68] note that the density data are biased toward binary asteroids and asteroids visited by spacecraft. There has been no large survey of sub-kilometer asteroids at present, so we assume that they have similar densities to their larger counterparts. We use

the densities from Scheeres *et al.* [68], shown in Table 3.1, for our analysis relating uncertainties in asteroid composition to deflection performance. S-type asteroids are fairly bright stony asteroids composed of iron and silicates [36]. C-type asteroids are carbonaceous chondrites with a dark albedo and among the most common of the asteroid spectral types with several different subclasses [70]. B-types such as Bennu, the target for the OSIRIS-REx mission, are made of silicates and have a higher albedo [70]. Finally Xc asteroids are a class of X-group asteroids that have a higher density and likely have metallics [36] although there is limited information on this spectral class. The S, C, and B types have overlapping densities with the Xc being the outlier.

Table 3.1: Densities of asteroid classes (Scheeres *et al.* [68])

Class	Density (g/cm^3)	Standard Deviation (g/cm^3)
S	2.72	$\pm$ 0.54
C	1.33	$\pm$ 0.58
B	2.38	$\pm$ 0.45
Xc	4.86	$\pm$ 0.81

Extending the work by DeCicco and Hartzell [71] for low-thrust asteroid maneuvering, and given the orbital parameters and varying densities described above, we calculate the deflection achieved by the proposed four spacecraft NBAC system, as a function of the spectral type of the asteroid. For a 420-day constant operation of NBAC, Fig. 3.1 plots the density and standard deviation for C, B, S, and Xc-type

asteroids. The deflection achieved for each of these types of asteroids is truncated by the minimum close approach altitude radius of 200km. Of the four spectral types considered, C-type asteroids have the greatest uncertainty in deflection due to the large uncertainty in density of this spectral class. Overlapping uncertainty in density for B and S-type asteroids gives similar deflection with the NBAC system. For a 420 day deflection campaign, a 60m radius S-type asteroid could be deflected from 7300km to 9000km (depending on its density) from the Earth's center, both extremes representing successful deflection. However, in the case of a 70m radius asteroid, S-type and B-type (on the denser extremes) and all Xc-type asteroids would not be successfully deflected.

Fixing the spectral density to the mean value (given in Table 3.1), we calculate the maximum radius asteroid that could be successfully deflected (defined as a distance of closest approach from the Earth surface greater than 200 km) given a deflection campaign duration, see Fig. 3.2. Asteroids larger than 60m radius can be deflected assuming densities consistent with C, B, and S types. Due to the large density of Xc types, only smaller (<60m) asteroids can be deflected. However, the predictions for Xc asteroids provide a conservative calculation for the worst-case scenario when the material makeup of the asteroid is unknown. As discussed before, it is likely that for a given PHA, there will not be spectral class defined before the mission design begins. For the subsequent analysis, we define deflection failure to occur if the maximum asteroid radius able to be deflected falls below that of the corresponding Xc-type asteroid radius in Fig. 3.2 for a given deflection duration.

We investigate partial failure of NBAC and how it affects mission success.

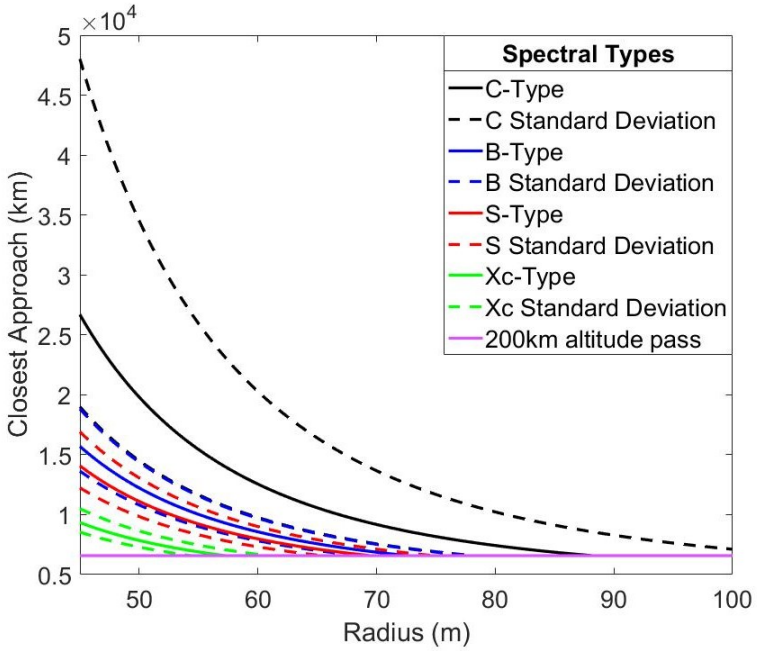

Figure 3.1: Closest approach achieved through 420 day duration, 4 spacecraft NBAC campaign, as a function of asteroid size and spectral type. Standard deviation lines indicate the uncertainty in spectral type density (as described in Table 3.1). Low-density C-type asteroids have a larger uncertainty in projected deflection than other spectral types along with a large difference in asteroid size that can be successfully deflected due to the large range in density of these asteroids.

Possible failure modes for NBAC include a failure of GNC where the spacecraft thrusts in the wrong direction and thruster failures. Failure of the GNC would make the spacecraft uncontrollable as NBAC requires operation of two thrusters with the spacecraft positioned such that one is directed towards the asteroid for deflection and the other is used for station keeping. The advantage of electric propulsion is the high achievable specific impulse owing to the high velocities in plasmas. Degradation and failure of the accelerating grids for the plasma would leave NBAC as a low specific impulse cold gas thruster. To evaluate the impact of

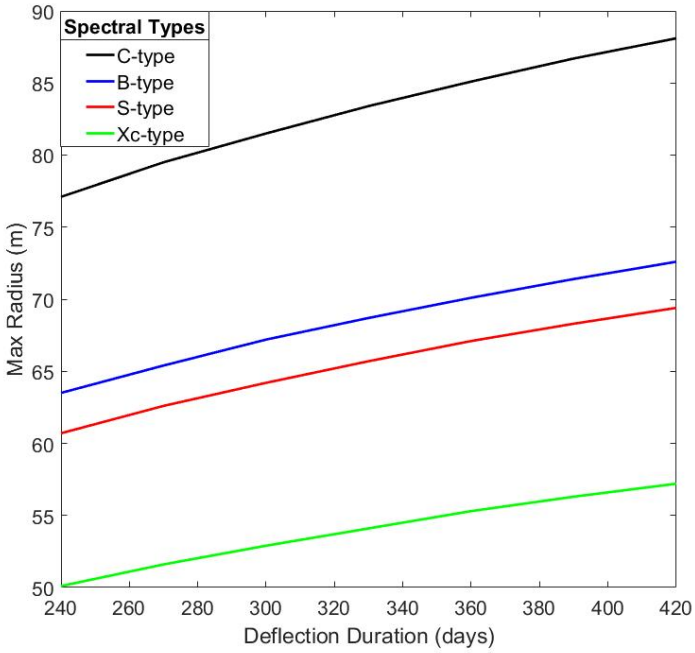

Figure 3.2: Maximum radius for an assumed spherical asteroid of the mean density for the considered spectral classes (see Table 3.1) that can be deflected using a 4 spacecraft NBAC campaign for a given deflection campaign duration. Xc-type asteroids, while only having a limited range of sizes that can be successfully deflected, provide a relevant conservative calculation for deflection given that the many asteroids do not have a known spectral type.

NBAC thruster failures, we set a time in the GMAT script for which the effective thrust on the asteroid is lowered. For example, considering a baseline thrust of 280 mN on a 240 day deflection campaign, we induce a single thruster failure after one quarter of the deflection campaign has elapsed (e.g. day 60) by lowering the thrust to 210 mN for the remainder of the deflection campaign. Fig. 3.3 plots the deflection achieved as a function of asteroid size, considering the loss of one or two thrusters (out of four thrusters total) at a particular elapsed mission time (e.g. after 25% of the campaign duration has elapsed). A significant loss in thrust (two

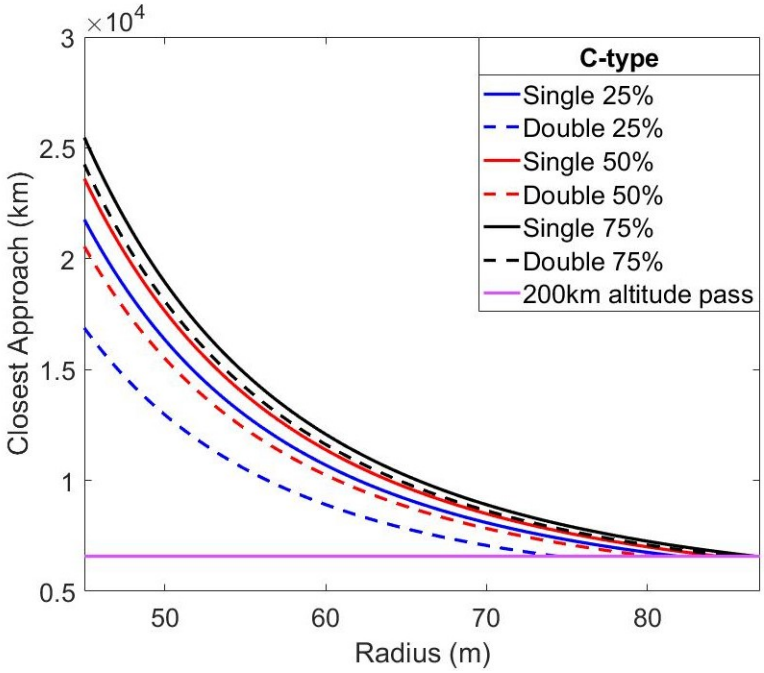

Figure 3.3: Closest approach as a function of asteroid size, considering a C-type asteroid and a 420 day deflection mission. "Single" ("double") indicates the failure of one (two) NBAC spacecraft. The percentage indicates the percentage of elapsed mission duration when the thruster failure occurs. For a 420-day deflection mission to a C-type asteroid, significant failure after 25% of the mission time can reduce the asteroid radius for successful deflection to 74m. Losing a singular thruster halfway through the mission does not significantly affect the asteroid radius able to be deflected under this long-term mission.

thrusters at 25% elapsed deflection time) reduces the asteroid radius able to be deflected by 16% from the nominal scenario.

We can compare across the different spectral types for the bounding cases of single and double thruster failure for 25% and 75% elapsed mission duration in Fig. 3.4. The effect of early stage failure (e.g. at 25% elapsed mission duration) reduces the asteroid size NBAC can successfully deflect but they all (except the Xc-type) are greater than the 57m minimum radius for complete failure in a 420-

day deflection campaign. There is only one perihelion passage that is advantageous for deflection with NBAC; the losses incurred from failure in this first perihelion passage could not be effectively recovered through deflection during the Feb 2024 perihelion passage. A double thruster failure at 25% elapsed mission duration for a C-type asteroid truncates the minimum asteroid radius able to be deflected to less than 75m. Comparing that result to Fig. 3.2, this failure causes the 420 day deflection campaign to be less effective than a 240 day campaign with all four NBAC thrusters operating, demonstrating the need to act upon asteroids early in deflection missions to reduce the total risk for failure. For a 420 day deflection campaign, the deflection (as measured from the Earth center at closest approach) attained for a 1 $\times 10^9$ kilogram asteroid with a double thruster failure after 25% of the mission decreases from a radius of 14500 km to 10000 km (a 31% decrease). There is also a shift in the asteroid mass that can be successfully deflected by NBAC due to these failures. With no failures, NBAC can deflect a 3.8 $\times 10^9$ kg asteroid, but this falls to 2.3 $\times 10^9$ kg, a 39% reduction, for a failure of the two thrusters 25% of the way into the deflection mission.

Even with two thrusters failing 25% into the deflection mission, NBAC's use of an electric propulsion system is still able to deflect some smaller asteroids that could cause an airburst event or in the rare case, impact the surface. Airbursts can cause weak structures to fail, windows to shatter, and result in minor or severe injuries. Both the Chelyabinsk [72] and Tunguska [73] events exhibited a significant amount of damage to the ground without being major cratering events. A four thruster NBAC architecture is able to handle a variety of asteroid spectral types and sizes with some

tolerance to uncertainty in asteroid density. Additional thrusters could successfully deflect larger, more dense asteroids. Considering a multi-spacecraft architecture, the propellant mass necessary for deflection is distributed amongst the spacecraft. For a 70 mN NBAC thruster and accounting for station keeping, Table 3.2 presents the propellant usage per spacecraft assuming that there is constant operation of the thruster. This relatively low propellant requirement is a result of the high specific impulse achievable with neutral beam propulsion.

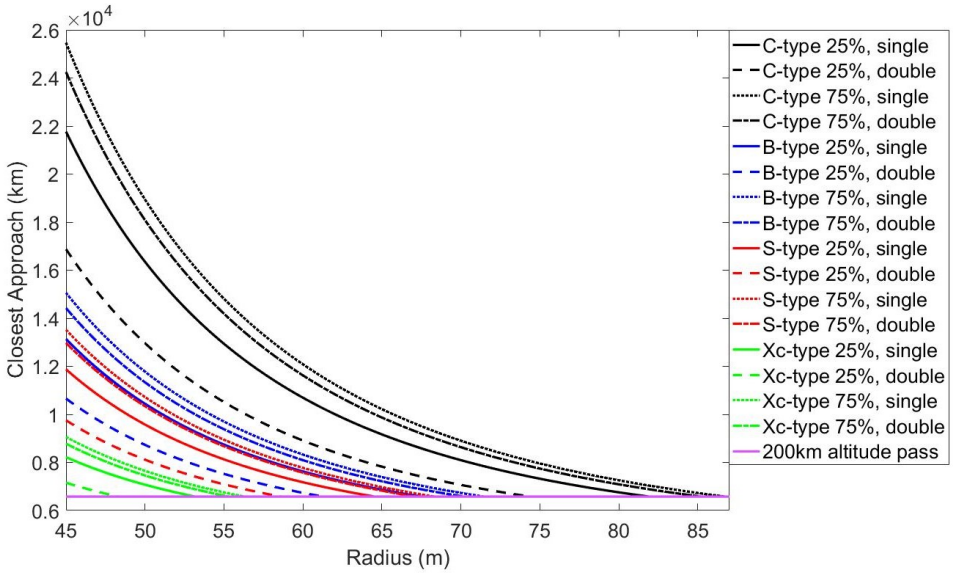

Figure 3.4: Closest approach as a function of asteroid radius for various spectral types in a 420 day deflection campaign. Percentages indicate the instance at which thruster failure occurs (e.g. 25% is 105 days into deflection mission). Single and double indicate whether one or two thrusters has failed at this instance. Decreases in asteroid radii that can be effectively deflected when there is system failure does not preclude C, B, and S-type asteroids from meeting the 57m minimum set by the Xc-type asteroid. Xc-type asteroids are not failure tolerant within the NBAC mission profile for this singular perihelion passage deflection.

Table 3.2: Propellant usage per spacecraft in a four thruster NBAC system for asteroid deflection

Deflection Duration (days)	Propellant Mass per Spacecraft (kg)
240	25
300	31
360	38
420	44

3.2 Arresting the Rotation of 2017 PDC

A rotating asteroid poses a problem for laser ablation, kinetic impactors, nuclear deflection, and tethered systems [45]. In the case of laser ablation, heating a fixed point from a distance would prove difficult as the surface being heated rotates away from the source. For a medium or fast rotator being deflected either kinetically or through a nuclear device, the ejected material would not necessarily act through the mass center of the asteroid. For tethered methods, the difficulty in maintaining a taught tether during deflection while the body is rotating can not be ignored. Stabilizing the rotation of an asteroid is one of the major goals for NBAC. We discuss the dynamics of asteroid control, estimations of asteroid spin rate and unstable criteria, and NBAC's performance for total and partial arrest of asteroid rotation. Nothing is known about 2017 PDC's rotational state at the time of discovery, given that very limited arcs have been observed in this hypothetical scenario. We consider an asteroid rotating with a angular velocity $\vec{\omega}_{B/V}$ with respect to the VNB frame

and align this with the inertia tensor $\mathbf{I}_B$ in the body-fixed frame with the principle axis so that its angular momentum is:

$$\vec{H}_B = \mathbf{I}_B \vec{\omega}_{B/V} \tag{3.1}$$

Using the transport equation and noting our choice in aligning $\mathbf{I}_B$ with the principle axis, the angular momentum in the VNB frame changes with an applied torque, $\vec{\tau}_B$ as:

$$\dot{\vec{H}} = \mathbf{I}_B \dot{\vec{\omega}}_{B/V} + \vec{\omega}_{B/V} \times \left(\mathbf{I}_B \vec{\omega}_{B/V}\right) = \vec{\tau}_B + \vec{\omega}_{B/V} \times \left(\mathbf{I}_B \vec{\omega}_{B/V}\right) \tag{3.2}$$

We derive a total angular momentum description (both rotational and orbital) in the inertial frame, I, for a rotating asteroid under an external torque noting that $\dot{\mathbf{I}}_B = 0$ as the body tensor is aligned with the principle axis (shown in Fig 3.5):

$$\dot{\vec{H}}^I_{TOT} = m_A(\vec{R} \times \dot{\vec{V}})^I + \mathbf{C}_{IV}[\vec{\tau}_B + \vec{\omega}_{B/V} \times (\mathbf{I}_B \vec{\omega}_{B/V}) + \vec{\omega}_{V/I} \times \vec{H}^V_{ROT}] \tag{3.3}$$

where $\vec{R}$ is the position of the asteroid center of mass in the inertial frame, $\dot{\vec{V}}$ is the asteroid acceleration of the center of mass in the inertial frame, $\vec{\omega}_{V/I}$ is the angular velocity in the VNB frame with respect to the inertial frame, $\vec{H}^V_{ROT}$ is the total angular momentum in the VNB frame, and $\mathbf{C}_{IV}$ is the transform tensor from the VNB frame to the inertial frame.

From the above equation we then define $\dot{\vec{V}}_I$ through the classical two-body orbital description with a force applied, $\vec{F}_{Bi}$ in the body-frame:

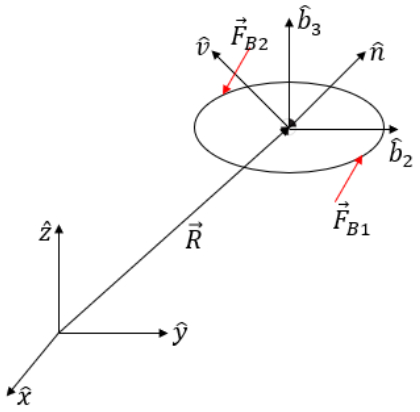

Figure 3.5: Schematic showing the body ($\hat{b}$), VNB ($\hat{v}, \hat{n}$), and inertial reference frames used to describe asteroid motion. The forces are applied in the body frame. If the forces are balanced on the moment arms, there will be no net $\vec{F}$ and the asteroid orbital trajectory will not be altered.

$$\dot{\vec{V}}_I = \frac{-\mu}{|\vec{R}^3|}\vec{R} + \mathbf{C}_{IV}\mathbf{C}_{VB}\sum_i \frac{\vec{F}_{Bi}}{m_A} \tag{3.4}$$

where μ is the gravitational parameter of the Sun, $\mathbf{C}_{VB}$ is the transform tensor from the body frame to the VNB-frame, and m_A is the mass of the asteroid. If the spacecraft are positioned at opposite ends of the asteroid as shown in Fig. 3.5, then $\sum_i \vec{F}_{Bi} = 0$. If we are able to maintain such a configuration about the asteroid during the de-spin maneuver, then there should be little to no effect on the orbit of the asteroid during that period. However, in practice, this configuration will be difficult to maintain so it is important to know the spacecraft positions relative to one another to determine how they affected the asteroid's orbit. One advantage of NBAC is that it is possible to correct any errors in thrust direction during either the de-spin or deflection phase of asteroid control.

To determine the range of spin rates for the distribution of asteroid sizes for

2017 PDC, we consult the JPL Small-Body Database. In Fig. 3.6, we plot the rotation rate as a function of asteroid size, for the subset of asteroids whose rotation state has been characterized. There is limited data on the rotation rates of asteroids between 100m - 250m due to the difficulty of observing rotation rates for small bodies. For an asteroid with a diameter $\simeq$ 150m, we can expect a rotation period anywhere between 0.3hr to 51hr, the faster of which is likely to be a monolithic, boulder.

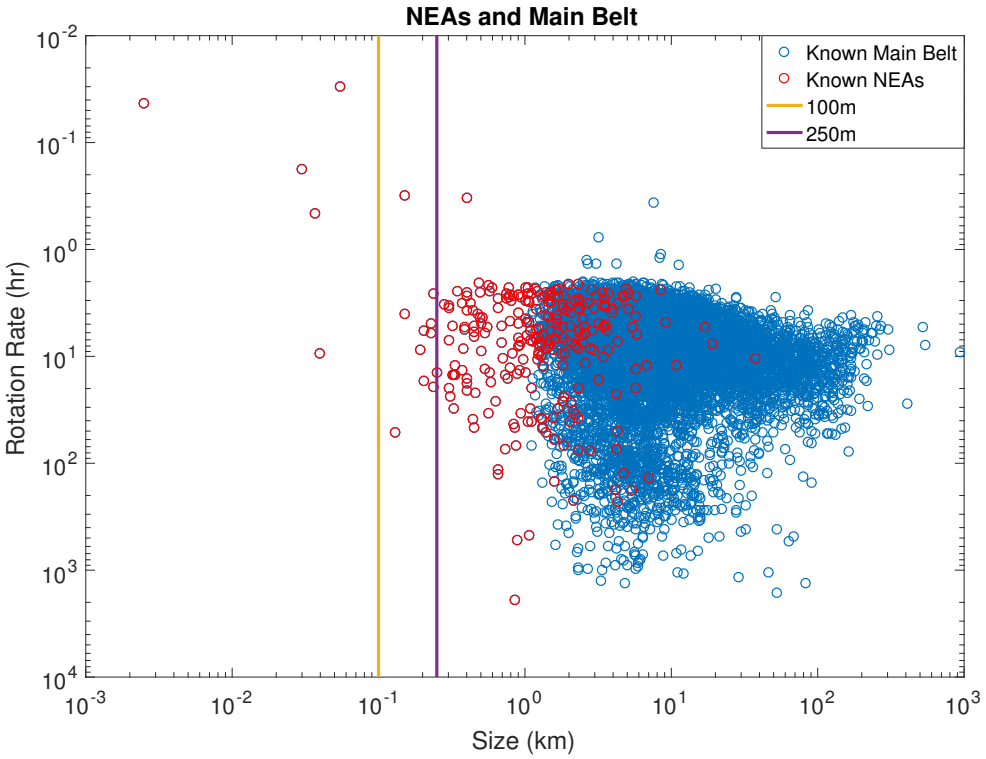

Figure 3.6: Known rotation rates as a function of asteroid size obtained from the JPL Small Body Database.

Discussion in Scheeres and Schweickart [33] suggests that there is a spin rate limit for rubble-pile asteroids, above which they will disassemble. This limit is

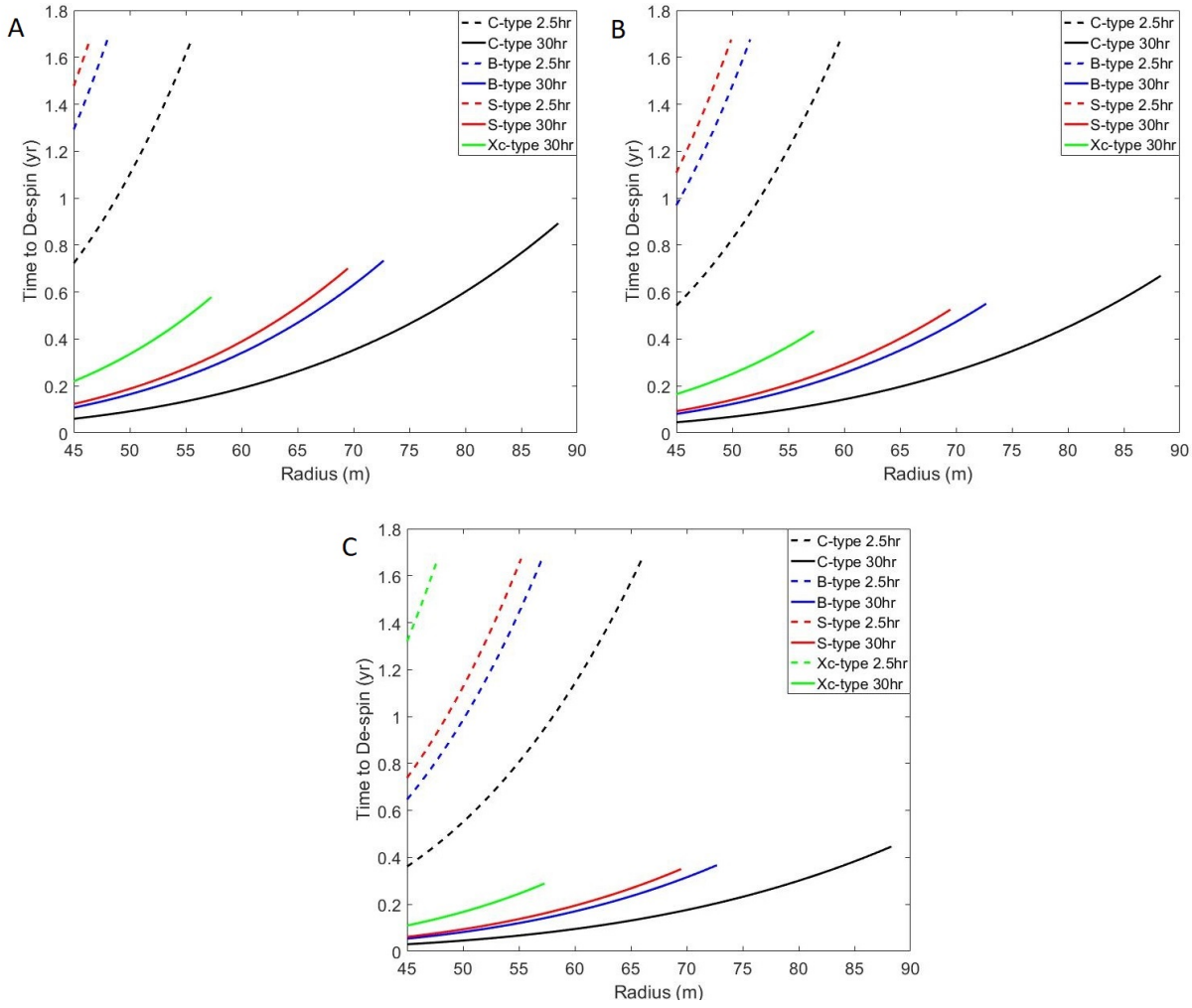

Figure 3.7: The time to slow asteroid rotation as a function of asteroid type and size. A: full asteroid rotation arrest B: 75% rotation arrest C: 50% rotation arrest. Slowing the asteroid rotation is achievable within a wide range of spectral types.

evident in the sharp cutoff seen in Fig. 3.6 for rotation periods faster than about two hours, above which there are only a couple of stray asteroids. Often spin rate data are obtained via light curves so there is still some bias in the data towards Main Belt asteroids since there have been more frequent, longer periods of observation for this population. However, the initial data from NEAs suggest that they follow the

same clustering in size and rotation rate so we can be confident in the current data in establishing the spin rate limit before an asteroid must have internal strength or as we denote in the asteroid-fixed frame, the unstable equilibrium in cohesion and centrifugal force. Thus we establish our boundary for stable asteroids to be at this cutoff of approximately 2 hrs, above which rubble pile asteroids risk disassembly.

For de-spin, we assume a roughly spherical asteroid rotating about a singular axis at some steady rate w_0 with no external accelerations. We require partial or complete de-spin to occur within a half asteroid orbital period; this brings the total time spent acting upon the asteroid, with the 420 day deflection opportunity described in the previous section, to approximately 2.8 years, meeting our time requirement of less than five years. Additionally, we require the asteroid to then be deflected by at least a 200km altitude to Earth at its closest approach. For the subsequent discussion, we again consider a four-thruster NBAC system operating at 0.28 N of combined thrust.

It is worthwhile to attempt total de-spin of an asteroid so that a separate, future spacecraft could attach a cable and tow the asteroid to a more favorable orbit. Full de-spin of asteroids can be achieved with those rotating with a period of at least 2 hours for asteroids between 100m - 250m. In Fig. 3.7, we present the time required to totally or partially arrest the rotation of asteroids, considering only those that can be successfully deflected (closest allowed approach of 200 km altitude). The requirement that the de-spin maneuver must take less than half of one orbital period severely limits the range of fast rotators than can be fully arrested, but it does not affect cases where the rotation period is 10 hrs or greater.

A 2.5 hr rotator can be completely de-spun for an asteroid radius of 50m with a $\rho \sim$ 2 g/cm^3 (this is in the range of C and B-type asteroids). Full arrest of the rotation is not necessarily required: decreasing the rotation rate will increase the strength of the body (by decreasing the centripetal acceleration). Additionally, slowing the rotation rate by 50 - 75% would also simplify the process of physically attaching to an asteroid and assist in making landings easier. Slowing the rotation of a 50m S-type spherical asteroid by 75%, increases the surface gravity from 1.36×10^{-5}m/s^2 to 3.65×10^{-5}m/s^2, a 168% increase thus improving the asteroid strength. Fig. 3.7 shows the time required to arrest or partially arrest the rotation of an asteroid, as a function of the asteroid size, spin rate, and spectral type. The 2.5 hr rotator can be partially arrested and deflected for a 50m radius asteroid in the density range of S, C, and B asteroids.

Using the full NBAC system means that the propellant mass is equally subdivided amongst the spacecraft to control the asteroid. Fig. 3.8 shows that we can achieve total de-spin for wide range of asteroid sizes using less than 60 kg of argon propellant per spacecraft. Having a campaign with multiple spacecraft reduces the consequences of a spacecraft failure. As we approach longer rotation periods ($P_0 \geq 20$ hrs), many solutions require less than 40 kg of propellant per spacecraft.

In Fig. 3.9 we show the calculated time to de-spin asteroids rotating faster than the break-up limit, slowing their rotation rate by 25%. The NBAC system is not suitable to slow the rotation of asteroids with rotation periods of less than 0.1 hour. However, half hour rotators could be moderately slowed, even though their rotation would not be fully arrested. While Fig. 3.9 shows that it is difficult

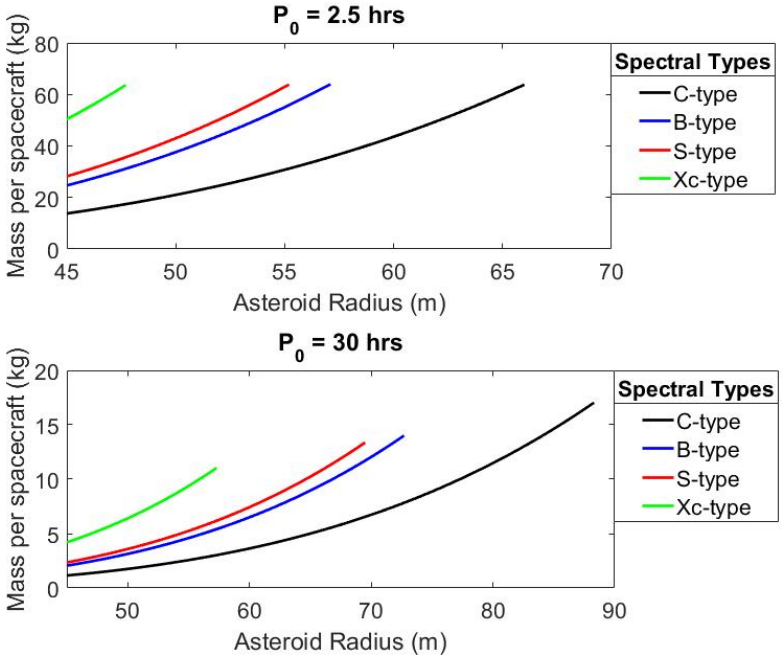

Figure 3.8: Propellant mass per spacecraft required to totally arrest the rotation of an asteroid using a four thruster NBAC system operating with a 10 keV beam and producing 280 mN total thrust. Many asteroid types can be completely de-spun with less than 60 kg of propellant.

to partially de-spin these fast rotating asteroids, there is a design space for NBAC to reduce the angular momentum of the asteroid. For a 50m asteroid, the NBAC system can partially arrest a half hour rotator by 25% with $\rho \leq 2$ g/cm^3 and an hour rotator with $\rho \leq 3$ g/cm^3. A more powerful NBAC system (drawing more electrical current) could yield a larger impact on these fast rotators. Whether an asteroid is a fast or slow spinner, heavier asteroids will be more difficult to de-spin due to their higher moment of inertia and thus require longer periods of time.

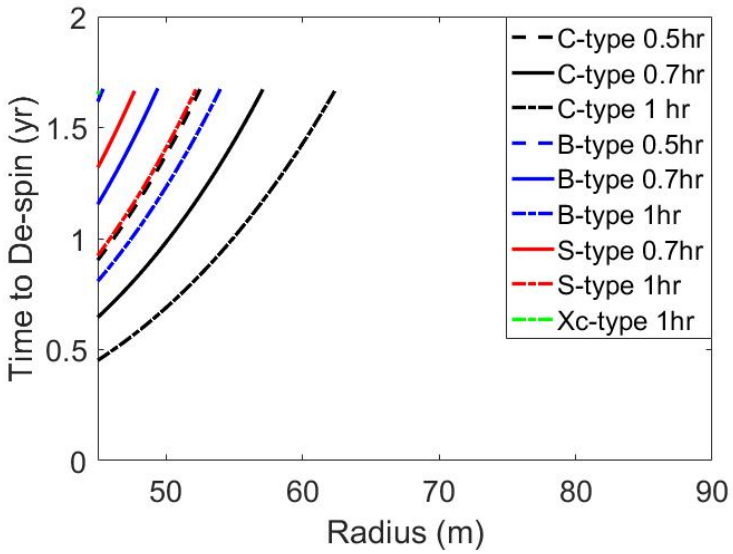

Figure 3.9: Time to partially de-spin fast rotating asteroids by 25% of the rotational rate within half an orbital period of 2017 PDC.

3.3 Discussion

A range of asteroid sizes and spectral types can be successfully deflected and/or de-spun using neutral beam emitting spacecraft. For an asteroid on the orbit of hypothetical asteroid 2017 PDC, the maximum mass that four NBAC spacecraft can deflect by at least 200 km on a 420 day campaign is 3.8×10^9 kg. The uncertainty in density for asteroid spectral types introduces an uncertainty in the size of asteroids able to be deflected. For C-type asteroids, the difference is that of a 78m or a 100m radius asteroid that can be successfully deflected in a 420 day deflection campaign. NBAC, through its multiple spacecraft architecture, is resilient to spacecraft failure during the deflection campaign. The spacecraft are able to adequately deflect a range of asteroids even in the extreme case of two spacecraft failures after 25% of

the active deflection time has elapsed. Neutral beams can also partially or fully de-spin fast and slow rotating asteroid. In doing this, de-spin and deflection can be accomplished for rotating asteroids while only requiring less than 60 kg of propellant per spacecraft. NBAC has the potential to be used for propulsive fine control of an asteroid's rotation state and orbit.

Chapter 4: Design of a Gas Diffusion Neutralizer for an Argon Ion Source

We have shown that neutral beams can be used to deflect a variety of asteroid sizes and spectral types. In this chapter, we will study the design of the gas diffusion neutralizer. First, we will determine the gas density and mass flow rate needed to neutralize argon ions. This is used to determine the effect of neutralization on electric propulsion performance. We then use COMSOL to investigate a variety of designs for the gas diffusion neutralizer. The data garnered from these simulations is used to design a unique self-contained gas diffusion neutralizer for a neutral beam technology demonstrator.

4.1 One Dimensional Model for Neutralization and Neutral Beam Performance

This section will outline the propulsive performance of a neutral beam that uses a secondary gas flow to globally neutralize the ion flow. Gas diffusion neutralization of an ion beam requires that there is a sufficient background gas density to facilitate the electron recombination reactions required to neutralize the ion beam. Unlike

other electric propulsion systems, a neutral beam requires two separate flow rates: one to create the ions and one to neutralize the ions. In order to maintain a favorable specific impulse, the neutralization fraction for a given flow rate must be maximized. Considering the particles in the flow as either neutral or singularly ionized, Menon [15] provides an analytical solution to the expected neutralization, η_n, (ratio of neutrals to ions) of the atoms after reactions have ceased:

$$\eta_n = \frac{\Gamma_0}{\Gamma_1} = \frac{C_{10}}{C_{10} + C_{01}}(1 - e^{-nL(C_{10}+C_{01})}) \tag{4.1}$$

Where Γ_0 is the flux of neutrals, Γ_1 is the flux of ions, n is the number density of the background gas in the neutralizer, and L is the length of the neutralizer. The reaction cross sections, C_{01} (ionization) & C_{10} (recombination), are dependent on the particle energy (E). Using data from Phelps [17] for beam energies up to 10 keV, we get the empirical relations:

$$C_{01} = 0.6432\ln(E) - 2.4453 \qquad [10^{-16}cm^2] \tag{4.2}$$

$$C_{10} = -4.819\ln(E) + 59.674 \qquad [10^{-16}cm^2] \tag{4.3}$$

Substituting Eqns. 4.2 and 4.3 into Eqn. 4.1 enables the calculation of the neutralization achieved for a range of gas number densities and argon ion energies (see Fig. 4.1). The neutralization chamber number densities shown in Fig. 4.1 drive the required mass flow rate into the neutralization chamber, since this chamber is exposed (on one side) to vacuum. For the range of ion beam energies considered, Fig. 4.1 shows that the gas number density in the neutralization chamber must be on the order of 10^{20} m^{-3} (10^{14} cm^{-3}) in order to maximize argon neutralization.

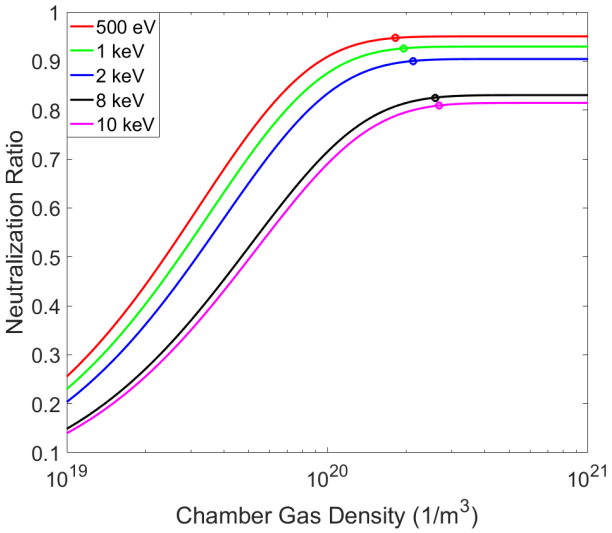

Figure 4.1: Neutralization of an argon ion beam is achieved through reactions with argon gas. The neutralization ratio approaches an asymptote that varies with the energy of the ion beam. The markers denote the point beyond which increasing the background gas density does not significantly increase the neutralization.

The neutralization in Eqn. 4.1 asymptotically approaches a maximum for a given energy as shown in Fig. 4.1. By holding the energy constant and calculating the derivative of neutralization with respect to density we can find the neutralization chamber density where the change in neutralization is less than 0.01%. We plot these points on Fig. 4.1. Increasing the neutralization chamber gas density beyond these values does not appreciably increase the neutralization of the beam. We determine an empirical power law relation for the required linear number density to maximize ion neutralization using the points from Fig. 4.1:

$$nL = 8 \cdot 10^{14} E^{0.1315} \qquad [cm^{-2}] \tag{4.4}$$

Considering a tube of radius r, length L, and the Knudsen number, K_n, we can

calculate the mass flow required in the tube for a desired background density [74]:

$$K_n = \frac{1}{\sqrt{2}\pi D_{HS}^2 nr} \tag{4.5}$$

$$\dot{m}_n = \frac{-\pi r^4 (n k_B T)^2}{1.6\mu_0 RTL} (1 + \alpha K_n) \left(1 + \frac{4K_n}{1 + K_n}\right) \tag{4.6}$$

Where D_{HS} is the hard sphere diameter of argon, μ_0 is the viscocity, R is the specific gas constant, T is the temperature, and α is a parameter for the rarefaction coefficient ($\alpha = 1.358$ for pipe flow). Eqn. 4.6 from [74] considers the viscosity of the fluid and slip in the molecular flow regime. We further assume that there is always a sufficient density of cold electrons, so that the neutralization of the beam is not time varying.

Fundamentally, thrust is produced by mass being ejected at some velocity and can be represented by:

$$F_T = \dot{M} u_e \tag{4.7}$$

Where F_T is the thrust, $\dot{M}$ is a mass flow leaving the thruster, and u_e is the exit velocity of that flow. Electrostatic acceleration relies on the principle that a charged particle is accelerated by an electric potential difference. From an energy standpoint, this is described by:

$$\frac{1}{2} M u_e^2 = eV \tag{4.8}$$

Where M is the mass of the ion, e is the elementary charge, and V is the electric potential difference that the ion experiences. Solving for u_e:

$$u_e = \sqrt{\frac{2eV}{M}} \tag{4.9}$$

The mass flow rate $\dot{M}$ can be expressed in terms of the ion current, I:

$$\dot{M} = \frac{IM}{e} \tag{4.10}$$

Thrust (Eq. 4.7) can be expressed by:

$$F_T = \sqrt{\frac{2eV}{M}} \frac{IM}{e} \tag{4.11}$$

Specific impulse is commonly regarded as the fuel efficiency standard for rocket propulsion and is the total impulse per weight of propellant. For the weight of propellant initially equal to the thrust of the rocket, specific impulse indicates the time it would take for the propellant to be exhausted. It is expressed as:

$$I_{sp} = \frac{F_T}{g\dot{M}} \tag{4.12}$$

Where g is the acceleration of Earth's gravity. Electric propulsion takes advantage of increasing the exhaust velocity of a low flow rate in order to increase the specific impulse. The specific impulse of past and current medium power DC gridded electric thrusters has been between 2000 - 4000s [75].

Finally another key parameter in electric propulsion performance is the mass utilization efficiency, η_n:

$$\eta_u = \frac{IM}{e\dot{M}} \tag{4.13}$$

This indicates the fraction of particles that are ionized, accelerated, and contribute to the thrust.

Using Eqns. 4.1 & 4.6, the basic equations for electric propulsion can be modified to account for changes in performance due to neutralization and the neutralizer mass flow rate:

$$F_T = \eta_n \sqrt{\frac{2eV}{M}} \frac{IM}{e} \tag{4.14}$$

$$I_{sp} = \frac{F_T}{g_0 \left(\dot{m}_b + \dot{m}_n\right)} \tag{4.15}$$

$$\dot{m}_b = \frac{IM}{e\nu_I} \tag{4.16}$$

$$\eta_u = \frac{IM}{e \left(\dot{m}_b + \dot{m}_n\right)} \tag{4.17}$$

Where $\dot{m}_b$ is the mass flow to create the ion beam, $\dot{m}_n$ is the mass flow to neutralize the ions, and ν_I is the ionization and extraction efficiency. Thrust (Eqn. 4.14) now includes the neutralization achievable for a specific ion energy. Specific impulse (Eqn. 4.15) and mass utilization efficiency (Eqn. 4.17) include the flow rate for ion generation and the flow rate required to maximize neutralization as a function of beam energy. The definition of mass utilization efficiency for neutral beam propulsion indicates the fraction of particles that are ionized, accelerated, neutralized, and contribute to the thrust. The flow rate for ion beam generation (Eqn. 4.16) is dependent on the ionization and grid extraction efficiency ν_I, which we take to be 0.9.

An additional consideration when designing an electric propulsion system is the power required to operate the system. Using the power efficiencies as compiled by Petro and Sedwick [75] for similar power systems, the required power of the

neutral beam deflection system can be calculated. Additionally, using the power to mass ratio for UltraFlex [76] (150 W/kg), the mass of the solar panels required can be calculated for a beam operating between 500 mA to 1000 mA (shown in Table 4.1). The mass and power requirements to operate such a propulsion system are both within current technological capabilities.

Table 4.1: Required Power for a Neutral Beam

Neutral Beam Energy (keV)	Power Required (kW)	Solar Panel Mass (kg)
2	2.5-3.85	17-26
8	6.15-10.13	41-68
10	6.94-12.66	46-84

Using Eqn. 4.14, we calculate the thrust as a function of ion energy and current. Thrust has been modified to account for neutralization and we assume that the spacecraft can supply a beam current up to 1000 mA. In Fig. 4.2, the thrust of the neutral beam is plotted as a function of ion beam energy and current. The maximum thrust levels, given the power restrictions, is 74 mN for a 10 keV neutral argon beam.

As mentioned previously, there will be no dust lofting due to neutral beam impingement, however, material may be sputtered from the surface. Using Transport of Ions in Matter (TRIM) [77], a Monte Carlo simulation software that models the interaction of energetic atoms or molecules with targets, we model energetic argon impingement on a flat plate of silicon dioxide with a density of 2 g/cc (an analog to the surface of type-C asteroids [68]). Tens of thousands of atoms with the prescribed

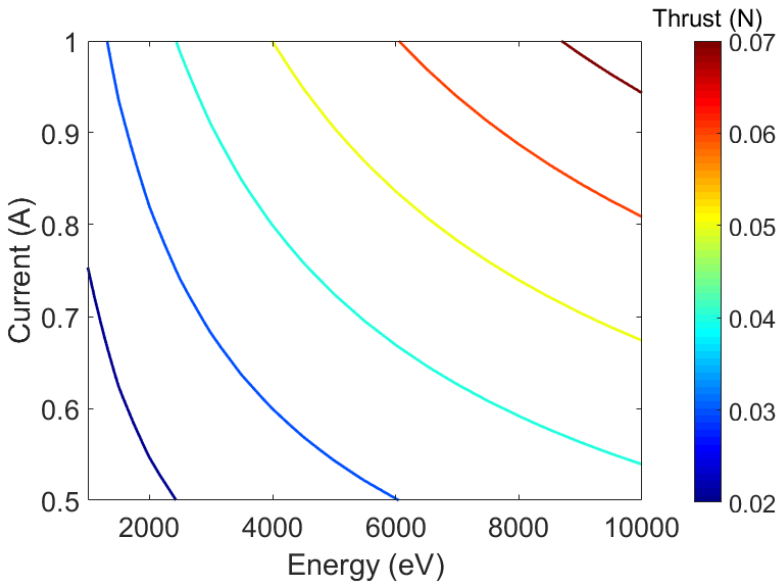

Figure 4.2: Thrust as a function of energy and current of the argon ion source, limited by a maximum beam current of 1000mA and assuming the maximum neutralization fraction for a given energy.

energy are directed at the plate. The number and species of sputtered molecules are recorded and their momentum relative to the beam is included as a thrust enhancement. Fig. 4.3 shows the thrust enhancement due to surface sputtering, considering an argon beam energy of 2 - 10 keV. Thrust enhancement is mildly dependent on incident angle (measured from the plane orthogonal to the surface) and is minimal over this energy range.

For the purposes of the neutral beam, there are two gas flow rates to account for when calculating mass utilization efficiency (i.e. the ratio of the thrust exhaust mass flow rate to the flow rate of argon to the system). Assuming that the mass utilization of the ion beam (ν_I) is 90%, we can calculate the mass flow rate to the ion source that is needed to create a specific plasma current (Eqn. 4.16). Given

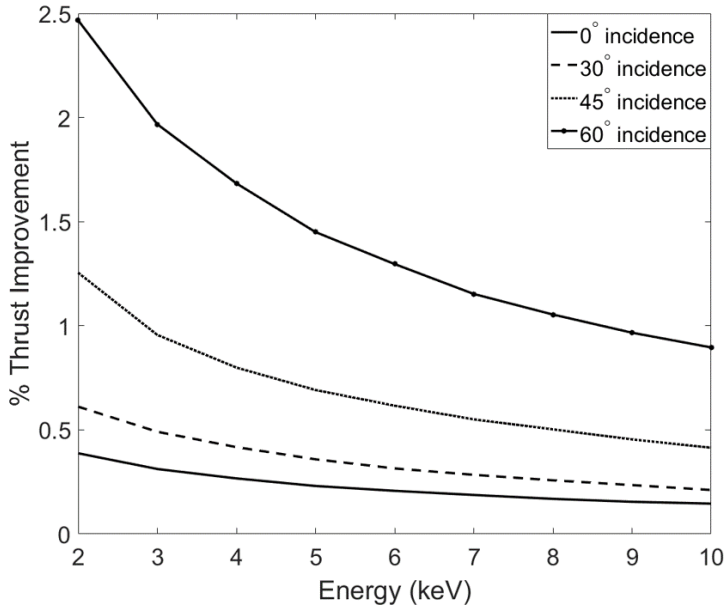

Figure 4.3: Thrust is enhanced by material sputtering from the surface due to the neutral beam impingement. Enhancement is mildly dependent on beam incidence angle and is minimal for this energy range.

a beam energy and assuming a 100 cm long neutralization chamber (chosen to reduce the secondary flow for neutralization), we can calculate the gas flow rate needed to maximize neutralization from Eqn. 4.6. Given the mass flow rates for ion generation and neutralization and the beam energy, we can calculate the mass utilization efficiency (Eqn. 4.17) for the neutral beam (see Fig. 4.4). These utilization values range from 81 - 87% for an open ended neutralizer, considering a 1D model.

Having two flow rates (the ion generation and neutralization flows) also affects the theoretical maximum specific impulse (Eqn. 4.15) for the neutral beam, as plotted in Fig. 4.5.

The mass flow utilization for the low-current, 10 keV thruster and the specific impulse are both high and within the range of ion propulsion [75]. Long term

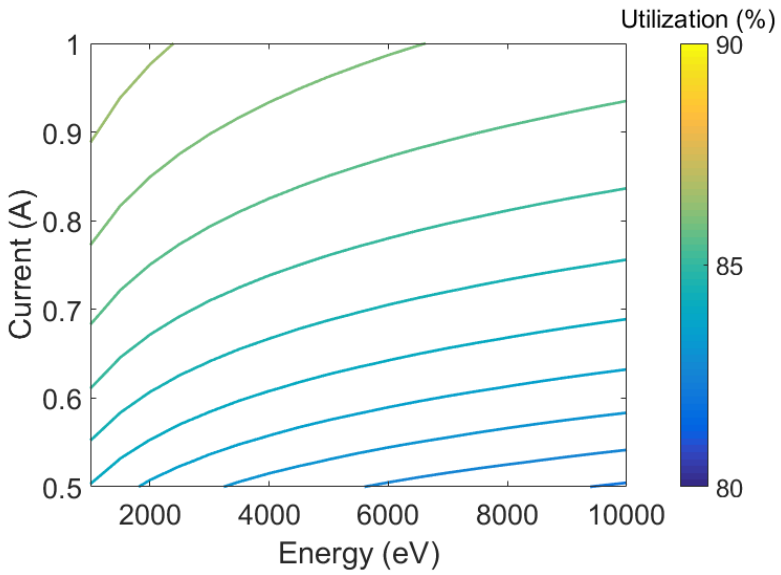

Figure 4.4: Utilization of the argon propellant for a 100 cm open diffuser design over the range of energies and currents. The mass flow utilization for the neutral beam ranges from 81 - 87%.

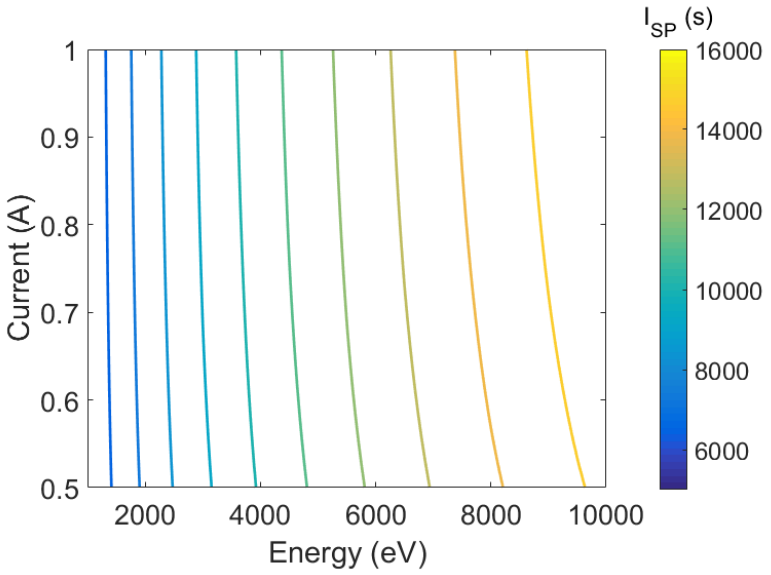

Figure 4.5: Specific impulse of the neutral beam using a 100 cm open diffuser design over a range of ion energies and currents. Specific impulse ranges from 5500- 15700s.

operation is feasible from a propellant mass standpoint and the advantage of ion acceleration techniques for creating efficient space thrusters is maintained making this the baseline energy for the in-space thruster. While the analytical relationships given here provide an initial estimate for the feasibility of neutral beam technology for space applications and the effects of varying beam designs, we are limited in the geometry of the neutralization chamber that can be analytically modeled. To improve the design of a gas diffusion neutralization chamber, COMSOL is employed to investigate the effect of geometry on the the gas flow rates and resulting neutralization of an argon beam.

4.2 Effect of Gas Injection Rate and Neutralizer Geometry

In the previous section, the 1D model demonstrated the relationship between ion energy, neutralization, and the required background gas density. The flow rate of argon gas required for neutralization is highly dependent on the neutralization chamber geometry. COMSOL is used to design a neutralization chamber for a neutral beam technology demonstration that utilizes a 1 keV argon ion source. This COMSOL model assumes low flow rates ($\sim$ 1-10 sccm), low linear densities ($\sim 10^{15} - 10^{16}$ cm^{-2}), and low Knudsen numbers (<10 - 50) and investigates how gas injection and diffuser geometry can be manipulated to realize high neutralization efficiency. Fig. 4.7 shows four geometries modeled in COMSOL that are used to investigate the effect of diffuser length, drift zone length, and injection flow resistance on background gas number density and, ultimately, neutralization.

Fig. 4.6 outlines the geometry choices. The injection zone is the region in which the neutral gas is injected into the system. The drift region is the region between the injection zone and the exit of the neutralizer. For some geometries, a screen is included in the injection zone to increase the local gas density, thereby increasing the neutralization for a given mass flow rate. Fig. 4.7 shows the four geometries modeled in COMSOL. For those geometries with a drift zone, the length of the drift zone is 10 cm, doubling the total overall length of the geometry. In addition to testing different physical geometries, the length of the gas injection zone will also be varied while keeping the total flow rate constant. The screen geometry is 50% porous to create a higher pressure zone in the injection zone by impeding the injected flow.

For all gas flow studies, the free molecular flow module from COMSOL is utilized to determine the background density of argon gas in the system. The boundary of the control volume is kept at vacuum. Once the background density in the chamber has been calculated for a range of flow rates, 1 keV argon ions are injected into the chamber. For ionization and recombination reactions, the reaction cross sections from [17] are utilized in the charge exchange reactions handled by the charged particle tracing module from COMSOL using resonant charge exchange reactions. The argon ions are considered to be monoenergetic and travel with an initial axial velocity. The simulation runs until the energetic particles strike the boundary of the control volume where their charge state is recorded. The size of the control volume is chosen such that its length is large enough to allow the outflowing gas from the neutralization chamber to expand to vacuum. Additionally, the mesh

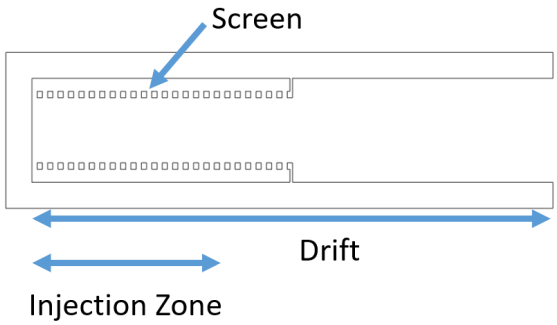

Figure 4.6: The neutralization chamber geometry can consist of an injection zone, drift length, and screen. The injection zone is the length at which an annular flow of gas is introduced; the drift zone has no gas flow introduced and supplements the injection zone as an area for reactions to occur; the screen provides a resistance in the incoming flow from the injection zone.

grid is set to a fine element size with a minimum element length of 0.5 cm and maximum of 4 cm as it was found that there was a loss in convergence for coarser element sizes.

We study the effect of the injection zone length, drift length, and introduction of a screen on the background gas density and sweep through a range of total flow rates from 1 - 10 sccm. Fig. 4.8 presents the neutralization achieved for an injection of 1 keV argon ions into a gas diffusion neutralization chamber with a 1 cm injection zone over the four geometries shown in Fig. 4.7. The neutralization achieved corresponding to the geometry in Fig. 4.7d is maximized for the lowest injection zone flow rate (4 sccm) of the four geometries investigated. In Fig. 4.9, the gas densities in the four geometries for an inflow of 4 sccm are given. Recall from Fig. 4.1, that for 1 keV argon ions, we need densities in the 10^{14} cm^{-3} range to maximize the neutralization ratio. Increasing the neutralizer length by itself has a positive effect

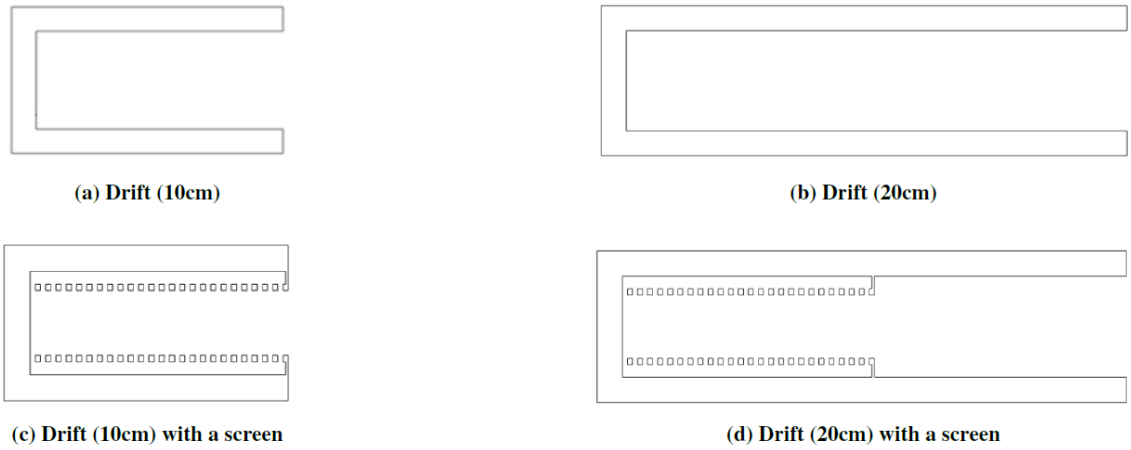

Figure 4.7: Four variations on an open ended gas diffusion neutralizer chamber are modeled in COMSOL to assess the effect of the total length of the neutralizer and flow resistance at the inflow to the background gas density.

on increasing the gas density as the head loss to vacuum decreases. Additionally, increasing the flow resistance via the screen likewise increases the gas density. Together, these two design choices will increase the gas density in the neutralizer for a given flow rate, showing consistency in results between Figs. 4.8 & 4.9.

In Fig. 4.10, we present the gas density of cold argon as a function of the axial position for each of the considered neutralization chamber geometries for a neutralizer flow of 4 sccm. For small injection zones (0.1 & 1 cm), the rate of pressure loss per unit length is constant in the injection zone and drift tube for the designs with and without a screen. However, there are distinct differences in larger injection zones (5 & 10 cm). The injection zone is a greater proportion of the total neutralizer length and a small plateau in gas density is present at the beginning of the neutralizer.

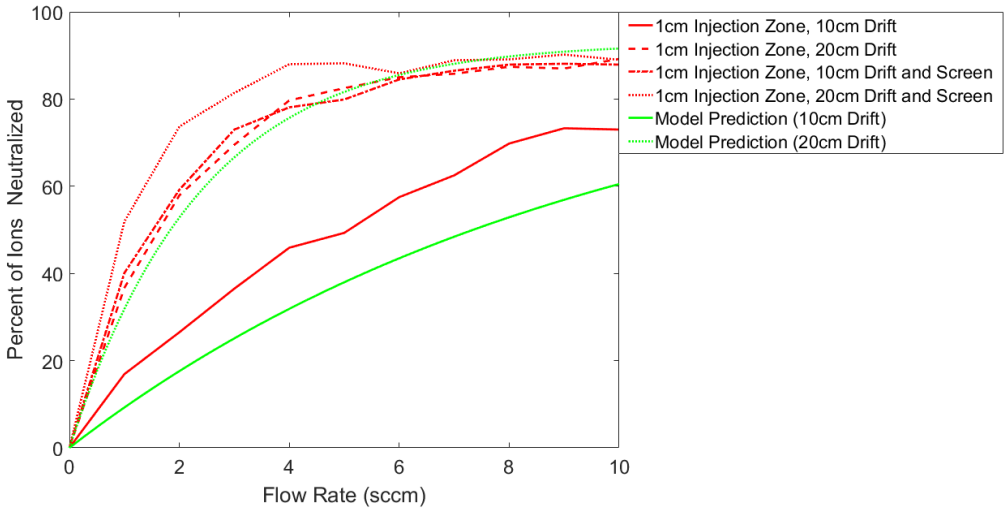

Figure 4.8: Achieving the maximum neutralization for a particular injection zone gas flow rate is dependent upon the geometry of the gas diffusion neutralization chamber. For a flow rate of 4 sccm, the 1 cm injection zone with a 20 cm drift and screen (see Fig. 4.7d) achieved the highest neutralization for the lowest flow rate.

Fig. 4.11 shows the resulting neutralization for the different geometries considered as a function of injection zone length. The addition of the drift zone and the screen both increase the maximum gas density as previously discussed. The addition of a drift region provides a longer reaction region with gas densities suitable for continued recombination reactions. The average density for the 0.1 cm injection zone design increases by a factor of 3.00 with the addition of a screen and drift region. The addition of a screen alone increases the average density by a factor of 2.59. Adding a drift region or a screen have comparable increases in the final neutrality while the addition of both always maximizes the neutralization. While there is an effect on the average density, the injection zone length does not cause a significant overall increase in the final neutralization.

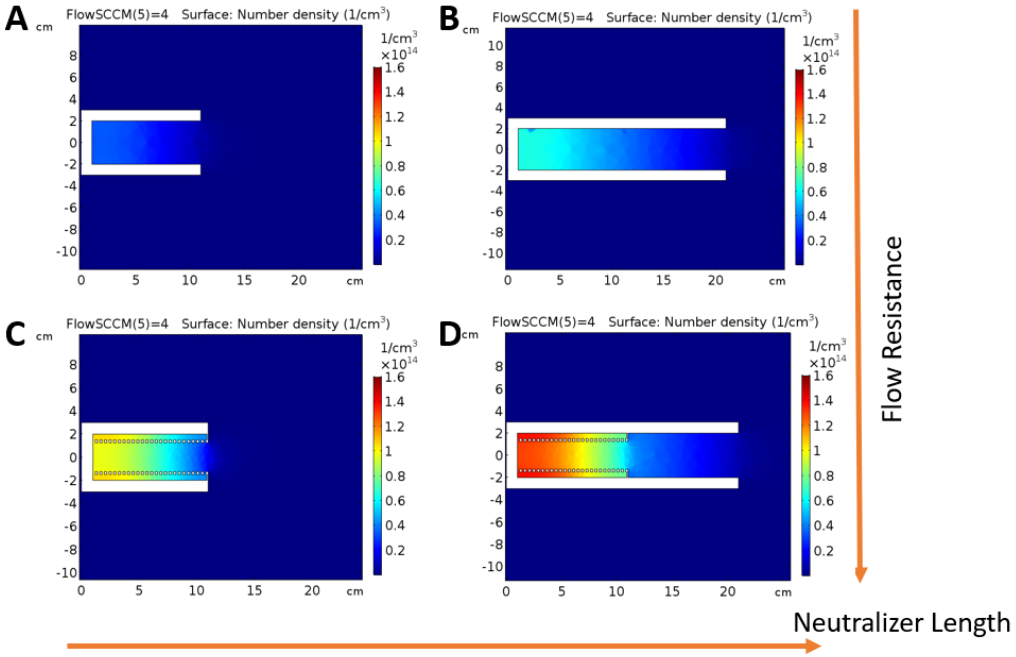

Figure 4.9: Density profiles (flow rate of 4 sccm, injection zone of 1 cm) for: A. a diffuser B. a diffuser with a drift region C. a diffuser with a screen and D. a diffuser with a screen and drift region. Increasing the neutralization chamber length and including a screen increase the argon density and the resulting neutralization of the beam.

The greatest neutralization in the open-ended geometry was achieved by adding a drift region and a screen to provide flow resistance in the injection zone. In order to reduce the gas loss rate, we can partially close the neutralization chamber end so that the high energy particles can pass through and the gas flow rate out is reduced (Fig. 4.12). We consider a geometry where the opening is half the radius of the neutralization chamber. The goal is to increase the total utilization efficiency for the gas in the thruster by reducing the gas flow rate out of the neutralizer.

In Fig. 4.13, we present a comparison of the axial gas density profiles for a range of injection zone lengths for the open and partially open geometries, considering a

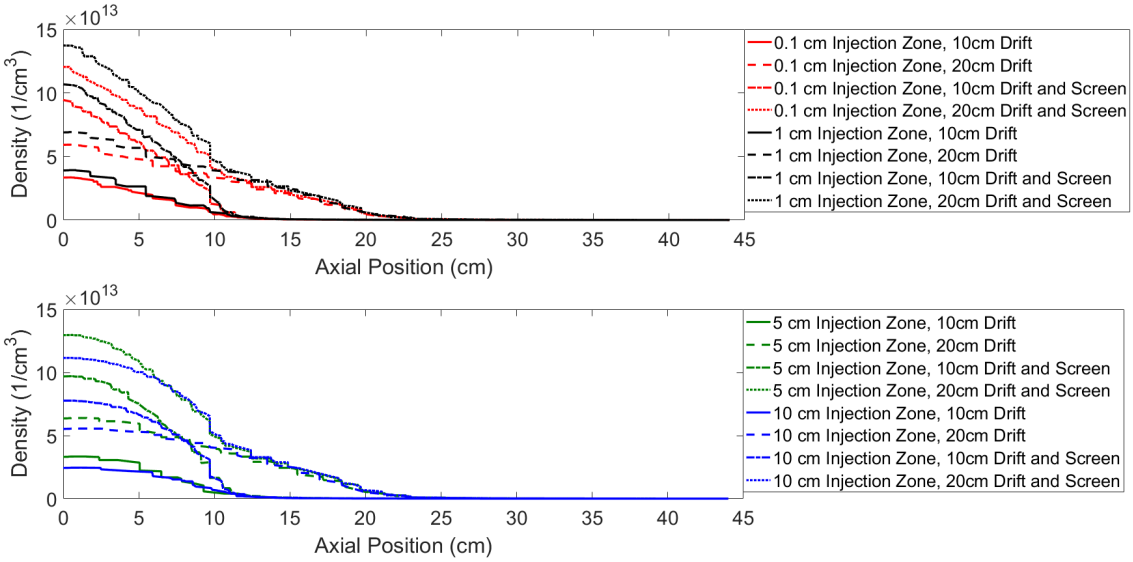

Figure 4.10: The gas density profiles for a flow rate of 4 sccm are given. Gas density loss per unit length is generally the same rate for each of the design options with different injection zone lengths. An increase in average density is seen in geometries that include an annular screen.

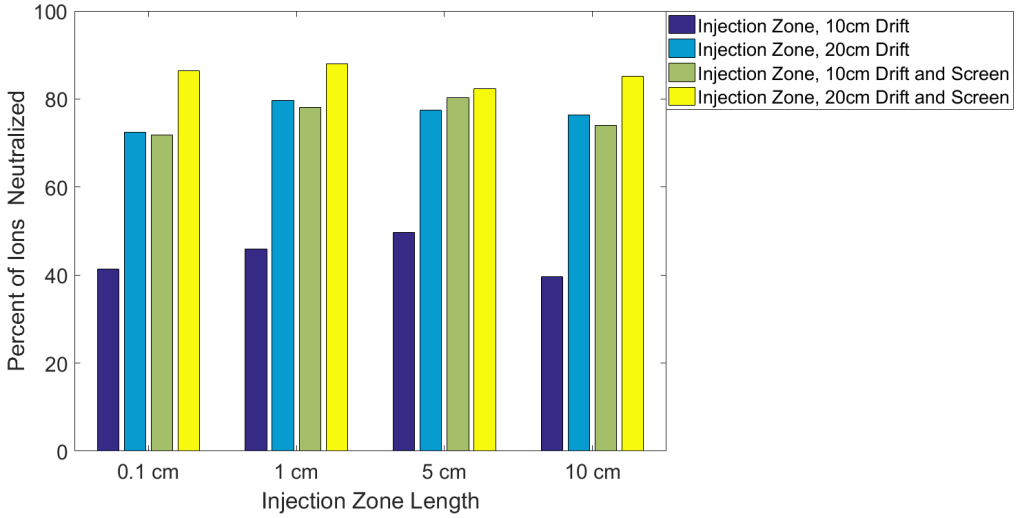

Figure 4.11: The percent of ions neutralized for a 4 sccm neutralizer flow rate and the scope of geometry choices is given. Neutralization increases with the addition of a drift region and a screen.

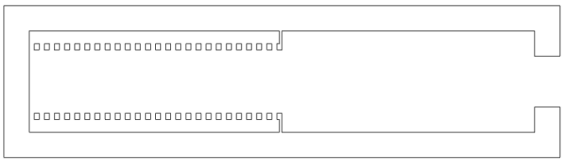

Figure 4.12: Geometry of the partially open neutralization chamber with screen and drift zone. With a partially open end, the high energy atoms can pass through and the gas is partially restricted from escaping.

gas injection rate of 4 sccm; this is the same gas flow rate shown in Fig. 4.10. As expected, the background gas density in the neutralization chamber increases for a partially open geometry. The rate of axial variation of the density is similar between open and partially open geometries up to the exit/vacuum interface where the gas density of the partially open geometry drops precipitously. The longer injection zone lengths (5 & 10 cm) both have a small gas density plateau in the injection zone before subsequently decreasing.

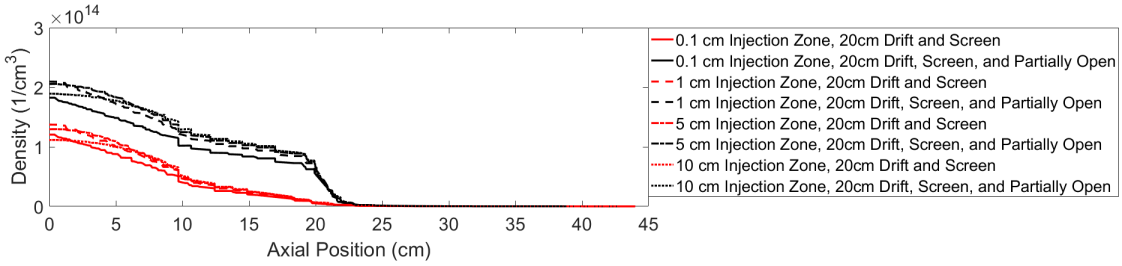

Figure 4.13: Gas Density for a 4 sccm flow rate for the partially open and open geometries using a range of injection zone lengths.

Repeating the simulations and methods for the same range of gas flow rates, we compare the neutralization of the beam between the partially open geometries and the open geometries in Fig. 4.14. Fig. 4.14 shows that neutralization generally

increases with increasing flow rates. The neutralization for partially open geometries for low flow rates is higher than that of the open ended geometries. The length of the injection zone has a minor impact on the total neutralization. The partially open geometry achieves a maximum neutralization of 89% for 3 sccm of flow where 6 sccm of flow is required to achieve maximum neutralization in the open design.

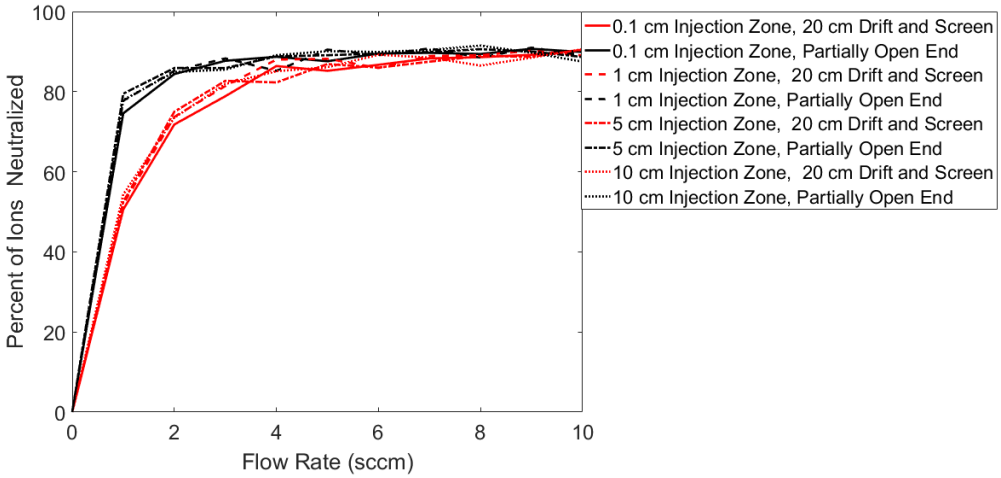

Figure 4.14: Predicted neutralization for open and partially open 20cm drift and screen (Figs. 4.7d & 4.12) geometries for flow rates of 1-10 sccm. The addition of the partially open end increases the neutralization achieved at lower flow rates.

Based on these investigations, a technology demonstration of neutral beam technology with a 1 keV ion source should use a flow rate of 4 sccm. The neutralizer should utilize a partially open geometry with a 20 cm drift region and screen to provide a high neutralization for a low gas flow rate. For a spacecraft equipped with a neutral beam, the fundamental geometry choices would remain the same. We would require a 10 keV ion source to meet thrust requirements for asteroid deflection which would change the achievable neutralization and the neutralizer flow rate.

4.3 Discussion

The additional gas flow needed to create the optimal background density for neutralization of an ion beam does not eliminate the efficiency advantage that electric propulsion has over other space propulsion. Both the specific impulse and mass utilization efficiency decrease from the ideal but have acceptable efficiencies for long-term operation. Investigating the effect of geometry on gas diffusion neutralizer performance in COMSOL, we have demonstrated that a partially open, long diffuser with an annular diffusion screen can provide high global neutralization of an ion beam for low gas inflow rates. The partially open end of the neutralizer limits the outflow of injected gas, increasing the utilization of this gas for recombination reactions. Using a longer neutralizer, not only increases the background gas density but it also increases the time that the ions can undergo recombination reactions. The annular screen also increases the average background gas density. This unique, self-contained gas diffusion neutralizer enables the application of a neutral beam for electric propulsion.

4.4 Final Design of the Gas Diffusion Neutralizer

The gas diffusion neutralizer for the neutral beam technology demonstrator comprises of three elements: the screen, the structure, and the end caps. It is 20 cm long consisting of two parts: a 10 cm screened region and a 10 cm drift region. Fig. 4.15 presents the drawing for the gas diffusion screen. A small hole patter is

drilled into a long aluminum ring with the lines of holes being separated by 12° from one another.

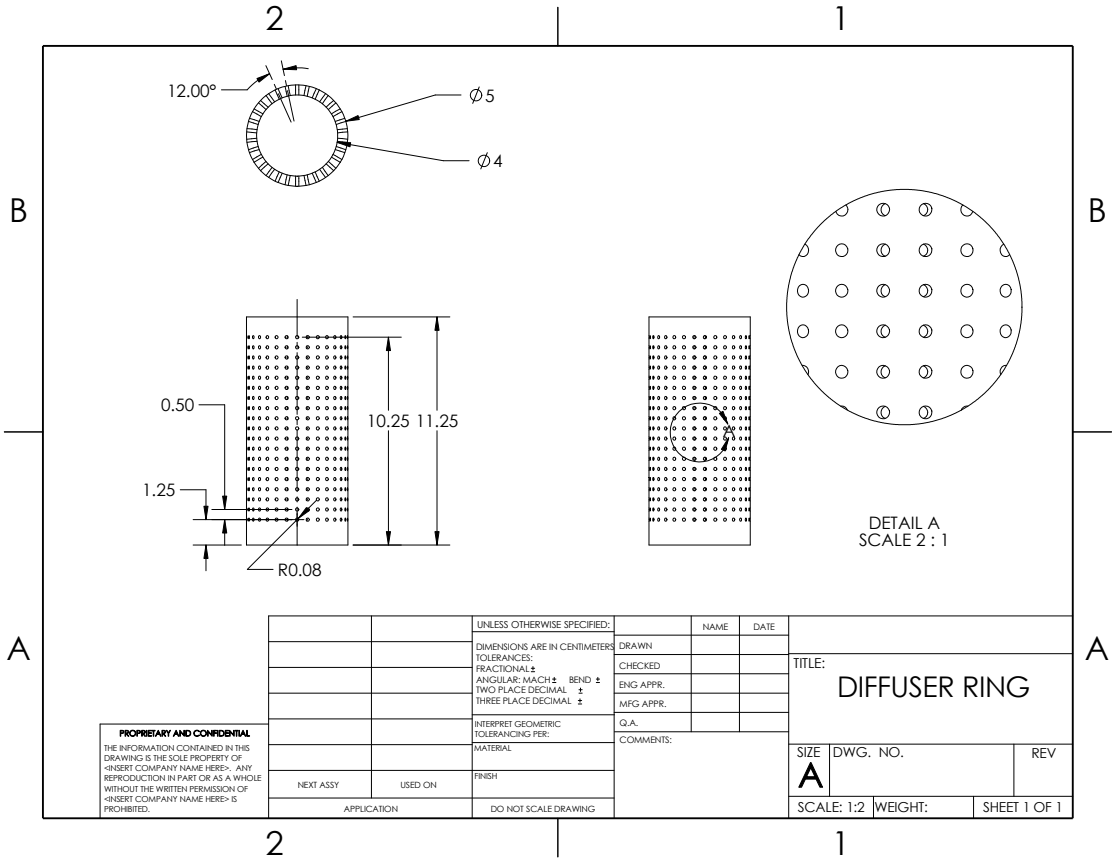

Figure 4.15: The gas diffuser screen has a small hole pattern to create a diffusive boundary between the gas input ports and the center of the gas diffusion neutralizer.

The gas diffusion screen is inserted into the structure (shown in Fig. 4.16) on the side with the eight holes drilled around the exterior. The holes on the structure exterior are for the eight barbed connectors that connect the gas lines to the gas diffusion neutralizer. They are separated by 45° from one another and provide an azimuthally symmetric gas flow to the neutralizer. Two end caps (Fig. 4.17) are

affixed the the structure using M2 screws. The 2 cm opening allows for the ion beam to pass through the gas diffusion neutralizer but prevents some injected gas from escaping. An exploded view of the gas diffusion neutralizer assembly is given in Fig. 4.18.

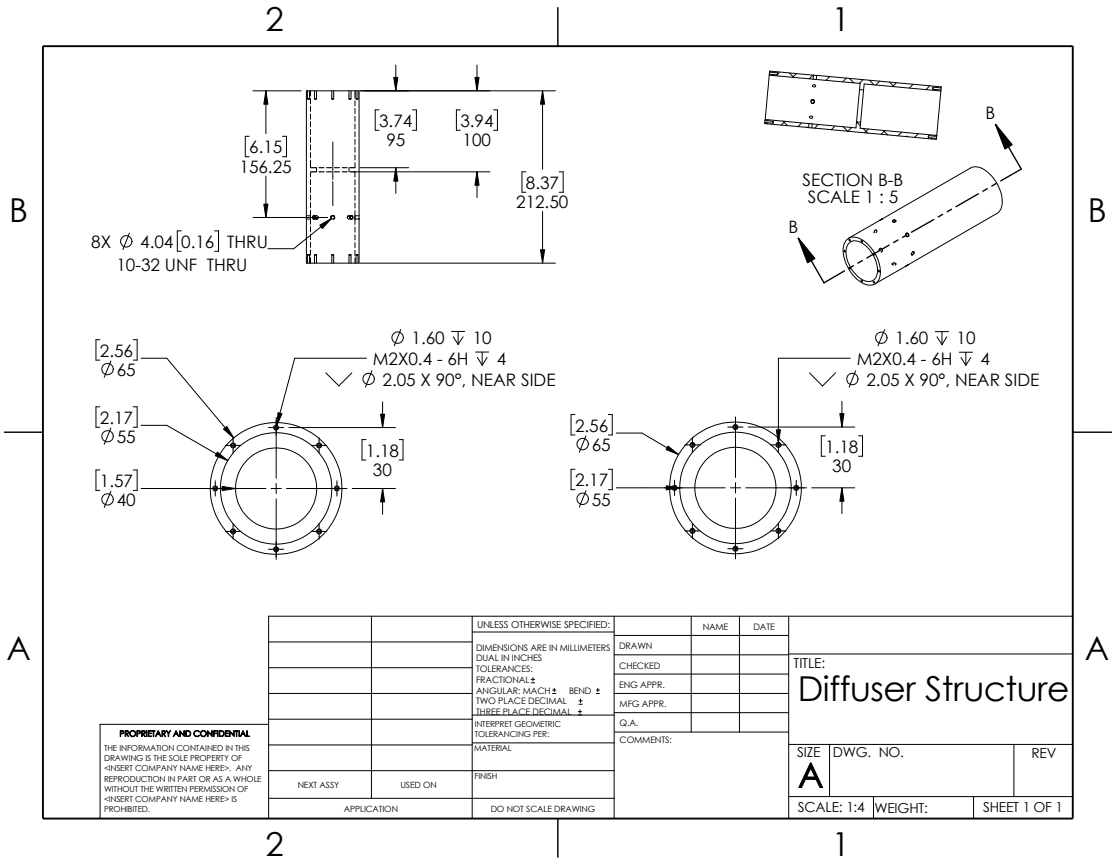

Figure 4.16: The gas diffusion neutralizer structure houses the gas diffuser screen and has eight holes on the exterior for the barbed fittings that connect the gas lines.

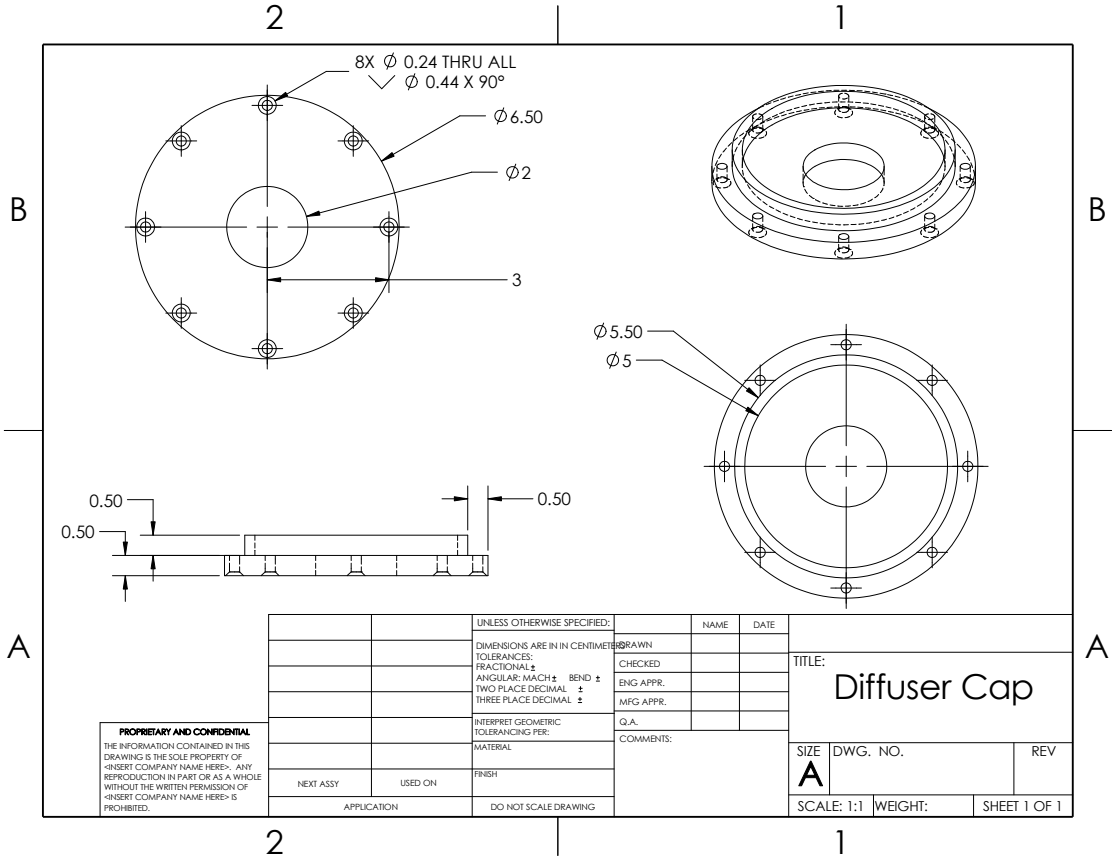

Figure 4.17: The neutralizer caps allow for the ion beam to pass through and prevent some of the injected gas from escaping.

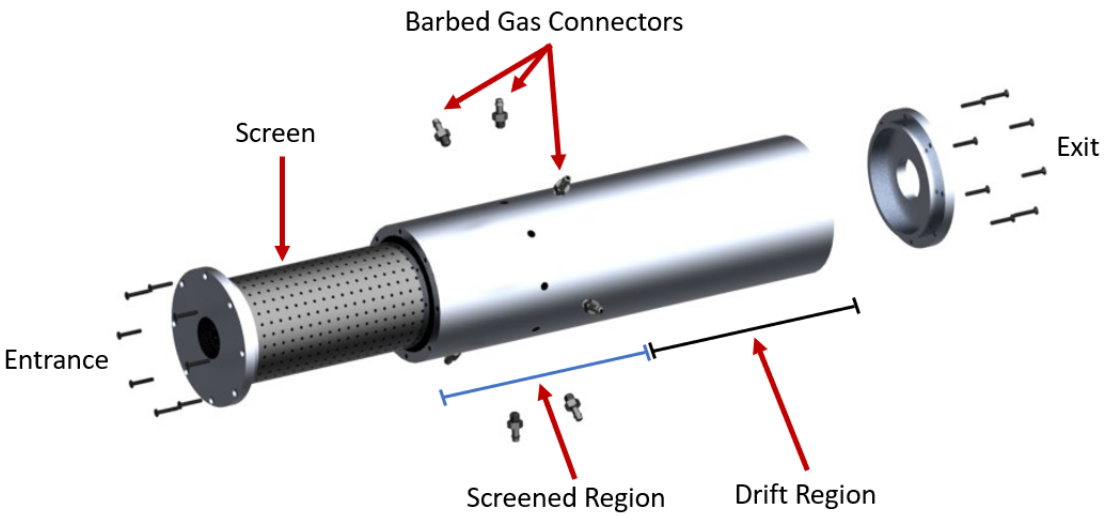

Figure 4.18: Exploded view of the gas diffusion neutralizer. The neutralizer consists of eight barbed gas connectors that are equally separated azimuthally about the neutralizer. A screen is inserted into the neutralizer to create a constant background density in the screened region.

Chapter 5: Testing Methodology for a Neutral Beam Technology Demonstration

The work in Chapter 4 developing the gas diffusion neutralizer design will be directly applied to a neutral beam technology demonstrator. This chapter will cover the procedures for building the diagnostics and testing at the NASA MSFC and UMD facilities. Through these tests, we will characterize the performance of a neutral beam technology demonstrator by measuring its thrust and neutralization.

5.1 Procedure for the preparation of the VAHPER thrust stand and vacuum chamber for thrust testing

Thrust measurements were performed using the hanging-pendulum VAHPER thrust stand of Polzin *et al.* [59] at Marshall Spaceflight Center. The VAHPER thrust stand is enclosed in a 9 ft diameter, 25 ft long vacuum chamber capable of maintaining a pressure of 10^{-6} torr using two 2400 L/s turbopumps during testing of the neutral beam. The vacuum chamber has multiple feedthroughs for power, gas flow, and visual purposes. Electrical cabling to the thruster was arranged in a waterfall manner to reduce the thrust stand arm deflection that could be caused by

cable heating. The neutral beam was affixed to the VAHPER thrust stand using M6 screws bolted through the frame holding the ion source and neutralizer (as shown in Fig. 5.1).

1) Using a ladder to access the top of the VAHPER thrust stand, verify that the two locking screws for the VAHPER thrust stand are fully tightened before conducting any work.

2) Attach the neutral beam technology demonstration frame with the assembled neutral beam to the VAHPER thrust stand using six M6 screws with their corresponding nuts, positioning the exhaust towards the long end of the chamber.

3) Connect the stainless steel tubing from the ion source to the Swagelok connector on the thrust stand for the tubing connected to mass flow controller #1, utilizing a new two-ferrule set. Tighten 1.5 turns with a 1/4 in. wrench.

4) Connect the plastic tubing from the gas diffusion neutralizer to the corresponding Swagelok connector on the thrust stand for the tubing connected to mass flow controller #2 , utilizing a new two-ferrule set. Tighten 1.5 turns with a 1/4 in. wrench.

5) Separate the two sets of three-wire cables that connect to the ion source and utilize zip ties to affix the wires to the top grate of the vacuum chamber in a repeated looping pattern, known as the "waterfall" method. Continue this pattern to the side 10 in. port of the vacuum chamber.

6) On the 8 in. power feedthrough port, insert the two 1 in. power feedthrough connectors and tighten the 1 in. nut with a wrench to a torqueof 15 ft-lbs. Plug the red and blue connectors from the ion source into the corresponding power feedthrough connector. (See Fig. 5.2)

7) Place the power supply on a table that is vibrationally isolated from the thrust stand and connect the ion source output cables to the power feedthrough port. Connect the power supply input cable to a 240V, 30A plug. Ground the power supply case using a braided cable and verify ground using the Ohmmeter setting on a voltmeter. Turn the power supply on to verify connection to an active power outlet.

8) Remove tools from vacuum chamber and verify that no tool pieces or hardware have fallen through grates.

9) Using a ladder to access the top of the VAHPER thrust stand, loosen the two locking screws, allowing the inverted pendulum to move freely. Remove ladder from vacuum chamber.

10) Close vacuum chamber door by pushing on superstructure to move door along track (shown in Fig. 5.3). Engage locking clamps on the upper left and upper right of the vacuum chamber door using control board. Using two large C-clamps, manually clamp the bottom left and bottom right of the vacuum chamber door.

11) Close the Swagelok air bleed valve on the vacuum chamber and verify that gas

valves to and from the mass flow controllers are open.

12) Verify that all power systems to vacuum chamber control and monitoring are connected and on.

13) Turn on roughing pumps and begin vacuum chamber gas evacuation.

14) Once vacuum chamber pressure has reached 10^{-3} torr, open gate valves to both turbopumps and engage both turbopumps. Tighten C-clamps on vacuum chamber door. Wait at least two hours before proceeding to reduce pressure to 10^{-6} torr and to allow full dampening of the VAHPER thrust stand from any residual mechanical vibrations from the pump-down procedure.

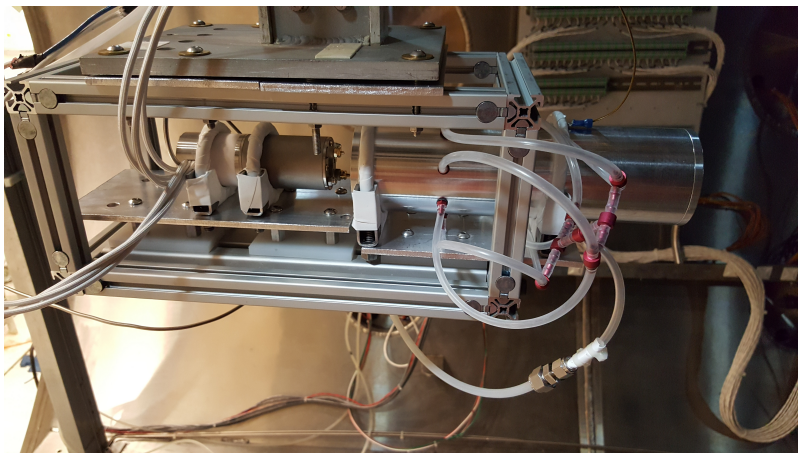

Figure 5.1: The neutral beam technology demonstrator is affixed to the VAHPER thrust stand using M6 screws bolted to the frame.

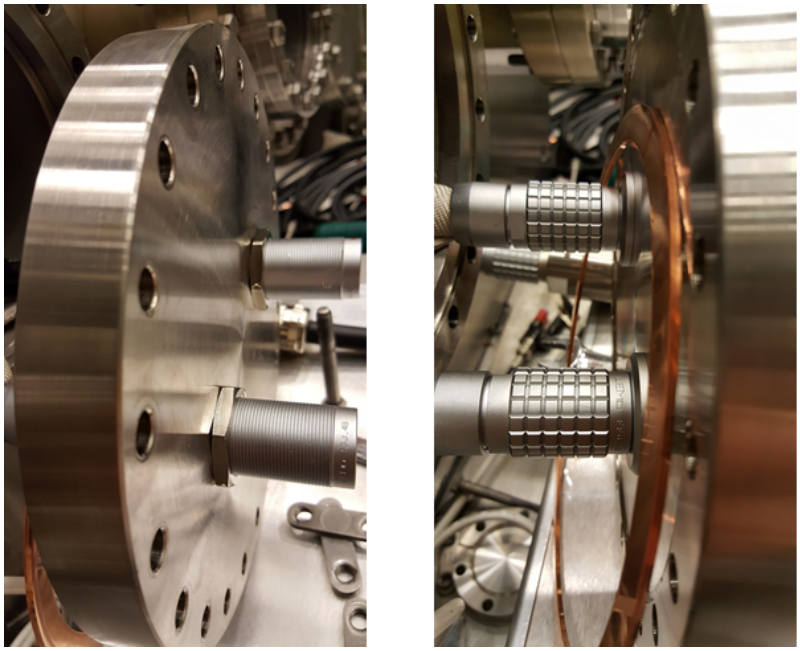

Figure 5.2: 10 in. power feedthrough port for the ion source at NASA Marshall Spaceflight Center. Left: 1 in. nuts tightened to create seal for the power feedthrough. Right: Plug connectors from the ion source plugged into the feedthrough (note the copper gasket used to seal the port).

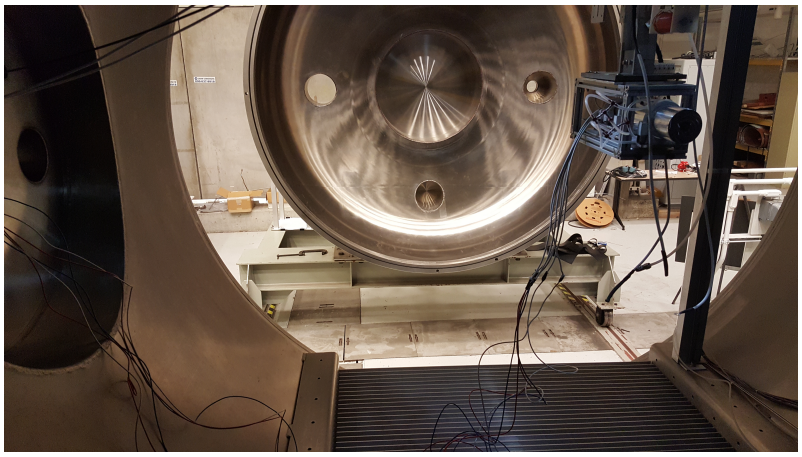

Figure 5.3: The vacuum door for the 9 ft diameter vacuum chamber at NASA Marshall Spaceflight Center is attached to a superstructure that rolls along a track.

5.2 Procedure for the calibration of the VAHPER thrust stand and thrust measurements of the neutral beam technology demonstrator

1) Open data capture LabView vi for the VAHPER thrust stand on the vacuum chamber monitoring desktop.

2) Initialize current to 5 mA for calibration tool and activate piezoelectric motor. If amplitude is larger than 1 mN, reduce output voltage and re-run tool until thrust amplitude is at or near 0.1 mN. If on first activation, thrust amplitude is immeasurable, increase current to 7 mA with a maximum of 10 mA allowable. Create 5-6 calibration points of varying voltage and current with the piezoelectric motor to include thrust magnitudes from 0 - 1 mN.

3) Fully open main argon tank valve and set regulator to 25 psi.

4) Initialize gas flow controller #1 to 4 sccm, begin recording data with LabView vi, and activate gas flow controller #1.

5) Turn on ion source power supply and pre-set the following values using the Setpoint Adjust nob: Discharge Volts: 40 V, Discharge Amps: 0.1 A, Beam Volts: 1000 V, Beam mAmps: 22.8 mA, Accelerator Volts: 150 V, Accelerator mAmps: 1.5 mA.

6) Verify that the thrust stand is damped. Press Discharge enable on ion source power supply. Once Cathode Volts, Cathode Amps, Discharge Volts, and

Discharge Amps have reached steady values proceed to next step.

7) Press Beam Enable button. Once Beam Volts, Beam mAmps, and Accelerator Volts have reach desired values and the values are steady, wait 1 min, then press Beam Enable button again to bring beam to standby mode.

8) Pre-set mass flow controller #2 to 1 sccm and enable. Repeat step 7 for Beam mAmps at 22.8 mA and 30.4 mA for 0 - 10 sccm flow rates for mass flow controller #2 in 1 sccm increasing increments.

9) When trials have finished or in the event of a beam stability or discharge error, power down power supply by flipping main switch. Stop LabView vi and save testing data. Evaluate trouble shooting procedures in ion source power supply manual for beam stability or discharge errors.

10) If trials are finished or maintenance is required set both mass flow controllers to 0 sccm and fully close main argon tank.

11) Turn off turbopumps and wait until both turbopump RPM readouts have reached 0 RPM.

12) Close gate valves and turn off roughing pumps. Open Swagelok air bleed valve to fully open and bring vacuum chamber up to atmospheric pressure.

13) Remove C-clamps on vacuum chamber door and release locking clamps. Push on vacuum door superstructure to move door along rails.

5.3 Construction of a Copper Faraday Cup

Neutralization and thermal power testing were both conducted at the University of Maryland. The vacuum chamber consists of an 18 in. diameter, 28 in. tall bell jar that rests on a 20 in. diameter, 11 in. tall stainless steel base. On the stainless steel base are two ports for gas flow control, one port for power to the ion source, one visual port, and one data feedthrough port. The pumping speed of the turbopump is 290 L/s and is able to maintain a pressure of $4{\cdot}10^{-4}$ - $1{\cdot}10^{-3}$ torr, depending on the neutralizer flow rate. This vacuum pressure is within the operating range for the KDC 10 ion source.

1) Cut a 12.5" x 4" piece of a 1/8" thick sheet of copper. Cut two 3" x 3" squares of a 1/8" thick sheet of copper. Centered in one of the 3" x 3" squares cut a 1.25" x 1.25" rounded square using a mill.

2) Bend the 12.5" x 4" piece of copper using a hammer and vise into a 3" x 3" x 4" open box with rounded edges. Clean all copper pieces with Scotch Brite and water.

3) Using a heat gun, Chipquik SMD291 flux [78], and lead solder, solder the seam of the open 3" x 3" x 4" box and the 3" x 3" squares on either end of the open 3" x 3" x 4" box. It is necessary to pre-heat the copper box as its thermal inertia is high. Ensure that there are no large gaps in the soldered joints. If large gaps exist, twist small stranded copper wire and push into large gaps. Use solder, heat gun, and Chipquik SMD291 flux [78], wick the solder into the

Figure 5.4: Copper Faraday cup made from a 1/8" sheet of copper. It is used for determining the neutralization of the beam.

joints via the small stranded wire.

4) Solder a thin gage wire onto one of the bottom joints and to that wire solder a 100 Ω resistor using a lineman splice [79].

5) Fill box with water and check for leaks. If any exist, re-solder.

6) Clean box on inside and outside using Scotch Brite to clean oxidized layer.

Finished Faraday cup is shown in Fig. 5.4.

5.4 Procedure for the preparation of neutralization measurements via a Faraday cup

1) Raise the bell jar to its maximum height by operating the hand crank.

2) Insert the neutral beam technology demonstration with the Faraday cup vertically into the middle of the vacuum chamber.

3) Connect the stainless steel tubing from the ion source to the Swagelok connector for the tubing connected to mass flow controller #1, utilizing a new two-ferrule set. Tighten 1.5 turns with a 1/4 in. wrench.

4) Connect the plastic tubing from the gas diffusion neutralizer to the corresponding Swagelok connector for the tubing connected to mass flow controller #2 , utilizing a new two-ferrule set. Tighten 1.5 turns with a 1/4 in. wrench.

5) Ground the gas diffusion neutralizer using a 14 gage braided wire that is inserted under the U-clamp and directly touching the neutralizer. Place the other end of the wire under the neutral beam structure such that it is held to the bottom of the chamber. Verify the ground connection using the Ohmmeter setting on a voltmeter.

6) Using an alligator clip, connect the wire from the Faraday cup to the single wire feedthrough. On the air side of the feedthrough, connect a wire to the feedthrough and insert into the NI 9205 on Channel 17. Connect a ground wire into the NI 9205 on Channel 33. Connect a wire on the NI 9205 on

Channel 33 to the COMM terminal.

7) On the 6 in. power feedthrough port, insert the two 1 in. power feedthrough connectors and tighten the 1 in. nut with a wrench to a torque of 10 ft-lbs. Plug the red and blue connectors from the ion source into the corresponding power feedthrough connector.

8) Place the power supply on a table and connect the ion source output cables to the power feedthrough port. Connect the power supply input cable to a 240V, 20A plug. Ground the power supply case using a braided cable and verify ground using the Ohmmeter setting on a voltmeter. Turn the power supply on to verify connection to an active power outlet.

9) Clean the stainless steel/rubber gasket interface where the bell jar rests on the vacuum chamber with isopropyl alcohol, removing all greasy residue.

10) Once the surfaces are clean and dry, apply Apiezon M vacuum grease [80] evenly on the rubber gasket. Lower the bell jar onto the vacuum chamber using the hand crank.

11) Close the Swagelok air bleed valve. Turn the power on for the vacuum pumps, vacuum gage, and mass flow controllers. Verify that the gate valve is closed and that the ball valve is open.

12) Turn on roughing pump and begin vacuum chamber gas evacuation.

13) Once vacuum chamber pressure has reached 10^{-3} torr, open gate valve to the turbopump and engage the turbopump. Once the pressure has reached

10^{-6} torr, the neutral beam technology demonstration is ready for neutralization testing.

Figure 5.5: The neutral beam technology demonstrator integrated with the vacuum chamber at UMD. The ion source is at the top of the frame with the gas diffusion neutralizer directly underneath. The Faraday cup is at the bottom of the image. The clear tubes and the stainless steel tube deliver argon to the system and the white cables deliver power.

5.5 Procedure for neutralization measurements via a Faraday cup

1) Using the USB connector, plug the NI 9205 into a computer. Open the data capture LabView vi for the Faraday cup.

2) On the main page of the vi, press Ctrl+E to access the wire diagram. Double-

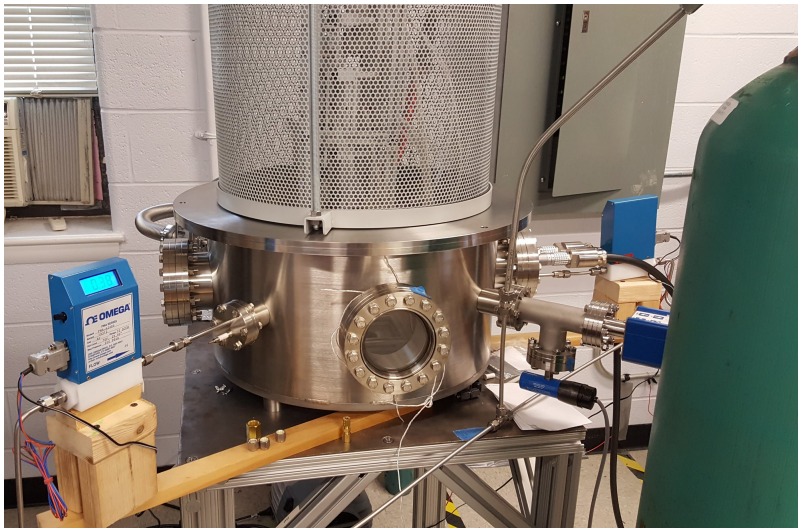

Figure 5.6: The vacuum chamber at UMD with the bell jar seated on the stainless steel portion. The front port is a visual port for pictures and to verify that the ion source is operating nominally. The green tank is the argon gas tank. The blue mass controller is capable of delivering 0 - 10 sccm of mass flow to the system.

click on the DAQ Assistant. Click on the Voltage input channel and set the minimum and maximum expected voltage. For a 100 Ω resistor enter ± 200 mV for the minimum and maximum. For a 1100 Ω resistor, enter ± 2 V for the minimum and maximum. This sets the proper gain for the NI 9205. Save the vi program.

4) Turn the mass flow controller potentiometers completely clockwise. Fully open main argon tank valve and set regulator to 20 psi.

5) To calibrate the controllers, use a small flathead screwdriver and turn the setpoint screw until each mass flow controller reads 0 sccm.

6) Turn on ion source power supply and pre-set the following values using the

Setpoint Adjust nob: Discharge Volts: 40 V, Discharge Amps: 0.1 A, Beam Volts: 1000 V, Beam mAmps: 22.8 mA, Accelerator Volts: 150 V, Accelerator mAmps: 1.5 mA.

7) Slowly turn the potentiometer on mass flow controller #1 to 4 sccm, begin recording data with LabView vi.

8) Press Discharge enable on ion source power supply. Once Cathode Volts, Cathode Amps, Discharge Volts, and Discharge Amps have reached steady values proceed to next step.

9) Press Beam Enable button. Once Beam Volts, Beam mAmps, and Accelerator Volts have reach desired values and the values are steady, wait 30 seconds, then press Beam Enable button again to bring beam to standby mode.

10) Set mass flow controller #2 to 1 sccm and enable. Repeat step 8 for Beam mAmps at 22.8 mA for 0 - 10 sccm flow rates for mass flow controller #2 in 1 sccm increasing increments.

11) When trials have finished or in the event of a beam stability or discharge error, power down power supply by flipping main switch. Stop LabView vi and save testing data. Evaluate trouble shooting procedures in ion source power supply manual for beam stability or discharge errors.

12) If trials are finished or maintenance is required set both mass flow controllers to 0 sccm and fully close main argon tank.

13) Turn off turbopump and wait for green LED light to stop blinking.

14) Close gate valve and turn off roughing pump. Open Swagelok air bleed valve to fully open and bring vacuum chamber up to atmospheric pressure.

15) Lift bell jar using hand crank and conduct maintenance if necessary.

5.6 Construction of a Direct-Contact Graphite Calorimeter

1) Using a tile saw, cut graphite sheet into 1.2 cm x 1.2 cm squares. Use 1000 grit or better sandpaper to meet tolerance of ± 0.08 cm. Let graphite blocks dry completely. Pick nine graphite blocks to be used for the calorimeter based upon best tolerance. Using milligram scale, measure mass of each calorimeter block and record data.

2) Cut T-type thermocouple wire into nine 13 in. segments. Strip 1.5 in. of brown casing from either end of thermocouple wire. On one end of thermocouple wire, strip 0.25 in. of the copper and constantan leads. Dip each lead into Chipquik SMD291 flux [78]. Solder leads together using lead solder and soldering iron. Repeat for all nine wires. On the other end of the thermocouple wire, strip 0.25 in. of the copper and constantan leads.

3) At the soldered end of the thermocouple, bend the wire to a right angle. Mix JB weld according to instructions [81]. Holding the soldered end against the back of the calorimeter block, apply JB Weld so that soldered end is completely covered and is covering the back of the calorimeter block. Using a heat gun on its low setting, heat the JB Weld on the back of the calorimeter block to

partially dry the JB Weld joint. Repeat for all nine calorimeter blocks and let cure for 24 hours.

4) Drill nine holes into a 5.5" wide, 4" long, 1/8" thick Garolite sheet. The holes should be arranged such that a 3 x 3 grid of graphite blocks can be arranged with the blocks touching one another. See Fig. 5.7.

5) Cut a small piece of Kapton tape and wrap the sides and bottom of each calorimeter block.

6) Insert each thermocouple wire into one of the nine drilled holes. In rows of three, match the heights and sides of each calorimeter block and tie together using small stranded wires to prevent slipping. When each row of three is complete, tie two rows together (matching heights and sides once again) and then tie all three rows together to create a 3 x 3 calorimeter block. See Fig. 5.8.

7) Inject Chipquik SMD291 flux [78] into 18 sequential soldering cup pins on a 50 pin, solder cup connector [82]. Dip each un-soldered copper and constantan lead into Chipquik SMD291 flux [78]. Using a soldering iron, melt a small amount of solder to create a bead on the soldering tip. Placing the copper lead in the soldering cup, touch the soldering iron tip at the top of the soldering cup and allow the solder to flow until the circular indicator is full on the soldering cup. Repeat for each copper and constantan lead. See Fig. 5.9.

8) Cut T-type thermocouple wire into nine 12 in. segments. Strip 1.5 in. of brown casing from one side and 8 in. of brown casing from the other side.

Strip 0.25 in of the constantan and copper leads on either side.

9) Cut nine 18 in. segments of 24 gage copper wire, strip 0.25 in. from either side of each wire. On the side where 8 in. of casing was stripped, solder the constantan wire to one end of the 18 in., 24 gage wire using the lineman splice [79]. Repeat for each constantan lead on the side where 8 in. of casing was stripped.

10) Repeat Step 7 on another 50 pin connector [82] for the side where 1.5 in. of casing was stripped taking care to match the copper and constantan leads with corresponding copper and constantan leads between the two 50 pin [82] connectors. Label each wire for which calorimeter block it corresponds to with a return address label.

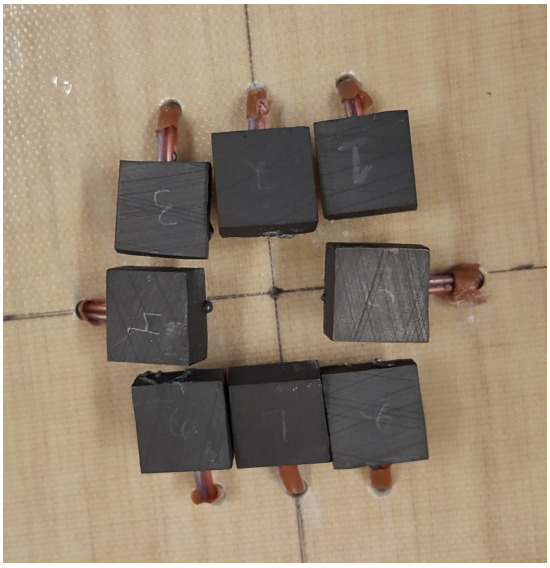

Figure 5.7: Calorimeter blocks with thermocouple wire are inserted into the drilled holes in the Garolite sheet. Shown here are eight of the nine blocks inserted.

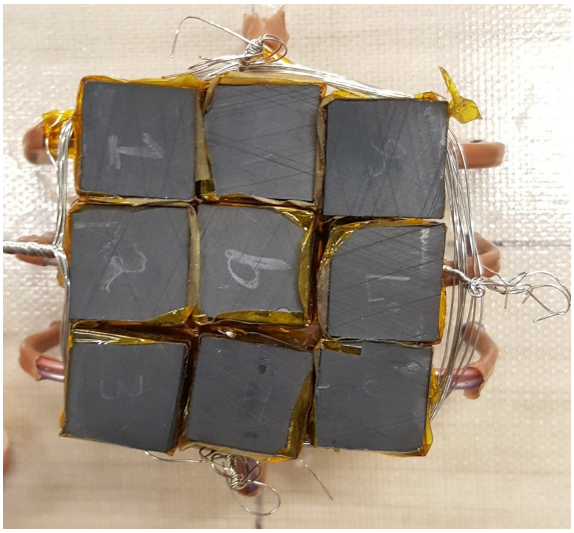

Figure 5.8: The calorimeter blocks are taped with Kapton and arranged in a 3 x 3 grid tied together by thin stranded wire.

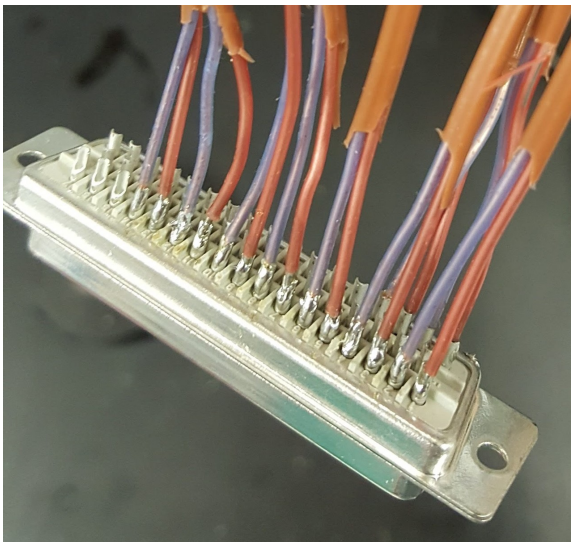

Figure 5.9: Each Copper and Constantan lead is soldered into a pin on the 50 pin connector [82].

5.7 Procedure for thermal output measurements via a direct contact graphite calorimeter

1) Clean Pyrex casserole dishes with water and soap. Pour de-ionized water into pyrex dishes and place in freezer overnight to create de-ionized water ice. Fill 1 gallon Pyrex jars halfway with de-ionized water and set in refrigerator on coldest setting overnight.

2) Repeat Steps 1-5 from "*Procedure for the preparation of neutralization measurements via a Faraday cup*" if necessary, removing the Faraday cup from the vacuum chamber.

3) Plug the 50 pin connector from the calorimeter into the 50-pin connector feedthrough. Plug the air side 50 pin connector into the 50 pin connector feedthrough.

4) Repeat Steps 7 - 13 from "*Procedure for the preparation of neutralization measurements via a Faraday cup*" as needed.

5) Remove ice from Pyrex casserole dishes and break up ice to fill the remaining volume of the 1 gallon Pyrex jar filled halfway with de-ionized water. Stir water & ice mixture to combine ice bath.

6) Place copper-constantan junctions from the air side thermocouple connections into the de-ionized ice-water bath taking care to prevent any two copper-constantan from touching one another.

7) Insert thermocouple wires into the NI 9205 following the channel layout in Table 5.1. See Fig. 5.10 for the finished set-up.

8) Using the USB connector, plug the NI 9205 into a computer. Open the data capture LabView vi for the Faraday cup.

9) On the main page of the vi, press Ctrl+E to access the wire diagram. Double-click on the DAQ Assistant. Click on each thermocouple to verify that the CJC (cold junction compensation) value is set to 0° C. Additionally, set the minimum temperature to 20° C and the maximum to 80° C. Save the vi program.

10) Repeat Steps 4 - 8 from "*Procedure for neutralization measurements via a Faraday cup*".

11) Press Beam Enable button. Once Beam Volts, Beam mAmps, and Accelerator Volts have reach desired values and the values are steady, wait 3 mins, then press Beam Enable button again to bring beam to standby mode.

12) Set mass flow controller #2 to 1 sccm and enable after 5 mins has elapsed in standby mode for the beam. Repeat step 11 for Beam mAmps at 22.8 mA for 0 - 10 sccm flow rates for mass flow controller #2 in 1 sccm increasing increments. Each test should consist of 3 mins of the beam enabled and 5 mins of the beam in standby mode.

13) Repeat Steps 11 - 15 from "*Procedure for neutralization measurements via a Faraday cup*".

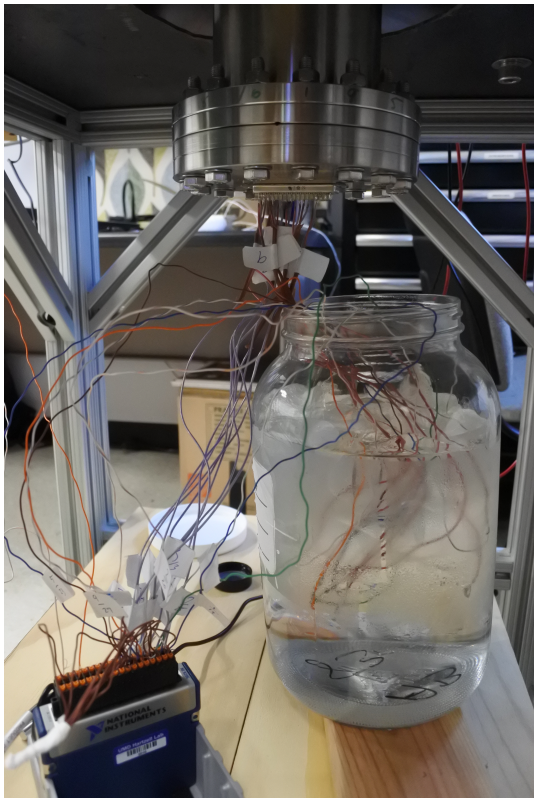

Figure 5.10: Air side of the thermocouple set-up. The copper-constantan junctions are separated in a de-ionized water-ice mixture. The copper leads are connected to the NI 9205 according to Table 5.1.

Table 5.1: Wiring Channels on NI 9205 for Calorimeter

Calorimeter	Vacuum Lead Channel	Copper-Constantan Lead Channel
1	1	19
2	2	20
3	3	21
4	4	22
5	5	23
6	6	24
7	7	25
8	8	26
9	9	27

Chapter 6: Performance and Characterization

This chapter will review the testing set-up at NASA MSFC and UMD to conduct thrust and neutralization measurements, respectively. Chapter 5 provides detailed instructions for building the diagnostics and the testing procedures. We present the thrust measurements for a novel low-power neutral beam technology demonstrator utilizing an error analysis method that enables thrust measurements during thermal drift. Additionally, we present the neutralization measurements as derived from Faraday cup data. The neutralization predictions from the COMSOL and analytical models from Chapter 4 is compared to the experimental data.

6.1 Technology Demonstration Description

Fig. 6.1 shows the neutral beam demonstration test set-up with the copper Faraday cup option (further discussed in Section 6.4). For our 1 keV neutral beam technology demonstration, we utilize a KDC 10 ion source [14] to generate argon ions at a 22.8 - 30.4 mA ion current. The KDC 10 requires an argon gas flow rate of 4 sccm to maintain the ion current. The gas flow rate to the ion source and to the gas diffusion neutralizer are controlled by separate Omega FMA-A2400 mass flow controllers [83]. Inside the KDC 10 ion source, a 0.25 mm diameter tungsten wire

cathode is heated, generating free electrons. The electrons interact with the argon gas to produce argon ions. Two accelerator grids are used to attract the ions (and prevent electrons from leaving the ion source) and accelerate them to 1000 V. The fast-moving ions exiting the ion source then enter the gas diffusion neutralizer, where they collect electrons from the neutral gas, thus becoming fast-moving neutrals. As discussed in Chapter 4, the background cold gas density must be $\sim 10^{14}$ cm^{-3} to neutralize the majority of the ions through recombination reactions. The geometry considerations for the neutralizer are discussed in Chapter 4. The technology demonstration device will use a 20 cm long gas diffusion neutralizer (Fig. 6.2) consisting of two parts: a 10 cm screened region and a 10 cm drift region. The gas is injected through eight barbed gas connectors that are spaced 45° azimuthally from one another 5 cm from the neutralizer entrance. The gas diffuses through the screen, creating a constant gas density in the screened region. The gas then flows downstream to the drift region and finally to the exit of the gas diffusion neutralizer. The entrance and exit of the gas diffusion neutralizer have an opening diameter of 2 cm to reduce the gas outflow rate in the gas diffusion neutralizer. The ions react with the background gas in the gas diffusion neutralizer, undergoing recombination and ionization reactions in both the screened and drift regions. The plume of energetic neutrals and ions then exit the neutralizer and travel downstream, where thrust (Section 6.3) or neutralization (Section 6.4) is measured.

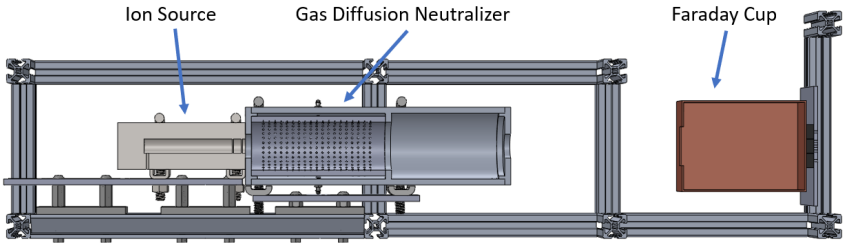

Figure 6.1: The 1 keV neutral beam test set-up with the copper Faraday cup. The ions are created and accelerated in the ion source. The ions then enter the gas diffusion neutralizer and interact with the background gas, undergoing recombination and ionization reactions. The energetic neutrals and ions then strike the Faraday cup where the neutralization is measured.

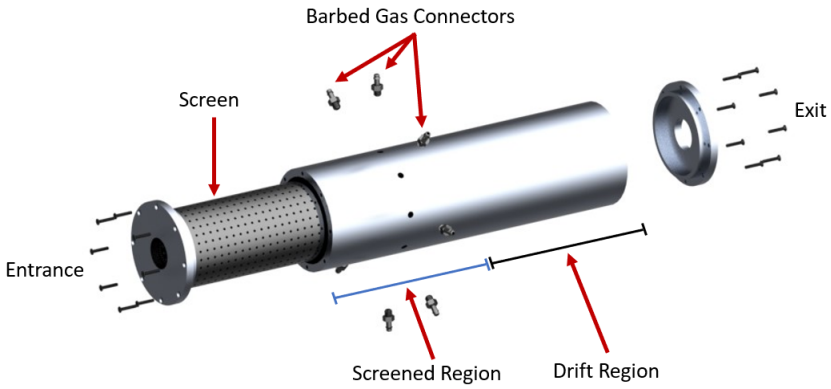

Figure 6.2: Exploded view of the gas diffusion neutralizer. The neutralizer consists of eight barbed gas connectors that are equally separated azimuthally about the neutralizer. A screen is inserted into the neutralizer to create a constant background density in the screened region.

6.2 Low Thrust Measurement Techniques

One common low thrust measurement technique is the use of a torsion thrust stand [53–55]. Torsion thrust stands are not ideal for small vacuum chambers but they are sensitive to micronewton thrust measurements [56]. A schematic of a

torsion thrust stand is shown in Fig. 6.3. The thruster is attached to an arm that is counterbalanced by a weight. The arm is attached to flexural pivots and a torsion spring provides the restoring torque. Mechanical vibrations are damped using an electromagnetic damper and the displacement of the torsion thrust stand is measured using a linear variable differential transducer (LVDT). An LVDT consists of a ferromagnetic core that slides freely inside a tube that has three solenoid coils surrounding it (see Fig. 6.4). Coil A (the central coil) is excited by AC and through induction, both B coils are excited. If the length of the ferromagnetic core is equally overlapping each B Coil, then the voltage across each B coil will be the same and the difference between the two is zero. This corresponds to zero displacement. If the ferromagnetic core overlaps one coil B more than the other, then there will be a voltage difference. This will correspond to the displacement of the arm and thus the measured thrust.

Another type of low thrust measurement method is the hanging pendulum thrust stand [58–60]. In this type of thrust stand (shown in Fig. 6.5), the thruster is mounted on an arm with the thrust vector parallel to the thruster mounting plate. The thruster center of mass should be in-line with the center of the pendulum arm. Leveling motors are used to make fine adjustments of the pendulum linkages to account for zero drift during testing. The zero point can drift due to heating of the thrust stand. An eddy-current damper is used to reduce mechanical vibrations. Calibration is carried out by exciting a solenoid at different currents to move a magnet which presses against a force transducer attached to the hanging pendulum arm. The current to the solenoid is regulated using a MOSFET to produce a square

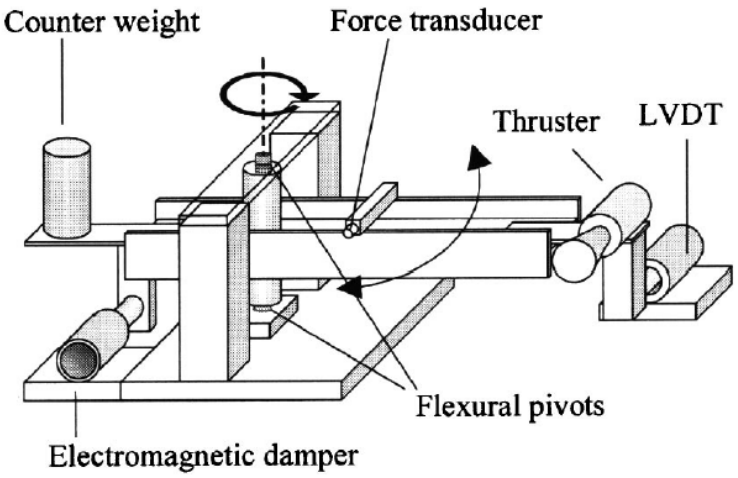

Figure 6.3: On a torsion thrust stand the thruster is affixed to an arm that is balanced via a counterweight. A torsion spring at the flexural pivots provides a restoring force. The electromagnetic damper reduces the mechanical vibrations and the LVDT measures the displacement of the arm. Figure reproduced from [55].

wave pulse of current [60]. On top of the pendulum arm linkage the displacement is measured using an optical linear gap displacement transducer (LGDT). This is different from the LVDT in that it uses an IR LED that is transmitted to a surface and the reflection is analyzed to determine the displacement [59]. The combination of the force transducer output and the LGDT produces a calibration curve. Additionally, the plate where the level sensors, leveling motor, damper, and LGDT are located is actively cooled using a water chiller. The hanging pendulum VAHPER thrust stand [60] is capable of measuring thrust from both pulsed and steady-state thrusters. This is the thrust stand that will be used in our experiments at NASA MSFC.

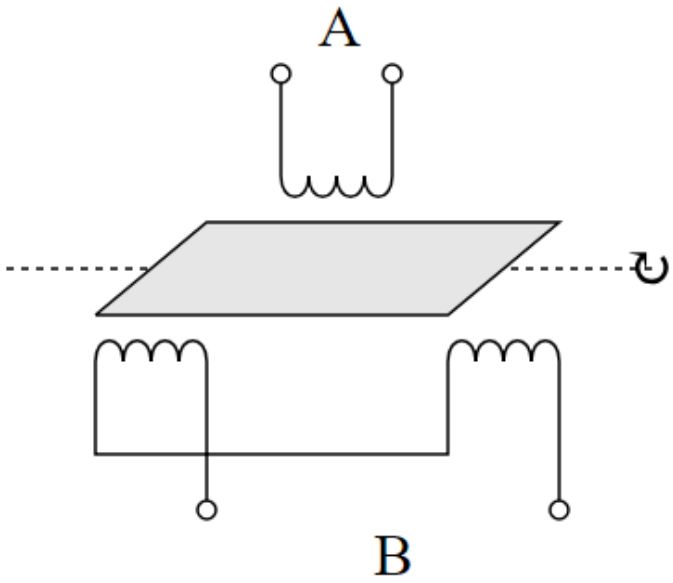

Figure 6.4: In a linear variable differential transducer (LVDT), a ferromagnetic core is free to slide in a tube surrounded by three solenoid coils. Coil A is excited and depending on the position of the ferromagnetic core, there will or will not be a voltage difference between the two B Coils. A voltage difference will correspond to a displacement whereas no voltage difference corresponds to a zero displacement. Figure reproduced from [57].

6.3 NBAC Thrust Measurement Data

Thrust measurements were performed using the hanging-pendulum VAHPER thrust stand described by Polzin *et al.* [59] at Marshall Spaceflight Center. Integration of the neutral beam and calibration of the thruster are covered in Chapter 5. The VAHPER thrust stand is enclosed in a 9 ft diameter, 25 ft long vacuum chamber capable of maintaining a pressure of 10^{-6} torr using two 2400 L/s turbopumps during testing of the neutral beam. The vacuum chamber has multiple feed-throughs for power, gas flow, and visualization purposes. More recently, we have upgraded

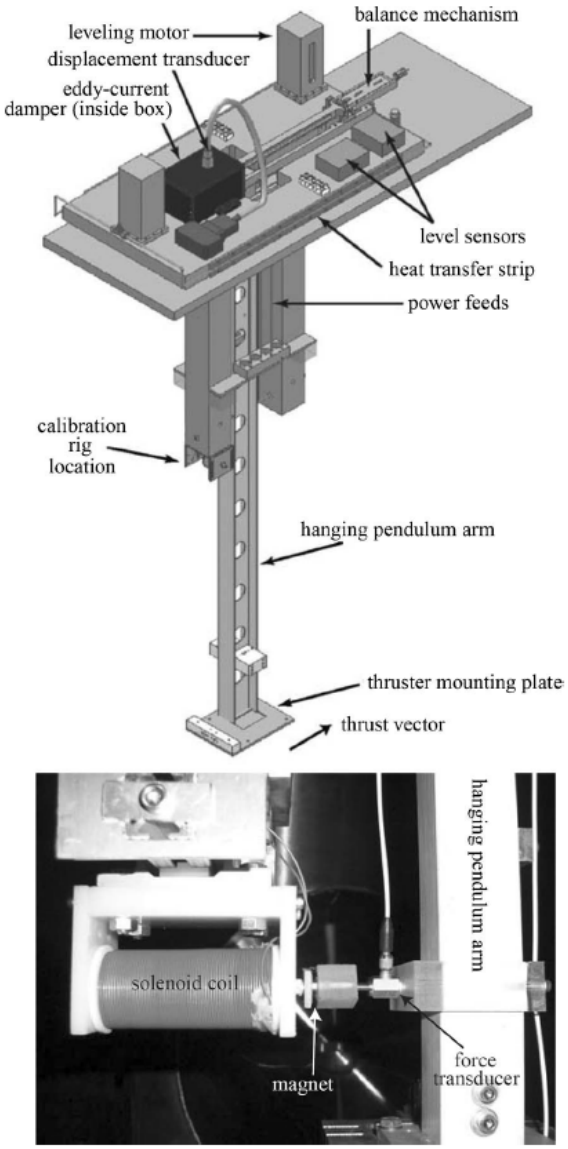

Figure 6.5: On a hanging pendulum thrust stand the thruster is affixed so that the thrust vector is parallel to the thruster mounting plate. Leveling motors are used to adjust the zero drift and a eddy-current damper reduces mechanical vibrations onto the thrust stand. The calibration set-up (bottom figure) uses a solenoid coil that pushes a magnet against the strhust stand where the force is measured by a transducer. An optical LGDT measures the displacement. Figure reproduced from [60].

the VAHPER thrust stand to enable greater thrust resolution sensitivity. The thrust stand now has a resolution of 10 μN. This was accomplished by attaching a mass sim-

ilar to the thruster to the VAHPER thrust stand and releasing the locking screws that secure the thrust stand hanging pendulum arm while not in use. Once the VAHPER oscillations had damped to a steady noise signature, data was acquired for the zero thrust case. This procedure was repeated several times and it was found that a 10 Hz repeatable signal was present in all cases. The LabView data capture program for the VAHPER thrust stand was modified to eliminate this signal. The resolution of the measured forces and position measurements have been improved as a result of this modification.

For steady-state thrusters, the VAHPER thrust stand has a Hookes Law response of:

$$F_T = k\Delta x \tag{6.1}$$

Calibration of the effective spring constant of the stand, k, is accomplished by applying known forces to the thrust stand via a piezoelectric motor and measuring the resulting deflection.

The thrust stand was recalibrated after each vacuum pump-down cycle to ensure accurate thrust data. Tests were conducted gas flow rates of 0-10 sccm into the gas diffusion neutralizer and for two different ion source beam currents (22.8 mA and 30.4 mA) at 1000 V. During testing, the ion source was allowed to heat to a steady state before the accelerator grids were activated. As the accelerator grids were turned on and off, signatures of instantaneous $\sim$ 100 μN changes in thrust were observed.

During testing, significant thermal drift was observed. To remediate this issue, electrical cabling to the thruster was arranged in a waterfall manner to reduce the thrust stand arm deflection that could be caused by cable heating. While cable heating still caused mild thermal drift in the zero position of the stand relative to the thruster-induced deflection, we show that this drift did not adversely affect the ability to measure thrust of the 1 keV neutral beam. Secondly, tests without gas flow were conducted to determine whether there was a repeatable thermal signature during the heating of the cathode and energizing of the accelerator grids. It was found that the apparent thrust induced by thermal strain in the wires was repeatable.

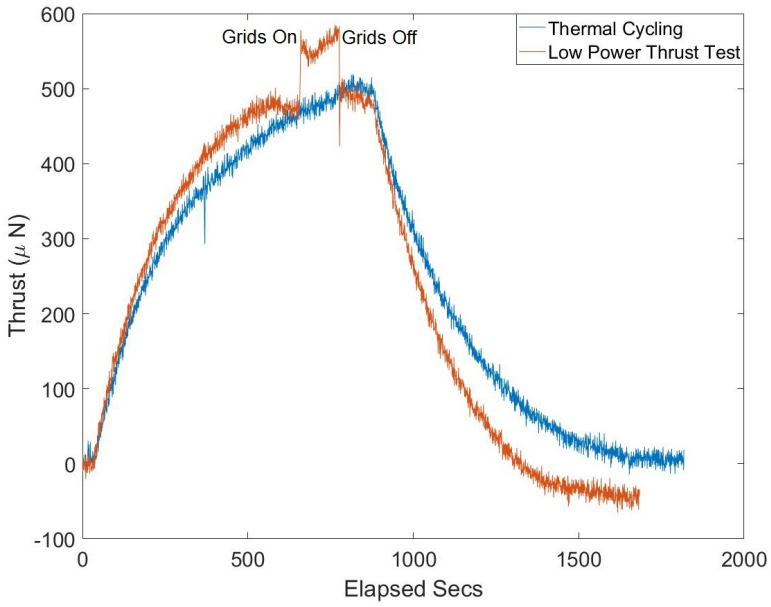

Figure 6.6: Measurements showing repeatability in thrust stand thermal drift. Shown is a pure thermal cycle (blue) and a test where the accelerator grids are cycled after the thermal drift has stabilized (red). This is for a flow rate of 4 sccm to the ion source at 1000 V and 22.8 mA.

Fig 6.6 shows the measured thrust (including thrust stand thermal drift) for

two separate tests of the neutral beam: one where there is only thermal drift in the test stand measurement and one where the accelerator grids are cycled on and off (accelerating the ions and producing thrust). The "false", thermally-induced thrust signal is relatively repeatable between the two tests. However, the real thrust is clearly observed in the instantaneous deflection when the grids are cycled on and off. Moreover, the change in measured thrust when the grids are turned on and off agree very well, implying that this signal is the real effect of the neutral beam thrusting. At low power, the neutral beam produced ~ 100 μN of thrust.

To expedite testing, we conduct tests before the ion source cabling reached a steady-state temperature (in other words, while the baseline "grid off" thrust value was still increasing). Fig 6.7 shows an example of multiple thrust measurements collected during the thermal ramp-up.

Because the measured thrust when the ion accelerator grids are off is time varying (because of the heating of the cables), in order to measure the thrust of the neutral beam, we must measure the *change* in thrust detected when the grids are turned on or off. The thrust measurement for each grid on/off cycle is only valid if the measurements vary by less than one standard deviation of the background measurement noise. Fig. 6.8 outlines our method for determining the standard deviation for each grid on/off cycle. Four standard deviations are calculated from each on/off cycle: before and after the grid is turned on and before and after the grid is turned off. The standard deviation for the measured thrust data is calculated considering data collected 10 - 50 seconds (in one second increments) before and after each on/off event. This varies the amount of points used to calculate the standard

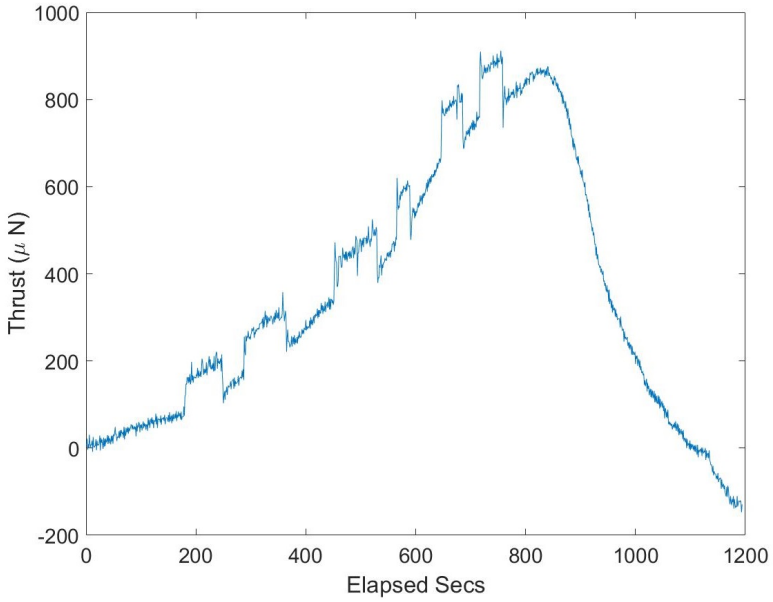

Figure 6.7: Testing during the thermal warm-up of the test stand with instantaneous thrust measured when the thruster was turned on and off.

deviation. Of those standard deviations calculated for each event, the minimum standard deviation is chosen for each of the four. This provides a conservative error in the data for determining whether or not the thrust measurement from each on/off cycle overlap within a standard deviation. The minimum standard deviation of each is then used to calculate the total standard deviation of the on/off event. For example, σ_{1R} is the minimum standard deviation of the 10 - 50 seconds of apparent thrust data before the grid is turned on and σ_{2R} is the minimum standard deviation after the grid is turned on. The total standard deviation is then calculated using Eqn. 6.2.

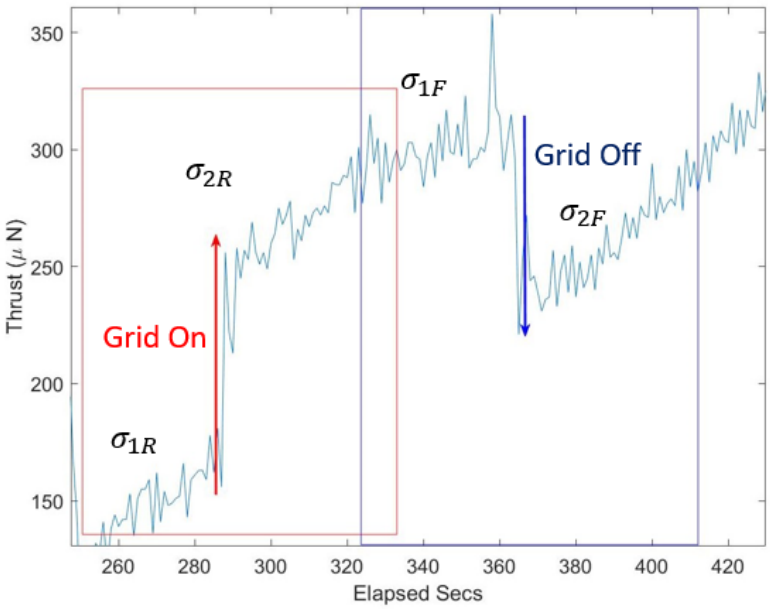

Figure 6.8: The standard deviation of each on/off cycle is determined by finding the minimum standard deviation of the apparent thrust data before and after each on/off cycle. σ_{1R} = minimum before grid on, σ_{2R} = minimum after grid on, σ_{1F} = minimum before grid off, σ_{2F} = minimum after grid off

$$\sigma_R = \sqrt{\sigma_{1R}^2 + \sigma_{2R}^2} \qquad \sigma_F = \sqrt{\sigma_{1F}^2 + \sigma_{2F}^2} \tag{6.2}$$

Where σ_R is the standard deviation for the measurement noise for the "grid on" case and σ_F is the standard deviation for the measurement noise for the "grid off" case. We then use the inequality in Eqn. 6.3 to validate whether the thrust measurement from each grid on/off cycle overlap with one another:

$$F_{TR} - \sigma_R \leq F_{TF} + \sigma_F \qquad or \qquad F_{TR} + \sigma_R \leq F_{TF} - \sigma_F \tag{6.3}$$

Where F_{TR} is the measured thrust for when the grid is turned on and F_{TF} is

the measured thrust for when the grid is turned off. We verified that the rises/falls from cycling the grid on and off were relatively similar, as shown in Fig. 6.9. For all measurements the error bars for thrust on the rises and falls for each cycle overlap. Thus, measurements of thrust taken during the thermal ramp-up are valid.

In our predictions of the performance of the neutral beam technology demonstration from Chapter 4, we assumed that the energy of the fast moving ions did not decrease during recombination (i.e. that there was no 'drag' on the ion beam due its interaction with the neutral gas in the diffuser). Given this assumption, we would not expect the thrust to change as a function of the neutralization gas flow rate. Fig. 6.9 shows no strong correlation of thrust with increasing gas flow rate over the range tested. Notably, there is no significant change in the measured thrust even when comparing the performance at 0 sccm (i.e. ion source only, no neutralization) to the cases with neutralization. Thus, our assumption that higher density cold gas does not significantly affect the produced thrust is valid.

We can predict the thrust of the neutral beam using Eqn. 6.4:

$$F_T = \sqrt{\frac{2eV}{M}}\frac{IM}{e} \tag{6.4}$$

The predicted thrust for an argon beam at 1000 eV and 22.8 mA is 656 μN while the actual measured thrust for no neutralizer flow rate was 104 $\pm$ 15 μN, an underperformance of 84.1%. The discrepancy is due to defocusing of the beam due to the image charge generated in the grounded, metal neutralizer rather than from the plume spread at the exit. The ion current is then lost to the neutralizer,

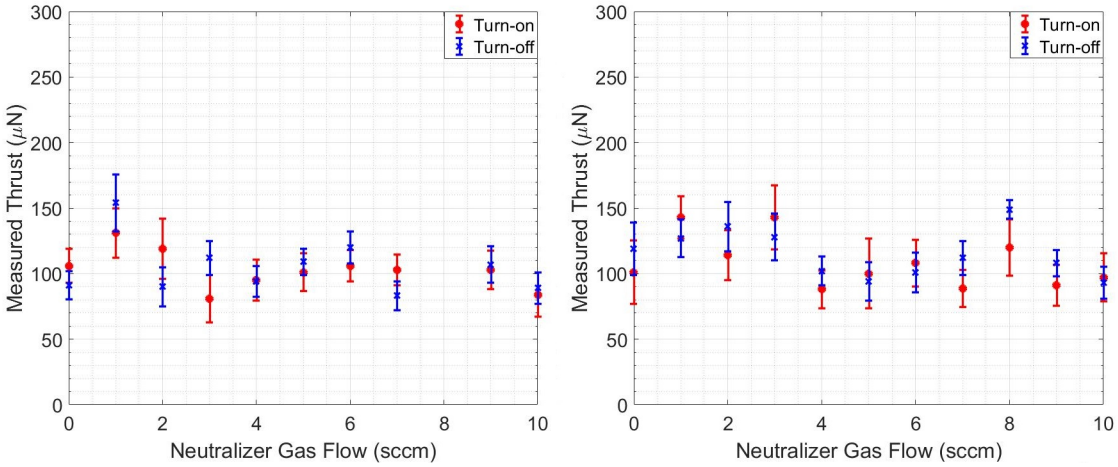

Figure 6.9: Thrust measured using the VAPHOR test stand as a function of neutralizer gas flow rate. Thrust was measured during the thermal ramp up, thus the thrust measured when the ion beam accelerator grids were turned on an off are plotted. The thrust measured when the accelerator grids are turned on and off are consistent. Additionally, the thrust data shows no evidence to suggest that drag from the cold gas in the neutralizer retarded the thrust. (Left) Low current (22.8mA) and (Right) higher current (30.4mA) thrust measurements acquired on thruster turn-on and turn-off. The measurement for 8 sccm in the 22.8mA test is absent due to a de-focusing event.

resulting in a lower than expected thrust. For a neutral beam thruster ready for spaceflight, the neutralizer should be constructed from a high temperature, low sputtering, non-conductive material such as a Beryllium Oxide.

6.4 Neutralization Measurements via Faraday Cup

For neutralization measurements, the neutral beam technology demonstration was tested at the University of Maryland. The vacuum chamber consists of an 18 in. diameter, 28 in. tall bell jar that rests on a 20 in. diameter, 11 in. tall stainless steel base. On the stainless steel base are two ports for gas flow control, one port

for power to the ion source, one visual port, and one data feedthrough port. The pumping speed of the turbopump is 290 L/s and is able to maintain a pressure of $4{\cdot}10^{-4}$ - $1{\cdot}10^{-3}$ torr, depending on the neutralizer flow rate. This vacuum pressure is within the operating range for the KDC 10 ion source. The neutralization of the energetic argon ions is measured using a Faraday cup. A Faraday cup is designed to measure the ion or the electron current [84, 85]. It does this by capturing ions or electrons and neutralizing them. Faraday cups are made from a conductive material, typically copper, and are electrically isolated from ground save for one connection. Faraday cups have a small opening for the ions to pass through to prevent charged particles from escaping. If an ion bounces from its first contact with the interior of the Faraday cup, then subsequent collisions will neutralize the ion without it escaping from the cup. Faraday cups must be in a vacuum environment to avoid measuring charge caused by ionization of air. This is particularly a problem as the ions in this study will have an energy of 1 keV where the first ionization potential of nitrogen is 14.5 eV [86]. Fig. 6.10 outlines the schematic of the test setup. The ions and neutrals emitted from the neutralization chamber enter the copper Faraday cup. The only path from the Faraday cup to ground is via a wire in series with a resistor. To neutralize an ion impinging on the Faraday cup, an electron flows from ground to the Faraday cup. The potential across the resistor is measured using an National Instruments NI 9205 and the current is then derived using Ohm's law. We use the same range of neutralizer flow rates (0 - 10 sccm) and the the 22.8 mA ion beam current. The current draw at each flow rate is compared to that at zero flow rate:

$$I_i = \frac{V_i}{R} \qquad \eta_i = 1 - \frac{I_i}{I_0} \qquad i = 0, 1, 2, ... \tag{6.5}$$

Where I is the current, V is the potential difference, R is the resistance, and i is the index for the neutralizer flow rate.

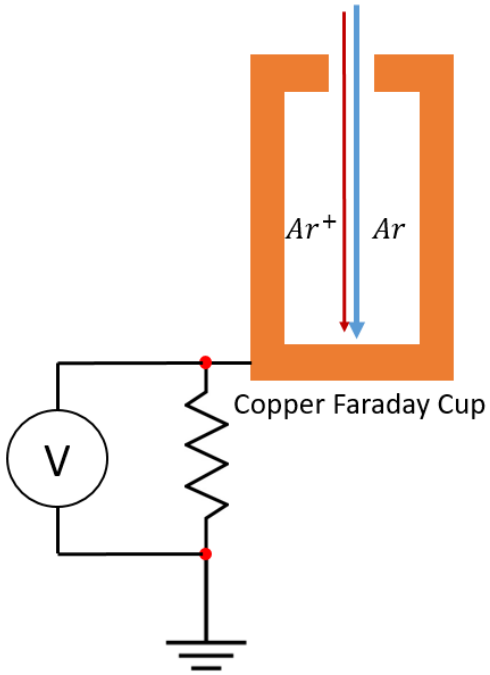

Figure 6.10: The ions and neutrals exiting the neutral beam neutralization chamber strike the copper Faraday cup. The potential difference across the resistor to ground is measured as the ions are neutralized.

In Chapter 4.1, we showed that the linear background density of gas required to maximize neutralization of argon ions in the 1 - 10 keV range follows the relation:

$$nL = 8 \cdot 10^{14} V^{0.1315} \quad [cm^{-2}] \tag{6.6}$$

For a 1 keV neutral beam, the linear density must be $\sim 2{\cdot}10^{15}$ cm^{-2} in order to maximize neutralization. We use an analytical model [74] for the mass flow

needed in a gas diffusion neutralizer for a molecular flow where viscosity and slip are included (Eqns. 6.7 & 6.8).

$$K_n = \frac{1}{\sqrt{2}\pi D_{HS}^2 nr} \tag{6.7}$$

$$\dot{m}_n = \frac{-\pi r^4 (n k_B T)^2}{1.6\mu_0 RTL} (1 + \alpha K_n) \left(1 + \frac{4K_n}{1 + K_n}\right) \tag{6.8}$$

Where α is a parameter for the rarefaction coefficient ($\alpha = 1.358$ for pipe flow). Fig. 6.11 presents the neutralization data as a function of neutralizer flow rate. The data is compared to the analytical model and COMSOL models from Chapter 4. The error bars constitute the standard deviation between the data runs for the six trials. The maximum neutralization achieved is 87.14 ± 0.82% at 10 sccm. At 7 sccm, the large majority of ions is neutralized (85.78 ± 0.83 %) with only minimal gains for further increases in neutralizer gas flow rate.

The neutralization data is within one standard deviation of the COMSOL model, but does not agree with the analytical model. The analytical model underestimates the gas density in the gas diffusion neutralizer which then predicts an inaccurate neutralization achievable for a given flow rate. For example, for a flow rate of 1 sccm, COMSOL predicts an average gas density of $1.05{\cdot}10^{19}$ m^{-3} while solving for the density from Eqn. 6.8, the density predicted is $7.39{\cdot}10^{18}$ m^{-3}. The density underestimate from Eqn. 6.8 then predicts 31.8% neutralization as opposed to the COMSOL prediction of 44.5% and the measured value of 41.17 ± 3.60%. One contribution to this error is the Knudsen number ranges from 3 - 30 in the gas diffusion neutralizer. This indicates that the nature and frequency of gas atom

reflection from the wall of the neutralizer will likewise change. If this frequency increases the gas atom takes a more circuitous path to exit the neutralizer and the average background density increases. This increases the number of recombination reactions leading to a higher neutralization. Using the average density from the COMSOL model for a given mass flow rate in Eqn. 6.8, we can determine the α parameter. Using the derived α parameters, we use a 2^{nd} order polynomial fit to determine α for a given flow rate (where the flow rate unit is in sccm):

$$\alpha = -1.49(10^{-4})\dot{m}_{sccm}^2 - 7.77(10^{-3})\dot{m}_{sccm} + 0.9575 \tag{6.9}$$

Applying this expression for α provides an accurate representation of rarefaction and that of the average gas density in the gas diffuser neutralizer design. This modified model is plotted in Fig. 6.11. It is accurate for low flow rates (compared to the COMSOL model and experimental data) but deviates for higher flow rates.

To understand the effect of each particle, let us break down each step in time. As the ion enters the Faraday cup, an image charge is drawn from ground. We measure the current through the resistor (connected to ground) for each of these ions. So long as the ions do not escape the interior of the Faraday cup before they are neutralized, the current measured will be consistent with the ions that entered the Faraday cup. Faraday cups have an opening that is small compared to the surface area of the interior. As the ions and neutrals impact the Faraday cup, there will be some amount of backscattering and sputtering. Using TRIM [77], we model 1 keV Argon impacting a 1/8" thick copper flat plate at a normal incidence angle. TRIM

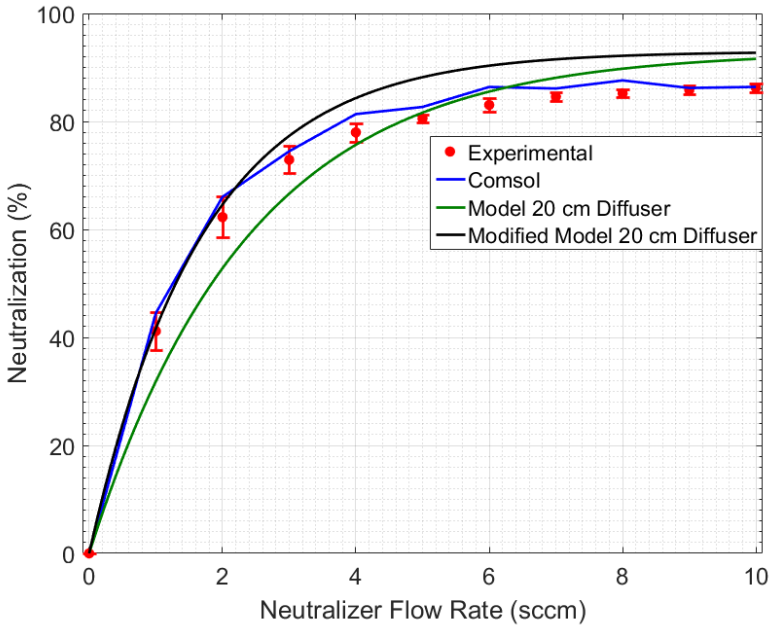

Figure 6.11: Neutralization of the neutral beam for flow rates ranging from 0 - 10 sccm. The data is compared to the analytical model and COMSOL results from Chapter 4. Additionally, the modified analytical model to account for the variation in the α parameter is presented. The experimental data shown is the mean of the six trials and the error bars are the standard deviation of those trials.

predicts 7% backscattering and a sputtering yield of 3.8 atoms per incident particle. The sputtered atoms have an energy of 22 eV, meaning some will be hot neutrals, singly ionized, or doubly ionized. However, in each of the cases of the sputtered particles, charge conservation holds. This means that there is no need for a current draw from ground as the electrons that were associated with sputtered particles that have ionized are still in the Faraday cup. If the copper ions and electrons do not escape the interior (due to the small opening) before the copper ions re-impact and neutralize, then there will be no net current draw due to these sputtered particles. The same explanation is true for backscattered ions. These also do not require an

additional current draw as the electrons that were previously associated with them are still in the system. Thus unless, there is significant escape of the backscattered ions or sputtered copper from the Faraday cup, the current measurements are not affected by either.

The Faraday cup assembly also allows us to investigate the loss of the ion current to the neutralizer. High energy ions that impact the neutralizer housing rather than flowing into the neutralizer decrease the efficiency of the neutral beam assembly. The ion current to the neutralizer housing can be caused by: 1. gas diffusion neutralizer misalignment with respect to the ion source and 2. plume expansion in the neutralizer that is exacerbated by image charges on the wall of the neutralizer. To characterize the ion current to the neutralizer housing, we conducted a 12 trials where the neutralizer was removed from the assembly and the ion source was directed into the Faraday cup. The ion source was set to 1000 V, 22.8 mA with a 4 sccm argon flow into the source. The measured current to the Faraday cup is 6.09 $\pm$ 0.05 mA for this case. We conducted 6 trials for when the neutralizer is included in the assembly but the gas flow rate to the neutralizer is 0 sccm; the current is 0.96 $\pm$ 0.05 mA. The significant decrease in the current to the Faraday cup (84.3 $\pm$ 0.6%) caused simply by the physical addition of the passive neutralizer assembly indicates that there is a significant current to the neutralizer assembly. Recall from Sec. 6.3 that the measured thrust underperformed as compared to the predicted thrust. The loss in thrust for the neutralizer in line with the ion source (84.1%) and the loss in current from the Faraday cup (84.3 $\pm$ 0.6%) are consistent with one another. Note that for these results, there is no neutralizing flow into the

system, so the current losses are not due to neutralization of the ions by a neutral gas. In the experiment presented, the neutralizer was grounded which enabled an electron current from the ground to create an image charge density on the interior of the neutralizer, defocusing the ion beam. In the tests where there is a non-zero neutralizer flow rate, the image charge density will decrease per unit length of the neutralizer as more ions are neutralized through recombination reactions. However, there will still be defocusing as the ions enter the neutralizer since the image charge density will be proportional to the ion current density.

6.5 Discussion

By improving the thrust resolution of the VAHPER thrust stand to ~ 10 μN, we have enabled testing of the neutral beam technology demonstrator. This thruster produced approximately 100 μN over the range of neutralizer flow rates. There is no strong evidence for momentum loss collisions in the gas diffusion neutralizer as there is no correlation for decreasing thrust with increasing neutralizer flow rate. By developing a method to take thrust measurement during thermal drift of the hanging pendulum thrust stand, we have enabled the rapid characterization of sub-Newton thrusters.

An alternative means to determine the thrust that would negate reliance on point to point calculations would be to use a linear regression fit for each segment. Thrust would then be calculated using the difference in the y-intercepts and the standard deviation would be that of the confidence interval of the y-intercept. A

three-point moving average could also be applied to the raw thrust data before calculating the regression fit; this would decrease the effect of outliers skewing the fit and calculating an inaccurate thrust.

Using a Faraday cup to determine the neutralization of a beam, we have confirmed the predictions from COMSOL for the neutral beam. By modifying the α parameter, we can accurately predict neutralization for lower gas flow rates with deviation of the asymptotic neutralization at higher flow rates.

Chapter 7: Calorimetry of a Neutral Beam

In our one dimensional model for neutralization from Chapter 4, we considered two primary reactions: ionization and recombination. Neutralization was calculated by using the reaction cross-sections and the gas background density. It was assumed in the model that momentum loss collisions do not significantly influence the beam energy. In Chapter 6, we measured the thrust of the neutral beam technology demonstrator at NASA MSFC. We used a range of neutralizer flow rates (0 - 10 sccm) and there was no strong evidence for thrust loss due to increasing neutralizer flow rate. In other words, there was no evidence for kinetic losses of the beam energy due to increasing gas flow rate from our thrust data.

Physically, as the flow rate increases to the neutralizer, the background density increases. Neutralization increases for background density (Eqn. 4.1) due to an increase in the collision frequency. If there are more collisions we should expect that some of these will be momentum exchange reactions. Any momentum exchange collisions that occur would transfer some of the beam ion energy to the background gas in the gas diffusion neutralizer, leading to kinetic losses. Increases in background gas density would increase the heat transfer rate. In this Chapter we present the calorimetric data of the neutral beam technology demonstrator and again look for

evidence of momentum loss due to gas-ion collisions. We will use the calorimeter data to predict the expected thrust and compare that to the VAHPER thrust stand measurements from Chapter 6.

7.1 Graphite Calorimeter Experiment Set-up

Calorimeters measure the thermal output of a heat source. One method is using a slug calorimeter, as described in ASTM Standard E457-08 [87]. We have built a graphite slug calorimeter that is in-line with the gas diffusion neutralizer. Slug calorimeters consist of a highly conductive material that is isolated from other surfaces and whose temperature is measured using a thermocouple. As the block heats up, the thermocouple does as well and produces a current due to the Seebeck effect. The measured voltage can be converted to a temperature and the evolution of temperature over a time frame can be recorded. We use graphite as the material for energetic ion and neutral impingement as it is highly conductive (108 W/(m·K) [88]) and the carbon-carbon bonds help minimize the mass loss from the energetic impingement. Detailed instruction for building the graphite calorimeter and testing are outlined in Chapter 5. We affix a T-type thermocouple (Constantan-Copper) to the back of the graphite block using epoxy. The sides of each block are taped with kapton to minimize arcing between each graphite block. Nine graphite blocks are arranged in a 3x3 grid and the grid is centered underneath the output neutral beam. Fig. 7.1 presents a schematic of the test set-up. The thermocouple wires are attached to a pin connector and plugged into a pin feed-through. On the outside of

the vacuum chamber, the constantan wire from each thermocouple is soldered to a copper wire to create another thermocouple and is placed in a de-ionized ice water bath to act as the cold junction. The copper wire from that bath and the copper wire from the graphite thermocouple are then the two leads wired to the NI 9205. For testing, the beam impinges on the calorimeter for 3 mins and then is turned off for 5 mins to allow the calorimeter to cool. This experiment is repeated over the range of gas flow rates into the neutralizer (1 - 10 sccm). The output power is determined using ASTM Standard E457-08 [87]. The specific heat of graphite is calculated using values from [89].

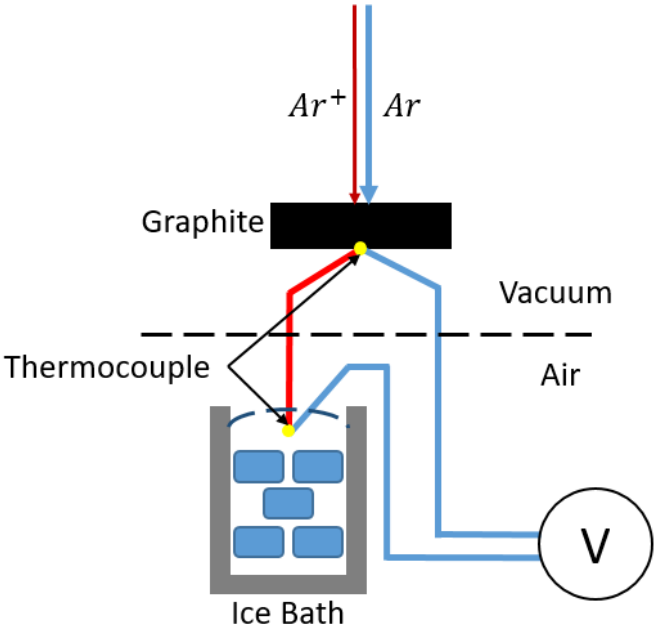

Figure 7.1: Graphite is used for the calorimeter with a T-type thermocouple affixed to the back. A de-ionized ice water bath is used as the cold junction.

7.2 Kinetic Losses from Neutralization

The nine calorimeter blocks, each on a separate channel, record the change in temperature via a thermocouple as the blocks heat up from the neutral beam. We use Matlab for regression analysis on the rise in temperature and the subsequent fall as the neutral beam is turned off. Fig. 7.2 shows an example of the output temperature data with the regression fits.

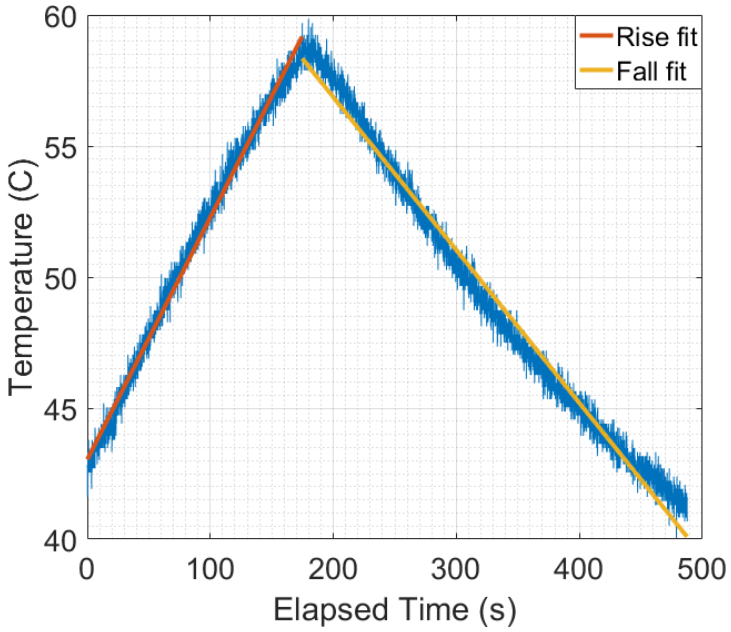

Figure 7.2: An example of the temperature profile of a calorimeter block for a full cycle of neutral beam testing. The rise in temperature is due to the neutral beam striking the calorimeter and the fall is due to the neutral beam being turned off. Regression fits are found for the rise and fall separately to determine the total power to the calorimeter.

From ASTM Standard E457-08 [87], the total thermal power imparted by a source is the sum of the measured power while the source is on and the power losses

from the calorimeter. The losses can be measured directly by turning the source off and using the cooling curve portion of the data to represent total loss rate. In our data the total temperature change rate is:

$$\frac{\Delta T_c}{\Delta t} = \frac{dT_{rise}}{dt} + \left|\frac{dT_{fall}}{dt}\right| \tag{7.1}$$

Where ΔT_c is the measured change in temperature (K), and Δt is the change in time (s), dT_{rise}/dt is slope of the temperature data while the source is on, and dT_{fall}/dt is the slope of the temperature data while the source is off. Using the 1-D heat conduction equation:

$$Q = \frac{M_c c_p}{A_c}\frac{\Delta T_c}{\Delta t} \tag{7.2}$$

Where Q is the heat transfer rate (W/m^2), M_c is the mass of the slug calorimeter (kg), c_p is the average specific heat of the slug calorimeter ($J/kg \cdot K$), and A_c is the cross-sectional area of the slug calorimeter (m^2). We can combine the temperature data from all nine calorimeter blocks and find the total heat transfer rate from the neutral beam to the calorimeter. Repeating this for all neutralizer flow rates, we can compare the heat transfer rate for increasing neutralizer flow rate:

$$Q_{si} = \frac{Q_i}{Q_0} \qquad i = 0, 1, 2, ... \tag{7.3}$$

Where Q_s is the scaled heat transfer rate compared to Q_0 (the heat transfer rate for no neutralizer flow) and i is the index for neutralizer flow rate. The measured heat transfer rate is analogous to the beam energy and the scaled heat transfer

rate is the measurement of the beam energy relative to the beam energy when no neutralization is present. Therefore we can use Q_{si} to determine whether the measurement of heat transfer rate indicates a decrease in thrust due to momentum losses during neutralization for increasing neutralizer flow rate. Modifying the thrust from Eqn. 6.4:

$$F_{Ti} = \sqrt{\frac{2Q_{si}eV}{M}}\frac{IM}{e} \qquad i = 0, 1, 2, ... \tag{7.4}$$

Applying this to the data from Chapter 6.3, we can use thrust from the no neutralization test (0 sccm) and Q_{si} to predict the thrust for each neutralizer flow rate. Fig. 7.3 compares these two results.

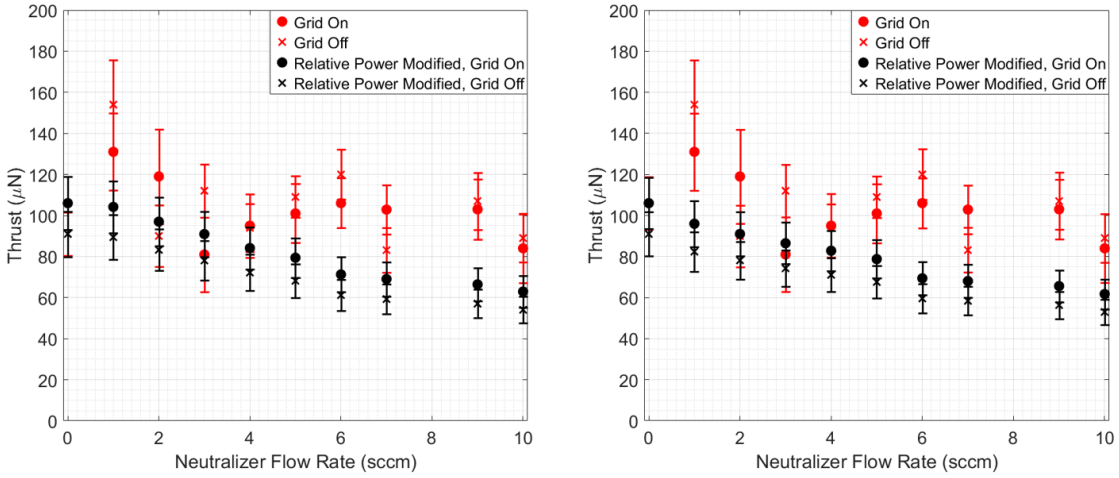

Figure 7.3: The thrust measurements of the neutral beam technology demonstrator are compared to the thrust predicted by the calorimeter data. The thrust measurement from the VAHPER thrust strand show no evidence for kinetic loss for increasing flow rate. The derived thrust from the calorimeter data, while appearing to show a correlation for decreasing thrust for increasing neutralizer flow rate, is not as sensitive as the VAHPER thrust stand and merits further investigation at higher beam energies.

7.3 Discussion

The error bars for the modified thrust (1 sigma) are a combination of the slope error and the measurement error from the no neutralizer flow test. As was previously discussed in Chapter 6.3, the neutral beam technology demonstrator thrust data (red in Fig. 7.3) shows no evidence of kinetic energy loss for increasing neutralizer flow rate. The derived thrust calculated using the calorimeter data (black in Fig. 7.3) appears to show a correlation for decreasing thrust for increasing neutralizer flow rate. In Fig. 7.3, the error bars from some of the modified thrust predictions overlap with that of the measured thrust. However, the results are not well-matched with one another. This could be due to the fact that the calorimeter is not as sensitive as the VAHPER thrust stand. This issue of kinetic losses does merit further investigation as while it may not be significant in our technology demonstrator that operates at 1 keV, this problem could potentially be exacerbated by increasing the energy to 10 keV. At this energy, the background density to maximize neutralization (recall Eqn. 4.4) increases by 36% as compared to the density needed for 1 keV ions. This increase in density will lead to more collisions between high energy particles and the background gas which would lead to higher kinetic losses if there are momentum exchange collisions. Reducing this kinetic energy loss is important to prevent loss in thrust for the neutral beam.

Chapter 8: Conclusion and Future Work

This thesis has shown that neutral beam electric propulsion is a possible solution to asteroid control and can be realized for kilowatts of power. Propulsive control of asteroids offers a precise method for changing the orbit and rotation state. Neutral beam propulsion eliminates charge coupling between the spacecraft and its target. In this chapter we will review the conclusions from this research and outline future work that can be undertaken to realize propulsive deflection and control of asteroids through neutral beam emitting spacecraft.

8.1 Conclusions

In Chapter 3 low-thrust deflection and de-spin of hypothetical asteroid 2017 PDC using neutral beam emitting spacecraft was investigated. We have presented the range of asteroid sizes that could be deflected and/or de-spun by a 4 NBAC spacecraft system, considering a range of spectral types and spin rates, and assuming the orbit for the hypothetical asteroid 2017 PDC. Investigating the effect of uncertainty on density to achievable deflection showed that C-type asteroids have the greatest range of sizes that can be deflected as compared to other spectral types. The maximum size that could be deflected was similar for B and S types (73m and

69m, respectively) under our low-thrust deflection method. Investigating single and double thruster failure at different times of the deflection mission, provides bounds in asteroid radius for each spectral type. NBAC can handle a variety of asteroid spectral classes with a maximum mass of 3.8×10^9 kg for a 420 day campaign, deflecting them to over 200 km from an Earth impact. Using multiple spacecraft is resilient in terms of providing adequate deflection and reduces the probability of system down-time during the deflection campaign. NBAC is also suited for slowing or arresting the rotation of some asteroids. Partial arrest increases the surface gravity thus increasing the asteroid strength for future missions to grapple the asteroid in order to tow it to another orbit. The propellant mass per spacecraft for total arrest of the asteroid is typically less than 60 kg per spacecraft which is reasonable considering the mission duration and thrust levels achieved with NBAC. For fast rotating asteroids ($P_0 \leq 2$ hrs), there are some solutions for partial arrest of these bodies within a half orbital period. Fast rotating C, B, and S-type asteroids can be partially arrested while Xc-type asteroids are unlikely to be partially arrested. Unlike work from [12, 18, 33, 45] who use ion propulsion or solar sails to control an asteroid's rotation or orbit, we established that low-thrust asteroid de-spin and deflection via neutral beam spacecraft is effective for sub-kilometer sized asteroids and resilient against spacecraft failure.

In Chapter 4 we conducted a system-level study of the neutral beam, altering the electric propulsion performance equations to account for changes brought upon by an additional gas flow rate for the gas diffusion neutralizer. The optimal background gas density necessary for the greatest global neutralization of an argon ion

beam as a function of beam energy is calculated. The additional flow rate is derived using a slip, molecular flow relationship for flow in cylindrical tubes that accounts for the viscosity of the fluid. The mass utilization efficiency decreases as a result of introducing two flow rates into the system, but the specific impulse for high energy argon neutral beams maintains acceptable efficiencies for long-term operation in space. COMSOL simulations demonstrate that high neutralization efficiencies can be achieved with low gas injection rates for cylindrical neutralization chambers that have an annular screen at the injection zone and a partially open chamber end geometry to limit the outflow of the gas. The length of the injection zone, while having an effect on the gas density profile, has a minor influence on the total neutralization. This work is unique in neutral beam design as the neutral beams in [15, 46, 48, 49, 51, 52] utilize differential pumping to control the gas density in the beam-line tube to neutralize the ions. Our design is a self-contained gas diffusion neutralizer that precisely controls the injected gas flow. It could be added as a neutralization stage to a gridded thruster with only minor adjustments for neutralizer diameter and opening diameter. The work in Chapter 4 provides the first analysis to show that neutral beams are scalable for keV electric propulsion for spacecraft. We also develop theory and simulation data for neutral beam performance based upon our unique design that uses a self-contained gas diffusion neutralizer.

In Chapter 6 we present our thrust and neutralization measurements for the neutral beam technology demonstrator. The thrust resolution of the VAHPER thrust stand at Marshall Spaceflight Center has been improved to ~ 10 μN. The 1 keV neutral beam technology demonstration produced ~ 100 μN of thrust over the

range of neutralizer flow rates. Additionally, we developed a method by which thrust measurements on a hanging pendulum thrust stand can be taken during thermal drift. The thrust measurements between grid on/off cycles match one another within one standard deviation of the measurement noise. Our predictions of neutralization through our work with COMSOL in Chapter 4 are consistent with the Faraday cup measurements. The analytical model presented in Chapter 4 does not accurately predict the neutralization of the beam for a given flow rate in the neutralizer because it underestimates the background gas density. This is due to changes in the Knudsen number over the range of gas flow rates. Modifying the model by solving for the α parameter produces an accurate average gas density which predicts the neutralization well for low flow rates. The high energy ion current and thrust loss due to the presence of a neutralizer are consistent with one another. This work in Chapter 6 demonstrates that thrust measurements on a hanging pendulum thrust stand for sub-Newton propulsion can be taken during thermal drift. For a hanging pendulum thrust stand [58–60], this is the first time that it has been shown that reliable thrust measurements for a sub-millinewton electric thruster can be taken during thermal drift. Additionally, our experimental performance for the low power neutral beam were validated against the theory and simulation data from Chapter 4. This unique thruster has been shown to match predictions on its neutralization efficiency and demonstrates that gas diffusion neutralization (unlike asymmetric ion compression in [63]) is an effective way to globally neutralize and ion beam for propulsion.

In Chapter 7 we present calorimetric results from the neutral beam technology demonstrator and compare them to the thrust results from Chapter 6. This is to

investigate whether there is evidence for momentum loss due to gas-ion collisions. We built a graphite slug calorimeter divided into nine segments and measured the thermal output from the neutral beam technology demonstrator over a range of gas flow rates. We scale the heat transfer rate to the calorimeter from the neutral beam for increasing neutralization flow rate to no neutralization. The derived thrust from the calorimeter appears to show a correlation for decreasing thrust for increasing neutralizer flow rate. Comparing derived thrust from the calorimeter to the VAHPER thrust, the results are not matched within one standard deviation. However, the calorimeter sensitivity is lower than the VAHPER thrust stand and merits further investigation at higher energy levels to determine if there is a momentum loss of the beam due to neutralization.

8.2 Future Work

In the asteroid de-spin and deflection area of research, there are several avenues for significant contributions. Control laws for long term proximity operations about tumbling asteroids should be developed. Tumbling asteroids add a unique challenge as they are chaotic rotators and determining how to safely operate about these bodies and decrease their rotational momentum is essential. Expanding these control laws to include several spacecraft would also be useful. Low-thrust deflection of the PHA population including launch and rendezvous opportunities to these objects is another useful future contribution. An application that is able to gather updated ephermerides of these bodies and use a program such as GMAT [67] or Evolutionary

Mission Trajectory Generator (EMTG) [90] to solve for the trajectory to the PHAs and the necessary deflection would be useful for future mission scenarios. This program could be used both for deflection purposes and expanded to include moving asteroids to orbits that are preferable for asteroid mining opportunities.

For the neutral beam, a gas diffusion neutralizer made from a non-conductive, low sputtering, high temperature material such as Beryllium-Oxide should be manufactured and tested with the current neutral beam technology demonstrator test set-up. This will eliminate the image charge problem and increase the measured thrust, specific impulse, and mass utilization efficiency. Once these issues are resolved, a compact assembly to deflect the ions to a dump is also necessary to allow only neutral particles to exist in the thrust plume. Another area of research is designing gas diffusion neutralizers for different types of ion thrusters such as Hall and Helicon. We have only investigated gridded ion sources, but these have finite lifetimes due to the cathode and grids. Additionally, the ionization efficiency of the KDC 10 was not particularly high which was detrimental to the specific impulse. Improving the amount of gas that is ionized by the free electrons from the cathode should be a focus for a future flight-ready thruster.

We did not implement an ion dump into our neutral beam technology demonstrator to deflect the remaining ions post-neutralization. There are two major ways of accomplishing this: magnetic [50] and electrostatic deflection. These ions would be captured and neutralized via an ion dump. There would also be a significant thermal component from the ions to the surface. Whether thermoelectric generators or spacecraft heating would be a worthwhile use for this waste heat should be

investigated.

Finally, additional work to characterize the momentum loss from neutralization should be undertaken. This effect is expected to be more pronounced for higher energy neutral beam due to the need for higher gas background densities in the gas diffusion neutralizer. These measurements could be accomplished through a more sensitive calorimeter or other methods to determine the energy of the beam for increasing gas flow rates. If there is a significant change in momentum that adversely effects the thrust, redesign efforts should be undertaken to mitigate this effect.

Bibliography

[1] "JPL's Center for NEO studies (CNEOS)." URL neo.jpl.nasa.gov/ca, 2018.

[2] R. Binzel, C. Chapman, L. Johnson, T. Jones, R. Schweickart, B. Wilcox, D. Yeomans, and B. Siegel, "Final report of the ad-hoc task force on planetary defense." URL www.nasa.gov/pdf/490945main_10-10_TFPD.pdf, 2010.

[3] E. Christensen, S. Larson, A. Boattini, A. Gibbs, A. Grauer, R. Hill, J. Johnson, R. Kowalski, and R. McNaught, "The Catalina Sky Survey: current and future work," in *AAS/Division for Planetary Sciences Meeting Abstracts*, vol. 44, 2012.

[4] N. Kaiser, "Pan-STARRS: a wide-field optical survey telescope array," in *Ground-based Telescopes*, vol. 5489, pp. 11–23, International Society for Optics and Photonics, 2004.

[5] C. Nugent, A. Mainzer, J. Bauer, R. Cutri, E. Kramer, T. Grav, J. Masiero, S. Sonnett, and E. Wright, "Neowise reactivation mission year two: Asteroid diameters and albedos," *The Astronomical Journal*, vol. 152, no. 3, p. 63, 2016.

[6] J. D. Ruprecht, J. S. Stuart, D. F. Woods, and R. Y. Shah, "Detecting small asteroids with the space surveillance telescope," *Icarus*, vol. 239, pp. 253–259, 2014.

[7] J. Tonry, L. Denneau, A. Heinze, B. Stalder, K. Smith, S. Smartt, C. Stubbs, H. Weiland, and A. Rest, "ATLAS: A high-cadence all-sky survey system," *Publications of the Astronomical Society of the Pacific*, vol. 130, no. 988, p. 064505, 2018.

[8] S. R. Chesley, P. W. Chodas, A. Milani, G. B. Valsecchi, and D. K. Yeomans, "Quantifying the risk posed by potential earth impacts," *Icarus*, vol. 159, no. 2, pp. 423–432, 2002.

[9] R. G. Jahn, *Physics of electric propulsion*. McGraw-Hill, 1968.

[10] R. J. Cybulski, D. M. Shellhammer, R. R. Lovell, E. J. Domino, J. T. Kotnik, J. Cybulski, and R. R. Loveli, "Results from SERT I ion rocket flight test," 1965.

[11] C. Russell and C. Raymond, "The dawn mission to vesta and ceres," *Space Science Reviews*, vol. 163, no. 1-4, pp. 3–23, 2011.

[12] C. Bombardelli, H. Urrutxua, M. Merino, J. Pelaez, and E. Ahedo, "The ion beam shepherd: A new concept for asteroid deflection," *Acta Astronautica*, vol. 90, no. 1, pp. 98–102, 2013.

[13] J. D. Huba, "NRL: Plasma formulary," tech. rep., Naval Research Lab Washington DC beam physics branch, 2004.

[14] "KDC 10." URL http://ionsources.com/products/kdc-10, 2018.

[15] M. M. Menon, "Neutral beam heating applications and development," *Proceedings of the IEEE*, vol. 69, no. 8, pp. 1012–1029, 1981.

[16] T. H. Stix, "Heating of toroidal plasmas by neutral injection," *Plasma Physics*, vol. 14, no. 4, pp. 367–384, 1972.

[17] A. V. Phelps, "Cross sections and swarm coefficients for nitrogen ions and neutrals in n2 and argon ions and neutrals in ar for energies from 0.1 ev to 10 kev," *Journal of Physical and Chemical Reference Data*, vol. 20, no. 3, pp. 557–573, 1991.

[18] C. Bombardelli, D. Amato, and J. L. Cano, "Mission analysis for the ion beam deflection of fictitious asteroid 2015 PDC," *Acta Astronautica*, vol. 118, pp. 296–307, 2016.

[19] D. J. Scheeres, C. M. Hartzell, P. Sánchez, and M. Swift, "Scaling forces to asteroid surfaces: The role of cohesion," *Icarus*, vol. 210, no. 2, pp. 968–984, 2010.

[20] P. Sánchez and D. J. Scheeres, "The strength of regolith and rubble pile asteroids," *Meteoritics & Planetary Science*, vol. 49, no. 5, pp. 788–811, 2014.

[21] C. M. Hartzell and D. J. Scheeres, "The role of cohesive forces in particle launching on the moon and asteroids," *Planetary and Space Science*, vol. 59, no. 14, pp. 1758–1768, 2011.

[22] P. Lee, "Dust levitation on asteroids," *Icarus*, vol. 124, no. 1, pp. 181–194, 1996.

[23] L. Johnson, "Planetary Defense Coordination Office (PDCO)." URL www.lpi.usra.edu/sbag/meetings/jan2017/presentations/Johnson.pdf, 2016.

[24] L. Billings, "Words matter: A call for responsible communication about asteroid impact hazards and plans for planetary defense," *Space Policy*, vol. 33, pp. 8–12, 2015.

[25] M. B. Syal, D. S. Dearborn, and P. H. Schultz, "Limits on the use of nuclear explosives for asteroid deflection," *Acta Astronautica*, vol. 90, no. 1, pp. 103–111, 2013.

[26] B. Wie, "Dynamics and control of gravity tractor spacecraft for asteroid deflection," *Journal of guidance, control, and dynamics*, vol. 31, no. 5, pp. 1413–1423, 2008.

[27] B. Wie, "Hypervelocity nuclear interceptors for asteroid disruption," *Acta Astronautica*, vol. 90, no. 1, pp. 146–155, 2013.

[28] B. Wie, B. Zimmerman, J. Lyzhoft, and G. Vardaxis, "Planetary defense mission concepts for disrupting/pulverizing hazardous asteroids with short warning time," *Astrodynamics*, vol. 1, no. 1, pp. 3–21, 2017.

[29] M. F. A'Hearn, M. Belton, W. Delamere, J. Kissel, K. Klaasen, L. McFadden, K. Meech, H. Melosh, P. Schultz, J. Sunshine, *et al.*, "Deep impact: excavating comet tempel 1," *science*, vol. 310, no. 5746, pp. 258–264, 2005.

[30] A. Gálvez and I. Carnelli, "ESAs Don Quijote Mission: an opportunity for the investigation of an artificial impact crater on an asteroid," in *Proc. 25th Int. Symp. on Space Technology and Science*, 2006.

[31] S. Wagner, B. Wie, and B. W. Barbee, "Target selection for a hypervelocity asteroid intercept vehicle flight validation mission," *Acta Astronautica*, vol. 107, pp. 247–261, 2015.

[32] A. F. Cheng, J. Atchison, B. Kantsiper, A. S. Rivkin, A. Stickle, C. Reed, A. Galvez, I. Carnelli, P. Michel, and S. Ulamec, "Asteroid impact and deflection assessment mission," *Acta Astronautica*, vol. 115, pp. 262–269, 2015.

[33] D. Scheeres and R. Schweickart, "The mechanics of moving asteroids," in *2004 Planetary Defense Conference: Protecting Earth from Asteroids*, p. 1446, AIAA, 2004.

[34] "Solar System Dynamics, Small-Body Database Search Engine." URL https://ssd.jpl.nasa.gov/sbdb_query.cgi, 2017.

[35] D. J. Tholen, "Asteroid taxonomic classifications," in *Asteroids II*, pp. 1139–1150, 1989.

[36] S. J. Bus and R. P. Binzel, "Phase II of the small main-belt asteroid spectroscopic survey: A feature-based taxonomy," *Icarus*, vol. 158, no. 1, pp. 146 – 177, 2002.

[37] J. T. Olympio, "Optimal control of gravity-tractor spacecraft for asteroid deflection," *Journal of guidance, control, and dynamics*, vol. 33, no. 3, pp. 823–833, 2010.

[38] Daniel D. Mazanek and David M. Reeves and Joshua B. Hopkins and Darren W. Wade and Marco Tantardini and Haijun Shen, "Enhanced Gravity Tractor Technique for Planetary Defense," in *4th IAA Planetary Defense Conference*, (Roma, Italy). April 13–17, 2015. Paper number IAA-PDC-15-04-11.

[39] J. R. Brophy and B. Muirhead, "Near-Earth Asteroid Retrieval Mission (ARM) study," *Orbit*, vol. 16, pp. 25–42, 2013.

[40] M. Ceriotti and J. P. Sanchez, "Control of asteroid retrieval trajectories to libration point orbits," *Acta Astronautica*, vol. 126, pp. 342–353, 2016.

[41] P. Lubin, G. B. Hughes, J. Bible, J. Bublitz, J. Arriola, C. Motta, J. Suen, I. Johansson, J. Riley, N. Sarvian, *et al.*, "Toward directed energy planetary defense," *Optical Engineering*, vol. 53, no. 2, p. 025103, 2014.

[42] J. Olds, A. Charania, and M. G. Schaffer, "Multiple mass drivers as an option for asteroid deflection missions," in *2007 Planetary Defense Conference, Washington, DC, Paper*, pp. S3–7, 2007.

[43] M. Vasile and C. A. Maddock, "On the deflection of asteroids with mirrors," *Celest Mech Dyn Astr*, 2010.

[44] A. DeCicco, C. Hartzell, R. Adams, and K. Polzin, "The feasibility of deflecting asteroid 2017 PDC using neutral beam propulsion," *Acta Astronautica*, 2018.

[45] Y. Gao and J. Wu, "Asteroid rotation control via a tethered solar sail," *Advances in Space Research*, vol. 58, no. 11, pp. 2304–2312, 2016.

[46] K. H. Berkner, R. V. Pyle, and J. W. Stearns, "Intense, mixed-energy hydrogen beams for CTR injection," *Nuclear Fusion*, vol. 15, no. 2, p. 249, 1975.

[47] J. Kim and H. Haselton, "Analysis of particle species evolution in neutral-beam injection lines," *Journal of Applied Physics*, vol. 50, no. 6, pp. 3802–3807, 1979.

[48] J. Paméla, "Gas heating effects in the neutralizers of neutral beam injection lines," *Review of scientific instruments*, vol. 57, no. 6, pp. 1066–1068, 1986.

[49] J. Milnes, B. Chuilon, Y. Xue, D. Martin, and C. Waldon, "High heat flux (hhf) elements for negative ion systems on ITER," *Fusion Engineering and Design*, vol. 82, no. 5-14, pp. 945–952, 2007.

[50] P. Franzen, J. Sielanko, H. De Esch, E. Speth, B. Heinemann, and R. Riedl, "Inline magnetic residual ion dump for the ITER neutral beam system," *Fusion engineering and design*, vol. 66, pp. 585–590, 2003.

[51] Y. Xu, C. Hu, S. Liu, L. Yu, N. Group, *et al.*, "Analysis of power deposition on heat load components for EAST neutral beam injector," *Journal of Fusion Energy*, vol. 33, no. 6, pp. 765–769, 2014.

[52] D. J. Economou, "Modeling and simulation of fast neutral beam sources for materials processing," *Plasma Processes and Polymers*, vol. 6, no. 5, pp. 308–319, 2009.

[53] J. K. Ziemer, "Performance measurements using a sub-micronewton resolution thrust stand," 2001.

[54] M. Gamero-Castano, "A torsional balance for the characterization of micronewton thrusters," *Review of scientific instruments*, vol. 74, no. 10, pp. 4509–4514, 2003.

[55] H. Koizumi, K. Komurasaki, and Y. Arakawa, "Development of thrust stand for low impulse measurement from microthrusters," *Review of scientific instruments*, vol. 75, no. 10, pp. 3185–3190, 2004.

[56] J. E. Polk, A. Pancotti, T. Haag, S. King, M. Walker, J. Blakely, and J. Ziemer, "Recommended practices in thrust measurements," tech. rep., California Inst Of Technology Pasadena Jet Propulsion Lab, 2013.

[57] Menner, "Linear variable differential transformer." URL https://en.wikipedia.org/wiki/Linear_variable_differential_transformer, 2018.

[58] T. Markusic, J. Jones, and M. Cox, "Thrust stand for electric propulsion performance evaluation," in *40th AIAA/ASME/SAE/ASEE Joint Propulsion Conference and Exhibit*, p. 3441, 2004.

[59] K. A. Polzin, T. E. Markusic, B. J. Stanojev, A. DeHoyos, and B. Spaun, "Thrust stand for electric propulsion performance evaluation," *Review of Scientific Instruments*, vol. 77, no. 10, p. 105108, 2006.

[60] A. R. Wong, A. Toftul, K. A. Polzin, and J. B. Pearson, "Non-contact thrust stand calibration method for repetitively pulsed electric thrusters," *Review of Scientific Instruments*, vol. 83, no. 2, p. 025103, 2012.

[61] N. Thiry and M. Vasile, "Statistical multi-criteria evaluation of non-nuclear asteroid deflection methods," *Acta Astronautica*, vol. 140, pp. 293–307, 2017.

[62] N. Baresi, D. J. Scheeres, and H. Schaub, "Bounded relative orbits about asteroids for formation flying and applications," *Acta Astronautica*, vol. 123, pp. 364–375, 2016.

[63] L. Blackhall and J. Khachan, "A simple electric thruster based on ion charge exchange," *Journal of Physics D: Applied Physics*, vol. 40, no. 8, pp. 2491–2494, 2007.

[64] A. N. Karpushov, R. Chavan, S. Coda, V. I. Davydenko, F. Dolizy, A. N. Dranitchnikov, B. P. Duval, A. A. Ivanov, D. Fasel, A. Fasoli, *et al.*, "Neutral beam heating on the TCV tokamak," *Fusion Engineering and Design*, vol. 123, pp. 468–472, 2017.

[65] R. Hemsworth, A. Tanga, and V. Antoni, "Status of the ITER neutral beam injection system," *Review of Scientific Instruments*, vol. 79, no. 2, p. 02C109, 2008.

[66] "Planetary Defense Conference Exercise - 2017." URL cneos.jpl.nasa.gov/pd/cs/pdc17, 2017.

[67] S. P. Hughes, R. H. Qureshi, D. S. Cooley, J. J. Parker, and T. G. Grubb, "Verification and validation of the general mission analysis tool (GMAT)," in *AIAA/AAS Astrodynamics Specialist Conference, AIAA SPACE Forum*, pp. 1–32, 2014.

[68] D. Scheeres, D. Britt, B. Carry, and K. Holsapple, "Asteroid interiors and morphology," *Asteroids IV*, pp. 745–766, 2015.

[69] B. Carry, "Density of asteroids," *Planetary and Space Science*, vol. 73, no. 1, pp. 98–118, 2012.

[70] B. E. Clark, J. Ziffer, D. Nesvorny, H. Campins, A. S. Rivkin, T. Hiroi, M. A. Barucci, M. Fulchignoni, R. P. Binzel, S. Fornasier, *et al.*, "Spectroscopy of B-type asteroids: Subgroups and meteorite analogs," *Journal of Geophysical Research: Planets*, vol. 115, no. E6, 2010.

[71] A. J. DeCicco and C. M. Hartzell, "System-level design considerations for asteroid despin via neutral beam emitting spacecraft," in *Aerospace Conference, 2016 IEEE*, pp. 1–8, IEEE, 2016.

[72] O. P. Popova, P. Jenniskens, V. Emelyanenko, A. Kartashova, E. Biryukov, S. Khaibrakhmanov, V. Shuvalov, Y. Rybnov, A. Dudorov, V. I. Grokhovsky, *et al.*, "Chelyabinsk airburst, damage assessment, meteorite recovery, and characterization," *Science*, vol. 342, no. 6162, pp. 1069–1073, 2013.

[73] C. F. Chyba, P. J. Thomas, and K. J. Zahnle, "The 1908 tunguska explosion: atmospheric disruption of a stony asteroid," *Nature*, vol. 361, no. 6407, pp. 40–44, 1993.

[74] G. Karniadakis, A. Beskok, and M. Gad-el Hak, "Micro flows: fundamentals and simulation," *Applied Mechanics Reviews*, vol. 55, pp. 113–138, 2002.

[75] E. M. Petro and R. J. Sedwick, "Survey of moderate-power electric propulsion systems," *Journal of Spacecraft and Rockets*, pp. 1–13, 2017.

[76] "UltraFlex Solar Array Systems." URL orbitalatk.com/space-systems/space-components/solar-arrays/docs/UltraFlex_Factsheet.pdf, 2017.

[77] J. F. Ziegler, M. D. Ziegler, and J. P. Biersack, "SRIM–the stopping and range of ions in matter (2010)," *Nuclear Instruments and Methods in Physics Research Section B: Beam Interactions with Materials and Atoms*, vol. 268, no. 11-12, pp. 1818–1823, 2010.

[78] "Chipquik SMD291." URL http://www.chipquik.com/datasheets/SMD291.pdf, 2018.

[79] "Workmanship standard for crimping, interconnecting cables, harnesses, and wiring (revision a 2016-06-30)." URL https://standards.nasa.gov/standard/nasa/nasa-std-87394, 2016.

[80] "Ultra High and High Vacuum Greases." URL https://static.mimaterials.com/apiezon/DocumentLibrary/TechnicalDatasheets/Apiezon_L_M_and_N_Ultra_High_and_High_Vacuum_Greases_Datasheet.pdf, 2018.

[81] "J-b weld twin tube." URL https://www.jbweld.com/collections/epoxy-adhesives/products/j-b-weld-twin-tube, 2018.

[82] "D-sub, 50 poles, female, straight, turned solder buckets, holes." URL https://b2b.harting.com/files/download/PRD/PDF_TS/096705047XX_BL01_R29754_100198224DRW002A.pdf, 2018.

[83] "OMEGA fma-a2400." URL https://www.omega.com/pptst/FMAA2100_2200_2300_2400.html, 2018.

[84] S. R. Mohanty, H. Bhuyan, N. K. Neog, R. K. Rout, and E. Hotta, "Development of multi faraday cup assembly for ion beam measurements from a low energy plasma focus device," *Japanese journal of applied physics*, vol. 44, no. 7R, p. 5199, 2005.

[85] K. L. Brown and G. W. Tautfest, "Faradaycup monitors for highenergy electron beams," *Review of Scientific Instruments*, vol. 27, no. 9, pp. 696–702, 1956.

[86] W. M. Haynes, *CRC handbook of chemistry and physics*. CRC press, 2014.

[87] ASTM, "E457-08, standard test method for measuring heat-transfer rate using a thermal capacitance (slug) calorimeter," *Annual book of ASTM standards, Space simulation; aerospace and aircraft; Compos. mater*, p. 15, 2008.

[88] C. Uher, "4.3. 2 temperature dependence of thermal conductivity of graphite," in *Thermal Conductivity of Pure Metals and Alloys*, pp. 430–439, Springer, 1991.

[89] T. Nihira and T. Iwata, "Temperature dependence of lattice vibrations and analysis of the specific heat of graphite," *Physical Review B*, vol. 68, no. 13, p. 134305, 2003.

[90] J. A. Englander, B. A. Conway, and T. Williams, "Automated mission planning via evolutionary algorithms," *Journal of Guidance, Control, and Dynamics*, vol. 35, no. 6, pp. 1878–1887, 2012.